

## **INFORMATION TO USERS**

This manuscript has been reproduced from the microfilm master. UMI films the text directly from the original or copy submitted. Thus, some thesis and dissertation copies are in typewriter face, while others may be from any type of computer printer.

**The quality of this reproduction is dependent upon the quality of the copy submitted.** Broken or indistinct print, colored or poor quality illustrations and photographs, print bleedthrough, substandard margins, and improper alignment can adversely affect reproduction.

In the unlikely event that the author did not send UMI a complete manuscript and there are missing pages, these will be noted. Also, if unauthorized copyright material had to be removed, a note will indicate the deletion.

Oversize materials (e.g., maps, drawings, charts) are reproduced by sectioning the original, beginning at the upper left-hand corner and continuing from left to right in equal sections with small overlaps.

Photographs included in the original manuscript have been reproduced xerographically in this copy. Higher quality 6" x 9" black and white photographic prints are available for any photographs or illustrations appearing in this copy for an additional charge. Contact UMI directly to order.

ProQuest Information and Learning  
300 North Zeeb Road, Ann Arbor, MI 48106-1346 USA  
800-521-0600

**UMI<sup>®</sup>**



**Photoemission study of MnBi and GdNi<sub>2</sub>Ge<sub>2</sub>**

by

**Derek Paul Brammeier**

**A dissertation submitted to the graduate faculty  
in partial fulfillment of the requirements for the degree of**

**DOCTOR OF PHILOSOPHY**

**Major: Condensed Matter Physics**

**Major Professor: David W. Lynch**

**Iowa State University**

**Ames, Iowa**

**2001**

UMI Number: 3016690

UMI<sup>®</sup>

---

UMI Microform 3016690

Copyright 2001 by Bell & Howell Information and Learning Company.

All rights reserved. This microform edition is protected against  
unauthorized copying under Title 17, United States Code.

---

Bell & Howell Information and Learning Company  
300 North Zeeb Road  
P.O. Box 1346  
Ann Arbor, MI 48106-1346

**Graduate College  
Iowa State University**

**This is to certify that the Doctoral dissertation of**

**Derek Paul Brammeier**

**has met the dissertation requirements of Iowa State University**

Signature was redacted for privacy.

**Major Professor**

Signature was redacted for privacy.

**For the Major Department**

Signature was redacted for privacy.

**For the Graduate College**

**TABLE OF CONTENTS**

<b>CHAPTER 1: INTRODUCTION</b>	1
MnBi	1
GdNi <sub>2</sub> Ge <sub>2</sub>	2
<b>CHAPTER 2: PHOTOELECTRON SPECTROSCOPY</b>	4
The 3-step Model	7
Energy Band Mapping	19
Core-levels	20
Resonant Photoemission	22
<b>CHAPTER 3: LIGHT SOURCE</b>	24
Synchrotron Radiation	26
Synchrotron Beamlines	32
Electron Energy Analyzer	39
<b>CHAPTER 4: RESULTS AND DISCUSSION</b>	44
Photoemission Study of MnBi	44
Photoemission Study of GdNi <sub>2</sub> Gd <sub>2</sub>	64
<b>CHAPTER 5: SUMMARY</b>	90
<b>APPENDIX A: THE KERR EFFECT</b>	92
<b>APPENDIX B: SPIN DENSITY WAVES</b>	96

<b>REFERENCES</b>	<b>101</b>
-------------------	------------

<b>ACKNOWLEDGEMENTS</b>	<b>105</b>
-------------------------	------------

## **CHAPTER 1: INTRODUCTION**

The purpose of this study is to use synchrotron radiation photoelectron spectroscopy to investigate single crystals of MnBi and GdNi<sub>2</sub>Ge<sub>2</sub>. Photoelectron spectroscopy is a tool which allows us to examine the electronic states (both core levels and valence band) of materials. Using angle resolved photoelectron spectroscopy, we are even able to map band structures of crystals. The electronic structure of materials, especially that of the outer orbitals, accounts for most of their physical properties. Knowledge of the electronic structure allows for a better understanding of the systems and lends itself to the understanding and discovery of other novel materials. Using synchrotron radiation as the light source gives photoelectron spectroscopy even more flexibility in studying the electronic states.

### **MnBi**

Photoemission was used to explore both the valence band and the shallow core levels of MnBi. In the past, numerous papers have been written investigating thin films of MnBi due to its potential for magneto-optic recording [1, 2, 3]. This is due, in part, to

a large Kerr rotation in both visible and ultraviolet (UV) light (see appendix A for a short description of the Kerr effect). While MnBi itself has proved less than adequate for this purpose, compounds of MnBi doped with other atoms, as well as with different stoichiometries, have proven to be closer to the ideal material [4]. Recently, several calculations of the electronic structure of the MnBi single crystal (as well as other MnBi and Mn-pnictide compounds) have been made to theoretically predict the Kerr rotation and other aspects of the system [4, 5, 6]. Some of these calculations have differing results, further meriting an experimental study of the electronic structure.

### **GdNi<sub>2</sub>Ge<sub>2</sub>**

Photoemission was used to explore the valence band and shallow core levels of GdNi<sub>2</sub>Ge<sub>2</sub>. The ternary rare-earth intermetallic compounds with the ThCr<sub>2</sub>Si<sub>2</sub> structure are known for their wide variety of magnetic properties [7]. Specifically, GdNi<sub>2</sub>Ge<sub>2</sub> shows two magnetic transitions at low temperature [8]. The first transition is a paramagnetic to antiferromagnetic (AF) transition and occurs at a Néel temperature of  $T_N = 27.1$  K, while the second transition (to another antiferromagnetic phase) occurs at a temperature of  $T_1 = 16.8$  K. The AF Néel transition is reported to be driven by strong Fermi surface nesting [8]. This nesting is responsible for the incommensurate magnetic modulation of  $\mathbf{q} = (0, 0, 0.793)$ , or a spin density wave (SDW). For a brief discussion on spin density waves and Fermi surface nesting, please see appendix B. A generalized susceptibility calculation was made (*Z. Islam*) [8] using the tight-binding linear-muffin-

tin-orbital (Tb-LMTO) method with the atomic sphere approximation (ASA) to prove the nesting to be responsible for the incommensurate structure. In the calculation, the Gd 4f electrons were treated as part of the atomic core. Here, we successfully tested the calculated band structure. An attempt was made to detect the SDW in  $\text{GdNi}_2\text{Ge}_2$ , but it was unsuccessful.

## CHAPTER 2: PHOTOELECTRON SPECTROSCOPY

Photoelectron spectroscopy (PES) is an old experimental technique still in extensive use [9]. It has become increasingly powerful with the flexibility provided by synchrotron radiation. The phenomenon of photoemission was first detected by Hertz in 1887 [10]. In a photoemission event, a photon impinges on a sample, and, via the photoelectric effect (the ejection of an electron when an atom is placed in a radiation field) an electron is liberated, which then escapes into the vacuum. In 1905, Einstein was able to explain the photoelectric effect by using the quantum nature of light:

$$E_{kin,max} = h\nu - \Phi , \quad (2.1)$$

where  $E_{kin,max}$  is the maximum electron kinetic energy,  $h\nu$  is the energy of the photon, and  $\Phi$  is the work function of the sample [11].

In general, the photoemission experiment consists initially of exciting electrons via the photoelectron effect. These electrons are then analyzed by measuring their kinetic energy  $E_{kin}$  and their momentum  $\mathbf{p}$  (wave vector  $\mathbf{p}/\hbar$ ) in an electrostatic analyzer. Knowing the energy of the light ( $h\nu$ ) and the work function  $\Phi$ , one can determine the binding energy of the electrons via the following equation:

$$E_{kin} = h\nu - \Phi - |E_B| . \quad (2.2)$$

This is just an extension of (2.1) to include electrons of all binding energies  $E_B$ . The momentum  $\mathbf{p}$  of the outgoing electron is determined by

$$E_{kin} = \frac{\mathbf{p}^2}{2m} \quad , \quad |\mathbf{p}| = \sqrt{2m \cdot E_{kin}} \quad . \quad (2.3)$$

The direction of  $\mathbf{p}/\hbar$  is obtained from  $\theta$  and  $\phi$  which are the polar and azimuthal angles at which the electrons leave the sample surface.

Figure 2.1 shows how the energy levels in a solid relate to the energy distribution of the photoemitted electrons [12].  $N(E)$  represents the number of states at a given energy. The sample is shown to have core levels and a valence band. The Fermi energy  $E_F$  runs through the valence band, so this sample is a metal.  $E_{vac}$  represents the vacuum level, and is the reference point for the spectra. If the photoemission takes place from a core level of binding energy  $E_B$  ( $E_B = 0$  at  $E_F$ ) the photoelectrons can be detected with kinetic energy  $E_{kin} = h\nu - \Phi - |E_B|$  in the vacuum (Note that  $E_F$  is the reference in the solid, but in the vacuum everything is measured with respect to  $E_{vac}$ , though one typically does not plot  $E_{kin}$ , but  $E_B$  instead).

In PES experiments, photons can be in the ultraviolet region (5 to 100 eV, UPS), the soft x-ray region (100 to 1000 eV, SXPS), or the x-ray region ( $> 1000$  eV, XPS). In our experiments, UPS is predominantly used. It is ideal to study valence bands and shallow core levels (due to higher resolution) and  $\mathbf{k}$ -conserving (“direct”) transitions (due to the small momentum of the photon).

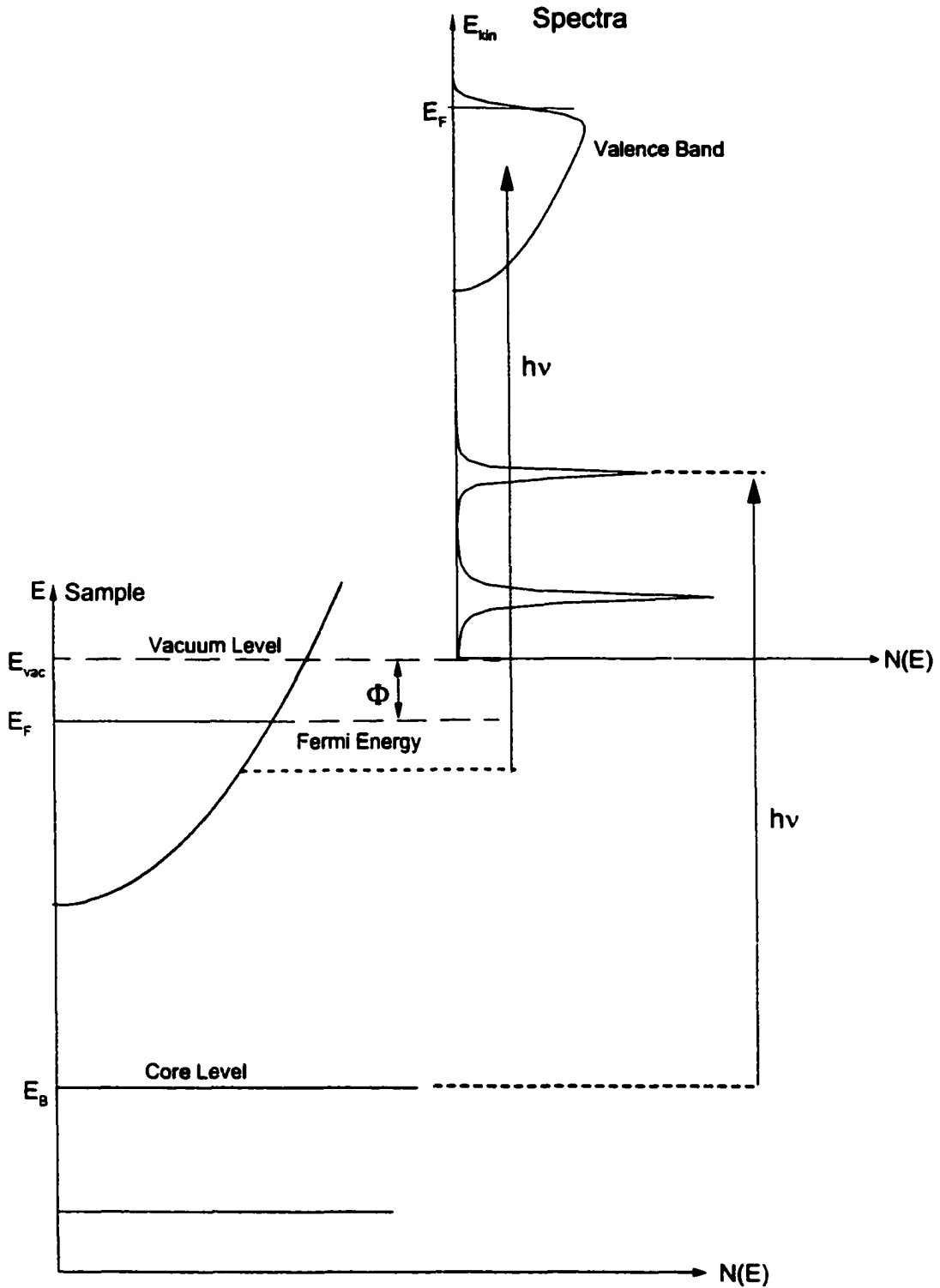


FIG. 2.1 Relation between the energy levels in a solid and the electron energy distribution produced by photons of energy  $h\nu$  [12].

### The 3-step Model

To interpret the photoemission spectra, the model most commonly used is the three-step model (see Fig. 2.2) [13]. In the three-step model the PES experiment is broken up into three distinct processes:

- 1) Optical excitation of the electron in the solid.
- 2) Transport of the electron to the surface.
- 3) Escape of the electron into the vacuum.

The culmination of these three processes results in the intensity spectra  $N(E)$ . Note that the three-step process is purely a phenomenological approach, yet it is descriptive and very successful in explaining the essence of photoemission.

In the photoexcitation of the electron (step 1), the solid is initially in its ground state, described by a Hamiltonian  $H_0$ . The incident photon beam will introduce a small perturbation

$$H' = \frac{e}{2mc} (\mathbf{A} \cdot \mathbf{p} + \mathbf{p} \cdot \mathbf{A}) \quad (2.4)$$

where  $\mathbf{p}$  is the momentum operator, and  $\mathbf{A}$  is the vector potential of the incident light.

The internal energy distribution of photoexcitations  $N_{\text{int}}(E, h\nu)$ , where  $E$  is the final kinetic energy and  $h\nu$  is the photon energy, is given by

$$N_{\text{int}}(E, h\nu) \propto \sum_{f,i} |\langle f | \mathbf{A} \cdot \mathbf{p} | i \rangle|^2 \delta(E_f(\mathbf{k}_f) - E_i(\mathbf{k}_i) - h\nu) \delta(E - [E_f(\mathbf{k}_f) - \Phi]) \quad (2.5)$$

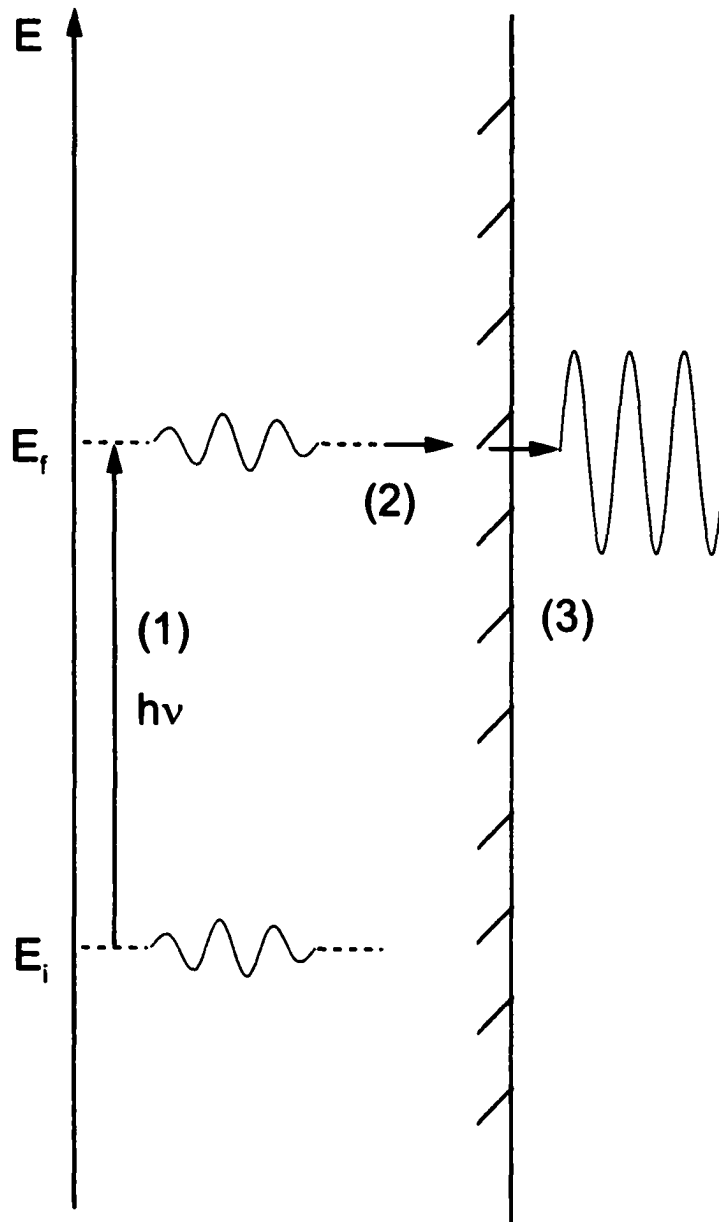


FIG. 2.2 The three-step process in PES. It consists of (1) photoexcitation of an electron, (2) its travel to the surface, and (3) its transmission through the surface into the vacuum [13].

where  $|i\rangle$  and  $|f\rangle$  are the initial and final state wavefunctions, respectively, and the  $E_f(\mathbf{k}_f)$  and  $E_i(\mathbf{k}_i)$  are the energies of final and initial states, respectively. The first delta function imposes energy conservation and the second delta function ensures that the kinetic energy measured outside the sample equals the final state energy inside, minus the workfunction. The conservation of momentum is implicit in the matrix element  $\langle f | \mathbf{A} \cdot \mathbf{p} | i \rangle$  and is given by

$$\mathbf{k}_f = \mathbf{k}_i + \mathbf{G} \quad (2.6)$$

where  $\mathbf{G}$  is a reciprocal lattice vector. Equation (2.6) represents a “direct” transition, treating the photon momentum as equal to 0. Band structures are usually plotted in the reduced zone scheme which means that the bands outside the first Brillouin zone are folded back into the first Brillouin zone by adding the appropriate reciprocal lattice vector  $\mathbf{G}$ . Figure 2.3 shows a direct optical transition between two bands (the final state  $E_f$  being above the vacuum level  $E_v$ ), as well as the resulting kinetic energy  $E_{\text{kin}}$  of the photoelectron as a function of its wavevector  $\mathbf{p} / \hbar$  after emission into the vacuum.

After excitation, the electrons must travel to the surface of the solid (step 2). Some of the electrons will be scattered by other electrons or excitations like phonons and plasmons. In the case of inelastic scattering, they will lose part of their energy and change momentum. These photoelectrons are then detected as satellite peaks or background emission in the spectrum. To quantify this effect, we assume that the scattering frequency  $1/\tau$  ( $\tau$  = lifetime) is isotropic and depends only on  $E$ . Then the inelastic mean free path  $\lambda(E, \mathbf{k})$  is given by

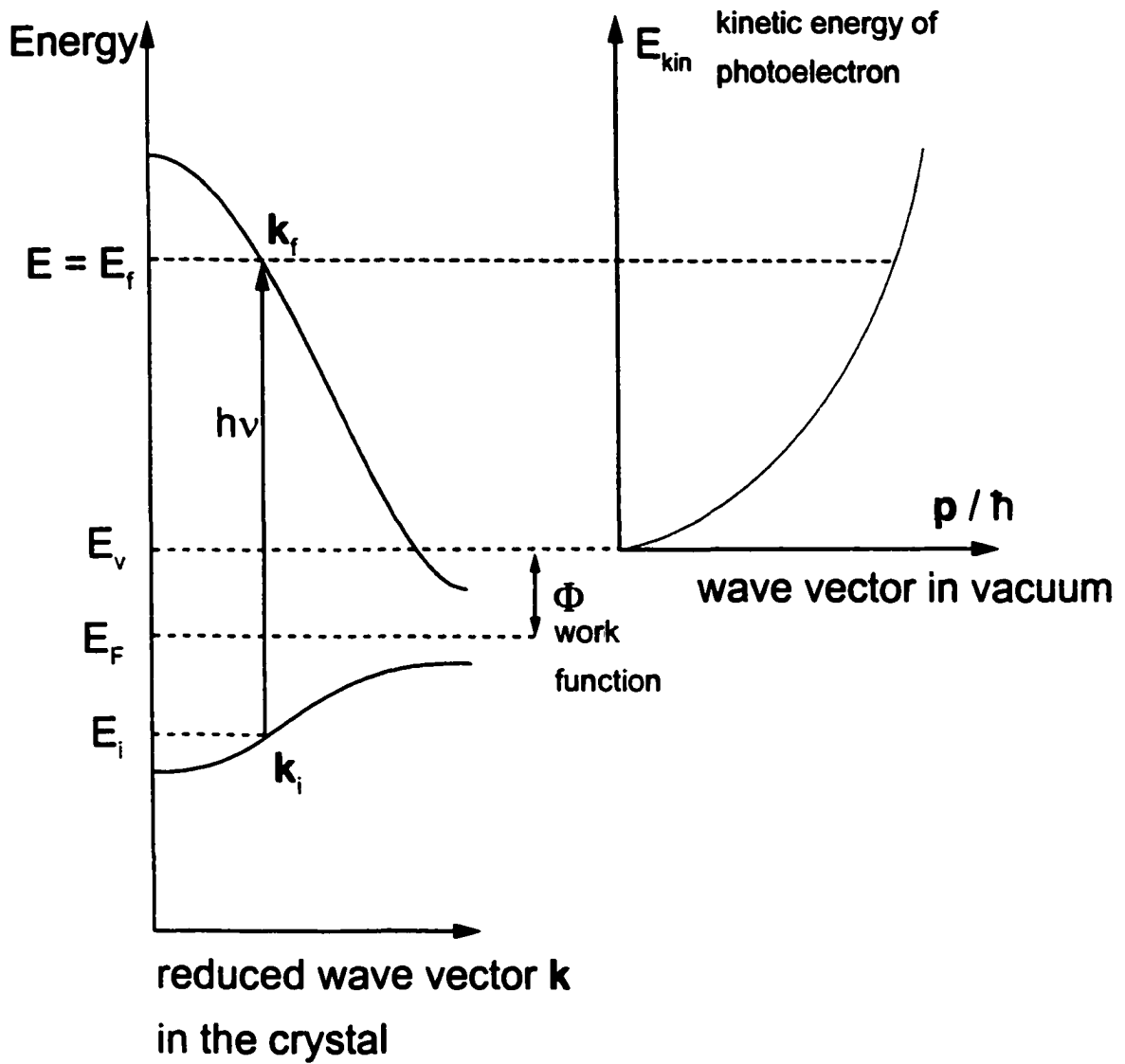


FIG. 2.3 Energy versus momentum shown for a "direct" or "vertical" transition between two energy bands. The left axis shows the photoelectron states in the crystal and the right axis shows its state after emission into the vacuum.

$$\lambda(E, \mathbf{k}) = \tau v_g = \frac{\tau}{\hbar} \frac{dE}{d\mathbf{k}} \quad (2.7)$$

where  $v_g$  is the group velocity of the final state. We assume that, on average, a photoelectron can travel over a mean free path before being scattered. Figure 2.4 shows a plot of scattering lengths of various elements at different energies [14]. Note that it follows a “universal curve”. For UPS, the mean free path can be seen to be 2-20Å. It is obvious, then, that UPS is surface sensitive due to the short mean free path of the photoelectrons. The expression for the transport can then be written as

$$d(E, \mathbf{k}) \cong \frac{\alpha \lambda}{1 + \alpha \lambda}, \quad (2.8)$$

where  $\alpha$  is the optical absorption coefficient of the light ( $\alpha^{-1} \cong 100 - 1000\text{Å}$ ) [15].  $d(E, \mathbf{k})$  describes the fraction of the total number of photoelectrons created within one mean free path  $\lambda$  from the surface.

After transport to the surface, the photoexcited electrons may be transmitted to the vacuum (step 3). This problem is treated classically: if an electron approaches the surface with an energy  $E > E_v - E_o$  normal to the surface (where  $E_v$  is the vacuum level and  $E_o$  is the bottom of the valence band, see Fig. 2.5a), then it will escape into the vacuum. This ignores the possibility of quantum reflection at the potential step ( $E_v - E_o$ ) of the surface.

In Fig. 2.5a, we use the “free-electron final-state model”. In this common model, we assume that the final state is that of a free electron. The final-state wavevector can then be obtained by the intersection of the free-electron parabola with its zero at the bottom of the valence band ( $E_o < 0$ ) and the final state energy  $E_f$ :

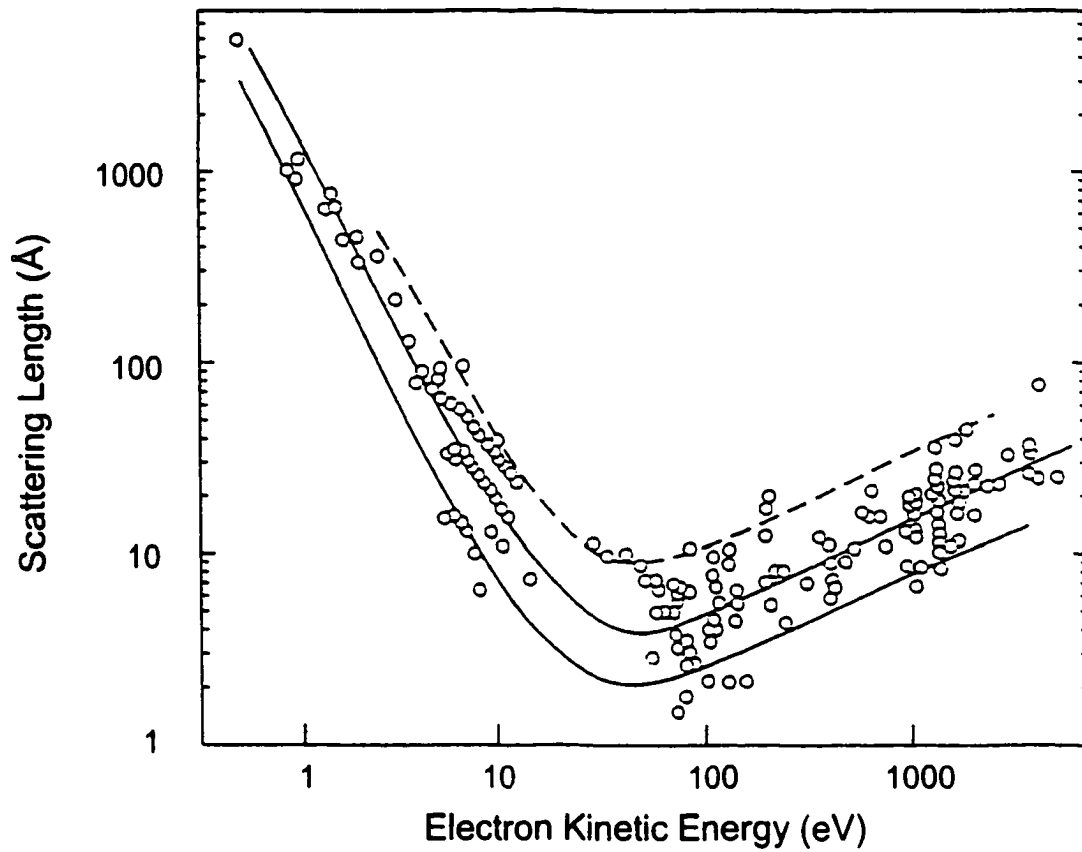


FIG. 2.4 The "universal curve" showing the photoelectron scattering length or mean free path as a function of its kinetic energy [14].

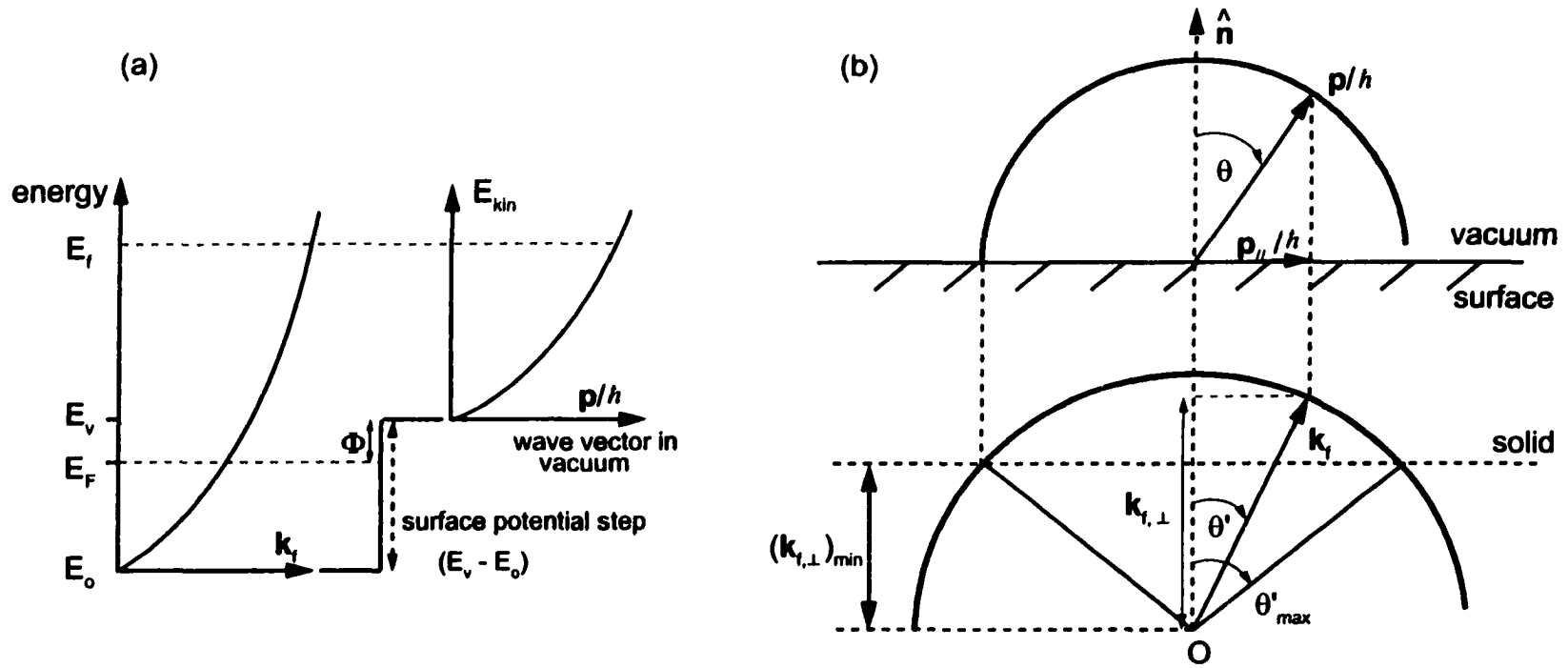


FIG. 2.5 a) A schematic of the "free electron final state model". b) The escape condition for (a) [13].

$$E_f = \left( \frac{\hbar^2}{2m^*} \right) (\mathbf{k} + \mathbf{G})^2 \quad (2.9)$$

where  $m^*$  is the effective mass (typically taken to be equal to the electron mass), and the energies are measured with respect to the Fermi energy  $E_F$ .

In its escape to the vacuum, the wavevector parallel to the surface  $\mathbf{k}_{f,\parallel} = \mathbf{p}_{\parallel}/\hbar$ , is conserved. The wavevector perpendicular to the surface  $\mathbf{k}_{f,\perp}$  is not conserved due to the surface potential step. The photoelectron trajectory then forms an “escape cone” shown in Fig. 2.5b.

The external and internal escape cones in Fig. 2.5b have radii  $|\mathbf{p}|/\hbar = \text{const.}$  and  $|\mathbf{k}_f| = \text{const.}$  respectively. One can see from the figure how, due to the loss of energy normal to the surface, the direction of the photoelectron makes a larger angle with the surface normal in the vacuum than in the solid. Therefore, for every final state energy  $E_f$  ( $\theta < \pi/2$ ) there is a maximum angle ( $\theta'_{\text{max}} < \pi/2$ ) inside the sample for which escape is possible, given by:

$$\cos \theta'_{\text{max}} = \left( \frac{|\mathbf{k}_{f,\perp}|}{|\mathbf{k}_f|} \right)^{1/2} = \left( \frac{E_v - E_o}{E_f - E_o} \right)^{1/2}. \quad (2.10)$$

The escape function  $T(E)$ , the fraction of electrons that escape the solid, can then be written as

$$T(E) = \frac{1}{2} \left( 1 - \left( \frac{E_v - E_o}{E_f - E_o} \right)^{1/2} \right) \quad \text{for } E_f - E_o > E_v - E_o, \text{ and}$$

$$T(E) = 0 \quad \text{for } E_f - E_o < E_v - E_o. \quad (2.11)$$

The 1/2 is present because only electrons traveling toward the surface are counted.

The final expression for the photoelectron energy spectrum  $N(E, h\nu)$  is then

$$N(E, h\nu) \propto \sum_{f,i} |\langle f | \mathbf{A} \cdot \mathbf{p} | i \rangle|^2 \delta(E_f(\mathbf{k}_f) - E_i(\mathbf{k}_i) - h\nu) \delta(E - [E_f(\mathbf{k}_f) - \Phi]) \\ \times d(E, \mathbf{k}) \times T(E). \quad (2.12)$$

Note that  $d(E, \mathbf{k})$  and  $T(E)$  are smooth functions, so any structure in the spectrum is due to the optical excitation process.

The resulting spectrum of  $N(E)$ , at photon energy  $h\nu$  is called an energy distribution curve (EDC). At a given photon energy, the photoemitted electron kinetic energy is scanned, giving an output of intensity vs. electron kinetic energy. The maximum kinetic energy is usually subtracted from the x-axis in order to zero the Fermi energy  $E_F$ . EDCs are not the only type of data that can be taken. Constant initial state (CIS) and constant final state (CFS) scans are also possible. A CIS involves scanning both photon energy and kinetic energy at the same time. If they are scanned at the same rate, the photoelectrons detected will always be from the same initial state in the sample. A CFS involves scanning the photon energy and measuring intensity at a constant  $E_{kin}$ . The CFS technique is typically used to perform low  $E_{kin}$  partial yield spectroscopy, which is structurally equivalent to the absorption coefficient. A diagram showing the different scans (EDC, CIS, and CFS) is given in Fig. 2.6 [16]. In our experiments, EDCs are most common while CIS scans were taken occasionally to utilize resonant photoemission (described later).

The geometry of a general photoemission experiment is shown in Fig. 2.7. In the figure,  $\mathbf{A}$  is the vector potential of the incoming radiation which has an incidence angle of

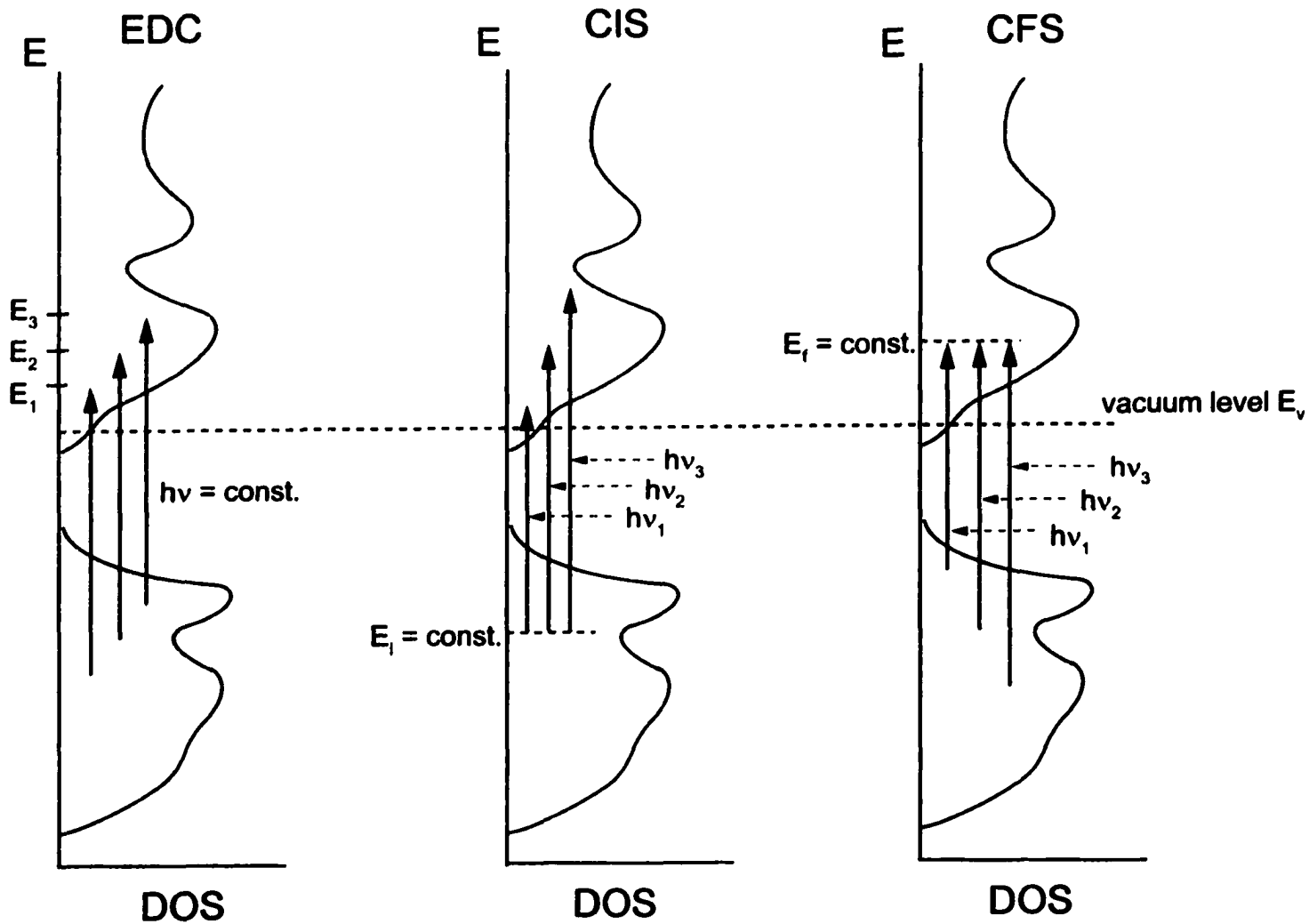
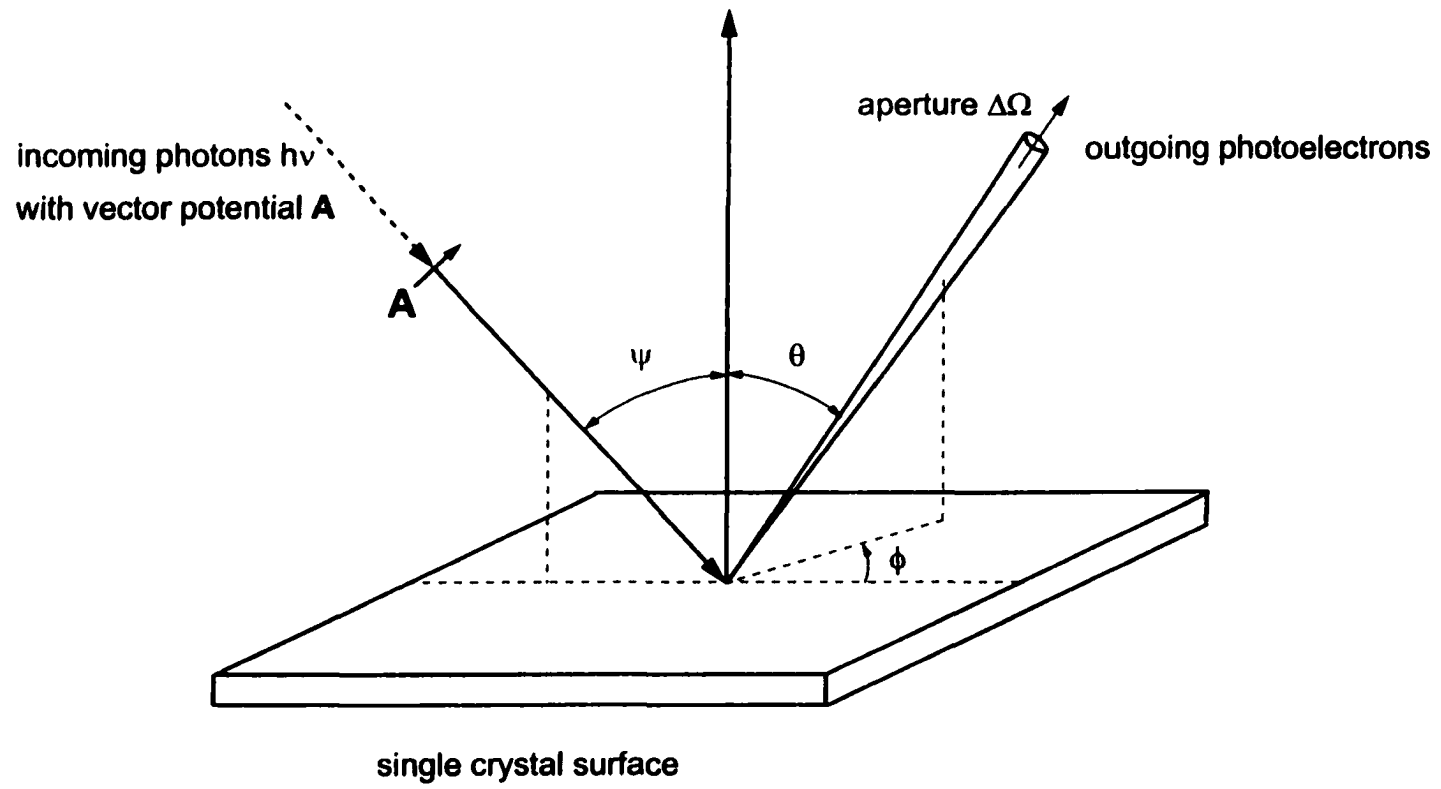


FIG. 2.6 Schematics of an energy distribution curve (EDC), a constant initial state scan (CIS), and a constant final state scan (CFS) [16].



**FIG. 2.7** Schematic of the external geometry of a photoemission experiment.

$\psi$  with the sample surface normal. The emitted electrons are detected in a solid angle  $\Delta\Omega$  (the detector's acceptance angle) in the direction given by  $\varphi$  and  $\theta$  where  $\varphi$  is the azimuthal detection angle and  $\theta$  is the polar detection angle with respect to the crystal axes.

There are generally two different ways the emitted electrons are measured. There are angle-resolved measurements, and angle-integrated measurements. Angle-resolved photoelectron spectroscopy (ARPES) refers to the case where single crystal samples are used and the solid angle of detection is small ( $\Delta\Omega$  preferably  $\leq 2^\circ \times 2^\circ$ ). One is then able to use  $\mathbf{k}$ -conservation by detecting the electrons in a small  $\mathbf{k}$ -interval. When used with photon energies in the ultraviolet range, it is known as ARUPS (angle resolved ultraviolet photoelectron spectroscopy), and is capable of mapping the band-structures of materials (detailed later).

Angle integrated photoelectron spectroscopy (AIPES) refers to the case where the solid angle of collection by the detector is large so that the  $\mathbf{k}$ -information is blurred by integration over all outgoing wave vectors. These measurements can be performed on single crystal surfaces, but are usually used with polycrystalline samples. AIPES can represent the joint density of states (JDOS) of a material. The JDOS gives the total number of direct transitions that are possible for a particular photon energy.

## Energy Band Mapping

Often, it is possible to use the EDCs from ARUPS to map the band structure of a single-crystal sample [17]. The goal is to obtain the initial and final state energies ( $E_i$  and  $E_f$ ) and wavevectors ( $\mathbf{k}_i \cong \mathbf{k}_f$  for direct transitions) of the emitted photoelectrons. These quantities are obtained from the measured quantities of the kinetic energy  $E_{kin}$ , and the horizontal and vertical angles of detection  $\varphi$  and  $\theta$ . Knowing the work function  $\Phi$ ,  $E_i$  and  $E_f$  are easy to acquire through the conservation of energy:

$$E_f = E_{kin} + \Phi, \quad E_f = E_i + \hbar\omega \quad (2.13)$$

The determination of the final-state wave vectors  $\mathbf{k}_f$  is more difficult. Since  $\mathbf{k}_\parallel$  is conserved, we know

$$\mathbf{k}_\perp = \frac{\mathbf{p}_\perp}{\hbar} = \sqrt{(2m/\hbar^2)E_{kin}} \sin\theta, \quad (2.14)$$

so  $\mathbf{k}_\parallel$  is easily attainable. However,  $\mathbf{k}$  is not conserved normal to the surface, so we have no expressions that include  $\mathbf{k}_\perp$ .

One way to overcome this problem is by assuming a free electron final state (described earlier in Fig. 2.5a). This is the simplest, most economical, and most-used method. We recall equation 2.9

$$E_f = \left( \frac{\hbar^2}{2m^*} \right) (\mathbf{k}_f + \mathbf{G})^2 - |E_o|, \quad (2.9)$$

giving an expression that includes  $\mathbf{k}_f$ . Now, the only parameter we need to determine is

the inner potential  $V_o = E_v + |E_o| = |E_o| + \Phi$ . One method to obtain  $V_o$  is by looking for symmetries in the  $E(\mathbf{k}_\perp)$  curves, as symmetries often indicate the crossing of a Brillouin zone. We can then find  $\mathbf{k}_f$  from (2.9) and obtain  $\mathbf{k}_\perp$  via

$$\mathbf{k}_f = \sqrt{\mathbf{k}_\perp - \mathbf{k}_\parallel}. \quad (2.15)$$

Figure 2.8 shows a schematic of the process, using an EDC measured from the (111) plane of an fcc crystal at normal emission [17]. The kinetic energies of the peaks are mapped onto the free electron parabola with its "0" at  $E_o$  to give  $\mathbf{k}_{f\perp}$ . The energy is then mapped from  $E_f$  to  $E_i$  by subtracting  $h\nu$ . Finally, we map the  $\mathbf{k}_{f\perp}$  into the first Brillouin zone with  $\mathbf{G}(111)$  to obtain  $\mathbf{k}_{i\perp}$ .

### Core-levels

One can also take spectra of the shallow core levels using UPS. Core-level spectra can be useful for identifying atoms of the sample near the surface, as well as giving some information of the bonding involved. An equation describing the general line shape of a core level was developed by Doniach and Sunjic [18]. It was the result of convoluting a  $1/(\omega_o - \omega)^{1-\alpha}$  singularity with a Lorentzian of lifetime width  $2\gamma$ , and is given by:

$$f(\omega) = \frac{\Gamma(1-\alpha) \cos \left[ \frac{\pi\alpha}{2} + (1-\alpha) \arctan \left( \frac{\omega_o - \omega}{\gamma} \right) \right]}{\left( (\omega_o - \omega)^2 - \gamma^2 \right)^{(1-\alpha)/2}} \quad (2.16)$$

where  $\Gamma$  is the  $\Gamma$ -function and  $\omega_o$  is the x-ray frequency at the absorption threshold.  $\alpha$

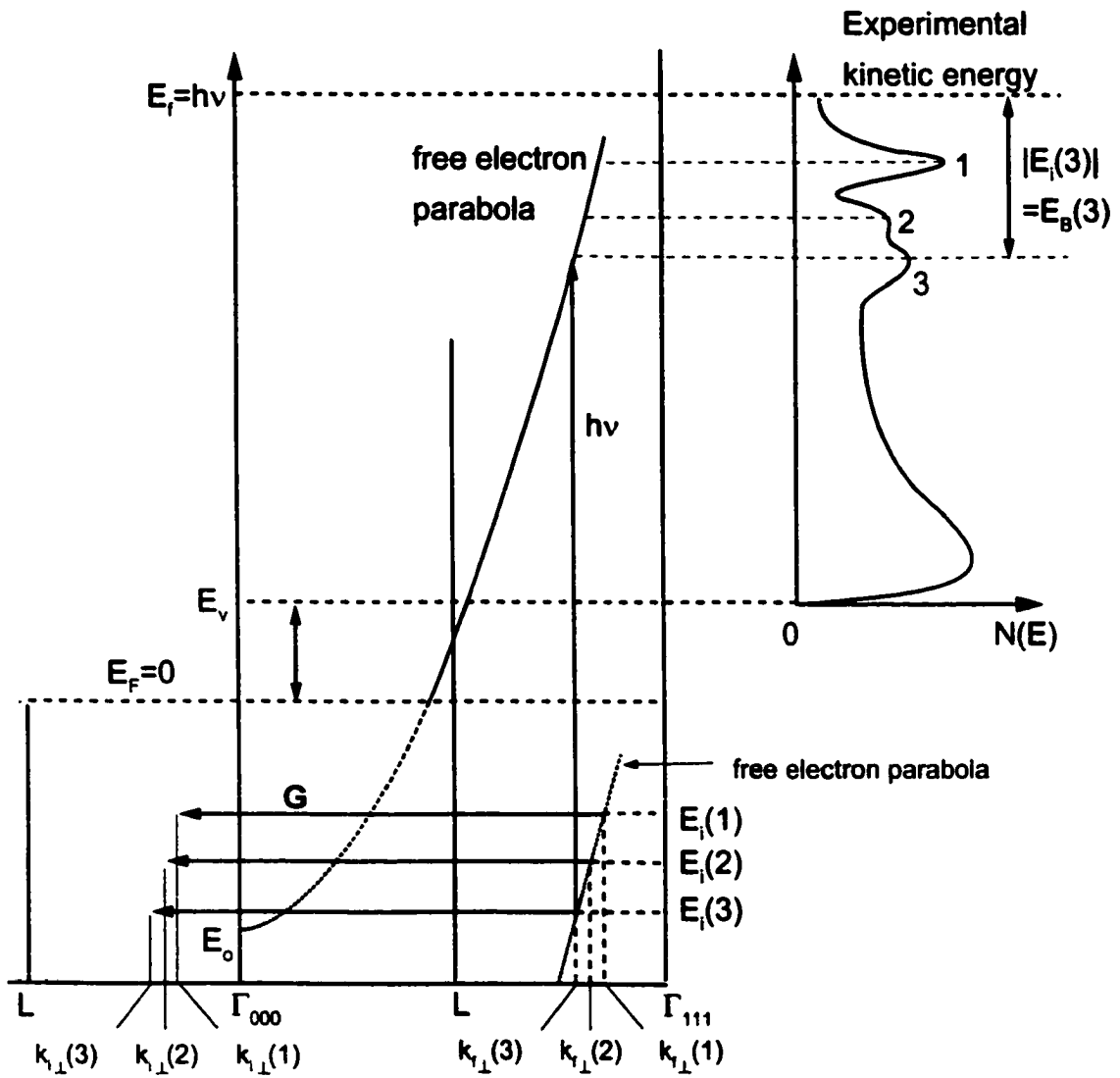


FIG. 2.8 Schematic of band structure determination using a free-electron parabola for normal emission from the (111) plane of an fcc crystal [17].

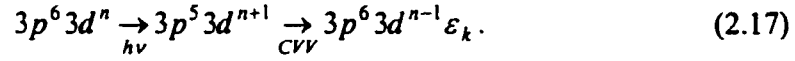
is an asymmetry parameter which causes an asymmetric line shape. It originates from the core hole (from the photoemitted electron) acting as a potential which scatters the conduction electrons. This leads to a “tail” in the PES spectrum. When  $\alpha$  is zero,  $f(\omega)$  becomes a Lorentzian.

Besides the skewed PES peak of the core level, there may be many other features accompanying the main peak. These extra peaks are known as satellites. They can be caused intrinsically or extrinsically. Intrinsic satellites are caused by the photoemission process itself. Since the electrons interact with each other, the emission of one electron will lead to excitations of the system. These excitations require energy and thus lead to signals with a larger binding energy. Extrinsic satellites are caused when the photoelectron travels through the solid and has a possibility of exciting other electrons, plasmons, etc., thus losing energy and appearing as a satellite.

### **Resonant Photoemission**

Resonant Photoemission (RPES) is an extremely useful tool for investigating valence band features in solids. The “resonance” may occur when we perform photoemission with photons of energy  $h\nu$  very close to the absorption threshold of a core level. Electrons of that core level may then be excited into an empty state of the valence band. If the resulting excited system then decays via a super Koster-Kronig process, it will emit an Auger CVV-electron which can interfere with electrons from direct photoemission of the valence band [19].

Typically, RPES occurs for transitions in which the angular momentum selection rule  $\ell \rightarrow (\ell+1)$  permits the transition to a final state of a partially filled inner core, e.g.  $3p \rightarrow 3d$ ,  $4d \rightarrow 4f$ , and  $5d \rightarrow 5f$ . An example for the case of a transition metal is given by:



where  $\varepsilon_k$  represents the emitted electron. Since photoemission occurs by the direct process



ending in the same final state, interference occurs between the two processes.

If a series of EDCs are taken with changing photon energies that pass through the core-absorption threshold, the emission from the resonating state is greatly increased due to the resonance. This can allow one to identify the character of specific features in the EDCs. CFSs and CISs are also used to detect resonances. CFSs will give the photon absorption spectrum of the resonance. CISs measure the cross section of the RPES lineshape at a given initial state. They can then be indicative of the character of that initial state. The lineshape is the Auger emission and direct PES overlap and is called the Fano lineshape [20], given by:

$$N(h\nu) \cong \frac{(\varepsilon + q)^2}{\varepsilon^2 + 1}, \quad \varepsilon = \frac{h\nu - h\nu_j}{\Delta h\nu_j / 2}, \quad (2.19)$$

where  $h\nu_j$  is the photon energy at the core-excitation threshold,  $q$  is a parameter involving the transition matrix elements and the matrix element of the Auger process, and  $\Delta(h\nu_j)$  is the width (FWHM) of the core level.

### **CHAPTER 3: LIGHT SOURCE**

An ideal photon source for photoemission is synchrotron radiation. Synchrotron radiation is the electromagnetic radiation emitted by electrons or positrons moving at relativistic velocities along a curved trajectory with a large radius of curvature. Our experiments were performed at the Aladdin electron storage ring [21] at the Synchrotron Radiation Center in Stoughton, WI.

Synchrotron radiation has several properties which make it an ideal tool for photoemission. Among these are the broad frequency distribution that ranges from visible light through the x-ray region, natural collimation, high intensity, and a high polarization.

At Aladdin, the electrons travel along a path with a circumference of 88.9 m (see Fig. 3.1). After the 108 MeV microtron (located in the south side of the ring) injects the electrons into the storage ring, the rf cavity (located on the North side) quickly increases the energy to 800 MeV - 1 GeV. The electrons are grouped in 15 bunches around the ring. The bunches are replenished in energy by the rf cavity, which has a frequency of 50.582 Mhz. There are twelve bending magnets around the ring, each one bending the beam with a magnetic radius of 2.083 m. The bending magnets are the source of the synchrotron radiation for our experiments.

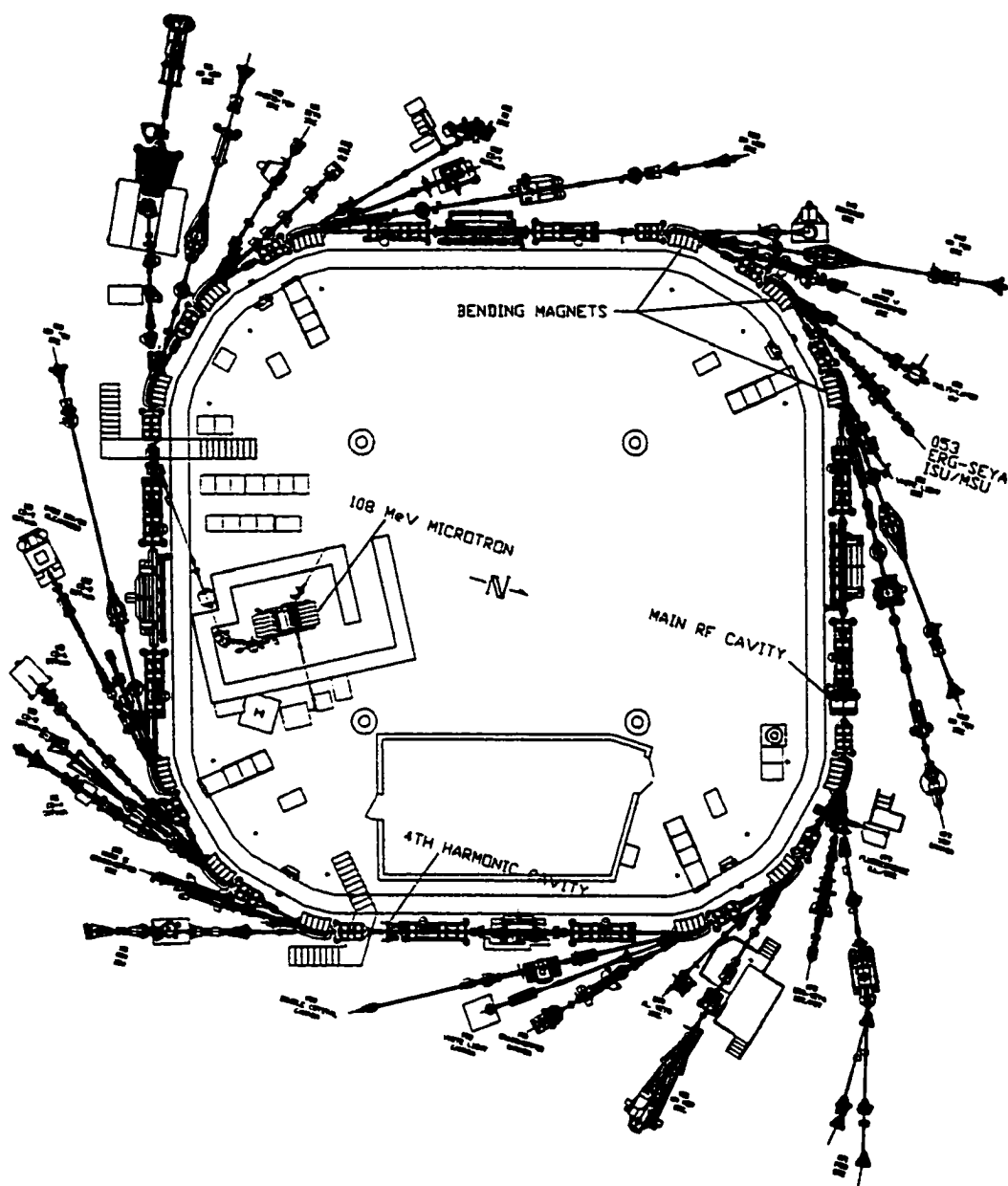


FIG. 3.1 Top view of the Aladdin electron storage ring at the Synchrotron Radiation Center in Stoughton, WI [21]. Each of the twelve bending magnets can support up to three beam lines. Beam line #053 is the Iowa State/Montana State beamline where we performed our experiments. It is detailed later in the chapter.

### Synchrotron Radiation

A charged particle, when accelerated (by a bending magnet, for instance), emits radiation known as “synchrotron radiation”. With a velocity small compared to the speed of light, a charged particle that is accelerated will emit radiation as

$$\frac{dP}{d\Omega} = \frac{e^2}{4\pi c^3} |\dot{\mathbf{v}}|^2 \sin^2 \theta \quad [22]. \quad (3.1)$$

This is the expression for the power radiated per unit solid angle, where  $\dot{\mathbf{v}}$  is the acceleration and  $\theta$  is the angle between the point of observation and the acceleration. It has a dipole pattern, as shown in Fig. 3.2a.

When the particle has a velocity  $\beta = v/c \cong 1$ , the power radiated per unit solid angle becomes strongly dependent on the velocity. Thus the dipole pattern is strongly distorted into the forward direction (see Fig. 3.2b).

For a relativistic particle in instantaneously circular motion (see Fig. 3.3), as in a synchrotron, the equation for the energy radiated per unit frequency interval per unit solid angle is

$$\frac{d^2 I}{d\omega d\Omega} = \frac{e^2}{3\pi^2 c} \left( \frac{\omega \rho}{c} \right)^2 \left( \frac{1}{\gamma^2} + \theta^2 \right)^2 \left[ K_{2/3}^2(\xi) + \frac{\theta^2}{(1/\gamma^2) + \theta^2} K_{1/3}^2(\xi) \right], \quad (3.2)$$

where

$$\xi = \frac{\omega \rho}{3c} \left( \frac{1}{\gamma^2} + \theta^2 \right)^{3/2} \quad \text{and} \quad \gamma = \frac{E}{mc^2} \quad [22].$$

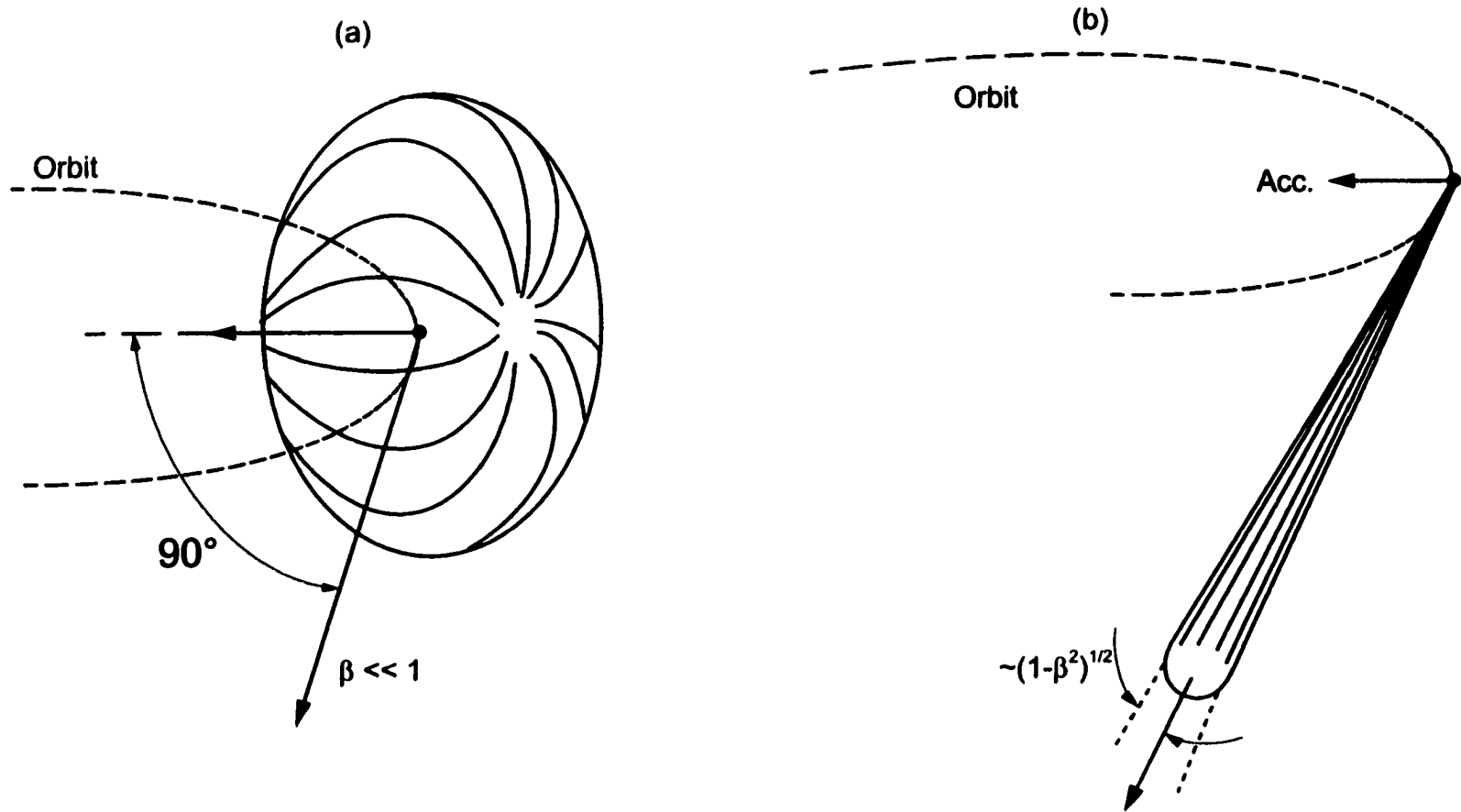


FIG. 3.2 Angular intensity distribution of slow (a) and relativistic (b) electrons on a circular orbit.

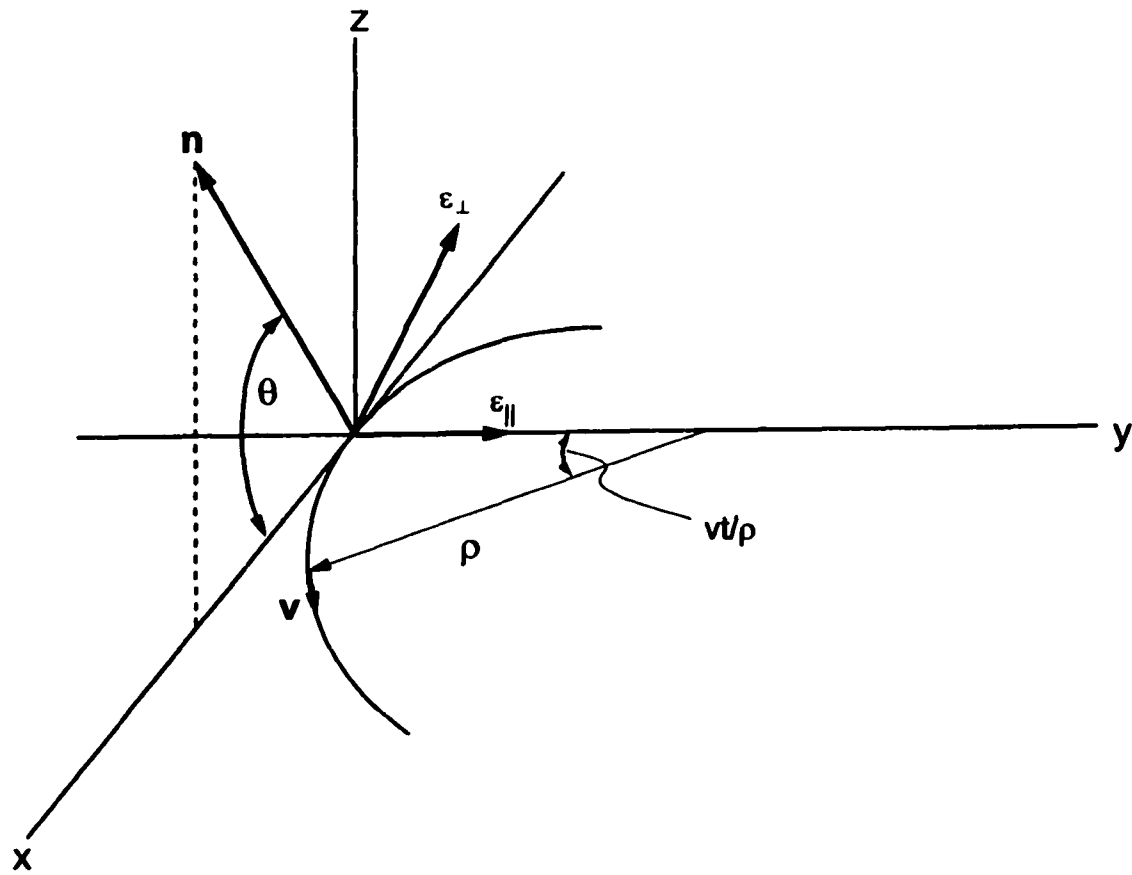


FIG. 3.3 Coordinate system for a relativistic particle in instantaneously circular motion.

$K_{2/3}$  and  $K_{1/3}$  are modified Bessel functions,  $\rho$  is the radius of curvature of the path, and  $\theta$  is the angle of observation above the plane of the path (only for very small  $\theta$  will there be any appreciable radiation). In the figure,  $v$  is the velocity of the particle,  $\rho$  is the instantaneous radius of curvature,  $\mathbf{n}$  is the unit vector in the direction of observation,  $\varepsilon_{\perp}$  and  $\varepsilon_{\parallel}$  are the perpendicular and parallel components of the radiation, respectively. The first term in brackets in (3.2) corresponds to polarization parallel to the orbital plane, and the second to perpendicular polarization. When integrating over all angles, there is seven times as much energy radiated with parallel polarization as with perpendicular polarization. Thus, the radiation is almost completely polarized in the plane of motion of the particle.

While equation 3.2 may be rather intangible, we can use it to analyze other characteristics of synchrotron radiation as well. Firstly, note that one property of the modified Bessel functions,  $K_{\nu}(\xi)$  is that they become negligible for  $\xi \gg 1$ . From the definition of  $\xi$ , we can see that this will occur at large angles and large frequencies. The radiation, then, is most intense at about  $\theta = 0$ . But if the frequency  $\omega$  gets too large,  $\xi$  will be large at any angle. So, there is some cutoff frequency  $\omega_c$  above which the radiation drops off.

We now will quantify Eq. 3.2 a bit to give a feel for the angles and frequencies involved. Looking at the frequency distribution first, we evaluate Eq. 3.2 for  $\theta = 0$ . If we say the frequency cutoff point occurs for  $\xi > 1$ , we find

$$\omega_c = 3 \left( \frac{E}{mc^2} \right)^3 \frac{c}{\rho}. \quad (3.3)$$

For  $\omega \ll \omega_c$ , we find:

$$\left. \frac{d^2 I}{d\omega d\Omega} \right|_{\theta=0} \cong \frac{e^2}{c} \left[ \frac{\Gamma(\frac{2}{3})}{\pi} \right]^2 \left( \frac{3}{4} \right)^{\frac{1}{3}} \left( \frac{\omega \rho}{c} \right)^{2/3} \quad (3.4)$$

and for  $\omega \gg \omega_c$ ,

$$\left. \frac{d^2 I}{d\omega d\Omega} \right|_{\theta=0} \cong \frac{3}{2\pi} \frac{e^2}{c} \gamma^2 \frac{\omega}{\omega_c} e^{-2\omega/\omega_c}. \quad (3.5)$$

Eq. 3.4 shows that for low frequencies, the radiation intensity increases as  $\omega^{2/3}$ . It reaches some maximum around  $\omega_c$ , then, according to Eq. 3.5, drops exponentially to zero for higher frequencies. One can compare this with the photon flux curve of the 800 MeV beam at the SRC, where the bending magnets form a magnetic radius of approximately  $\rho \cong 2$  m (see Fig. 3.4).

To quantify the collimation of the beam, we estimate the spread in angle for a particular frequency. We define the angle  $\theta_c$ , beyond which the radiation quickly drops off, by

$$\xi(\theta_c) \cong \xi(0) + 1. \quad (3.6)$$

Now for a low frequency,  $\omega \ll \omega_c$ ,  $\xi(0)$  will be negligible so  $\xi(\theta_c) \cong 1$ . Thus,

$$\theta_c \cong \left( \frac{3c}{\omega \rho} \right)^{\frac{1}{3}} = \frac{1}{\gamma} \left( \frac{\omega_c}{\omega} \right)^{\frac{1}{3}}. \quad (3.7)$$

For UV radiation of 22 eV,  $\theta_c$  would then be approximately 3 mrad.

For the higher frequencies,  $\omega > \omega_c$ ,  $\xi(0)$  will be large compared to unity and the intensity will fall off with angle approximately as

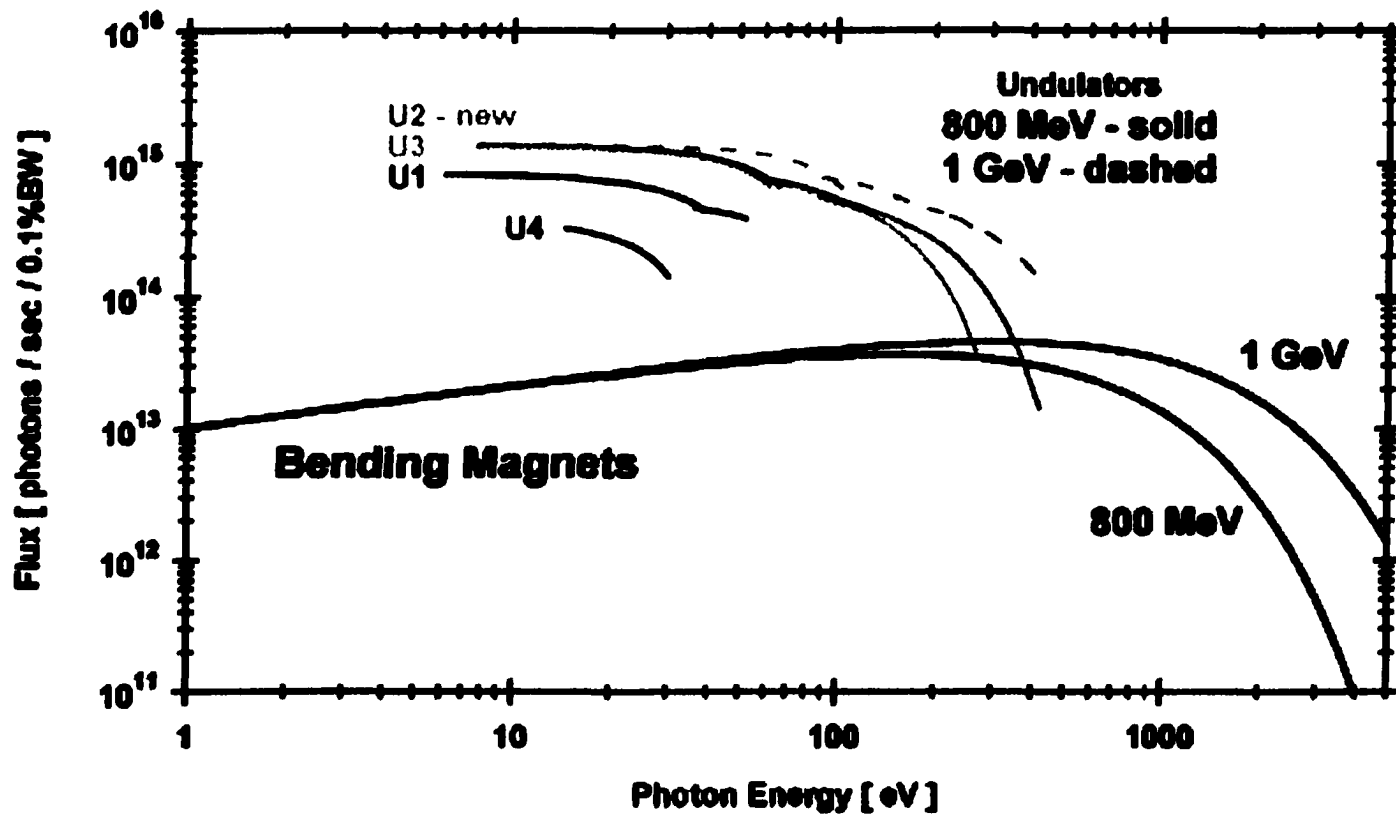


FIG. 3.4 Flux curves for a 200 mA beam current at Aladdin. The bending magnet plots are for 10 mrad horizontally [23].

$$\left. \frac{d^2 I}{d\omega d\Omega} \right|_{\omega > \omega_c} \propto e^{-3\omega\gamma^2\theta^2/\omega_c}. \quad (3.8)$$

If we define the critical angle by the 1/e point, we have

$$\theta_c \equiv \frac{1}{\gamma} \left( \frac{\omega_c}{3\omega} \right)^{1/2}. \quad (3.9)$$

Comparing this to the low-frequency  $\theta_c$ , we note the intensity drops off quicker with angle as we go higher in frequency. So the limit to the height of the beam of light is about 3 mrad.

### Synchrotron Beamlines

In order to select the photons from the synchrotron source to a specific energy, one uses a monochromator. All of the photoemission measurements in our experiments were performed on the Ames/Montana ERG/Seya combined monochromator beamline at the SRC. The ERG/Seya beamline was built by Dr. C.G. Olson [24].

The ERG and the Seya monochromators are configured so that they use the same final refocusing mirror. Light from either monochromator will then be incident on the sample from the same direction and focused at the same spot. Transfer between the two monochromators is accomplished by a cooled photon shutter at the front end of the beamline. The layout of the two monochromators is given in Fig. 3.5.

At the core of the monochromator is the grating. The gratings diffract the incident radiation, dispersing its component wavelengths. Both the ERG and the Seya utilize

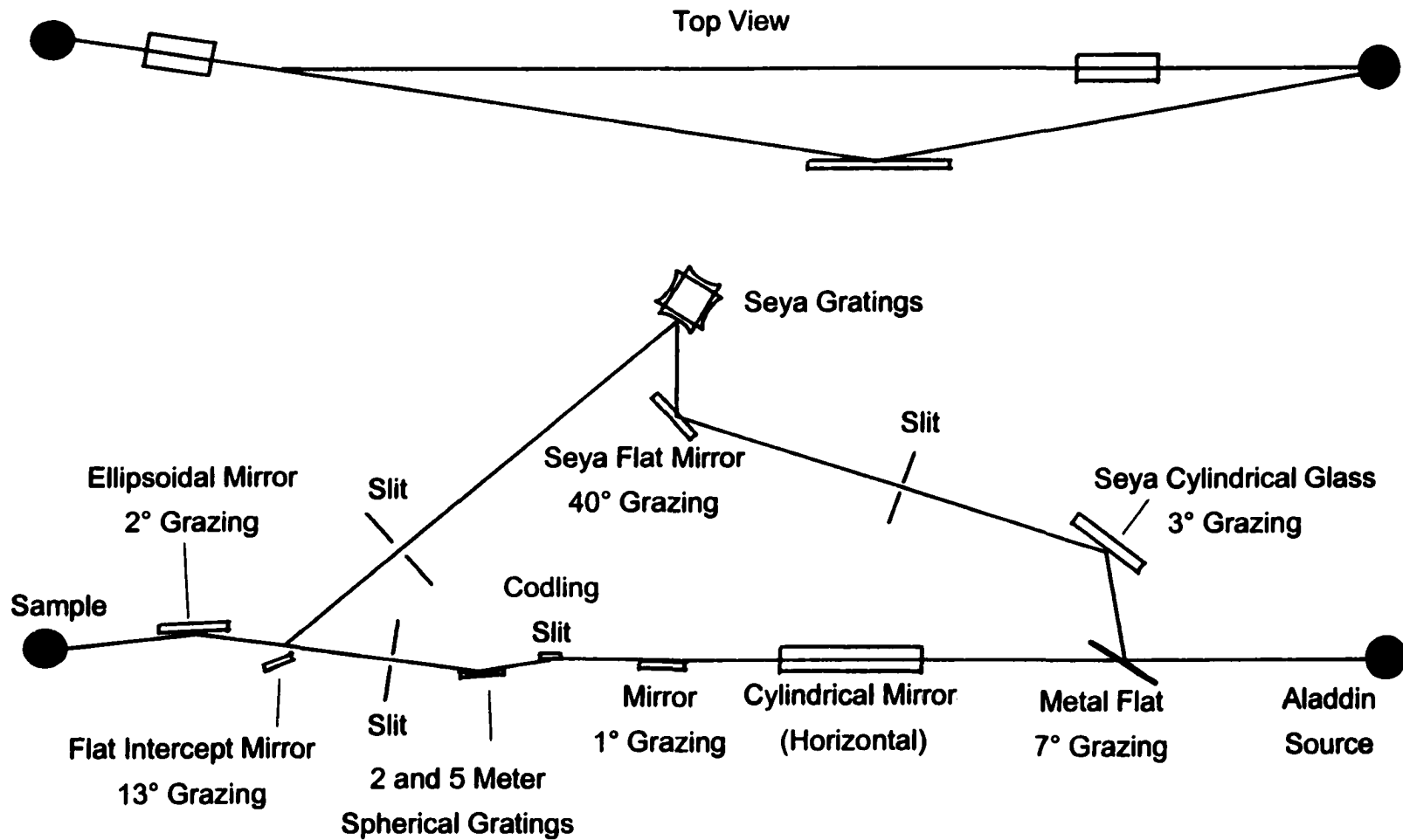


FIG. 3.5 Schematic layout of the Ames/Montana ERG/Seya combined monochromator beamline (after [24]).

spherical gratings. Spherical gratings have an advantage over plane gratings due to their focusing properties. If a spherical grating is placed tangentially to a circle of a diameter equal to the radius of curvature of the grating such that the grating center lies on the circumference, the spectrum of an illuminated point lying on the circle will be focused tangentially (in the plane of reflection) on this circle (see Fig. 3.6). The circle is called the Rowland circle after Prof. H. A. Rowland who conceived the idea of the spherical grating in 1882 [25]. The sagittal focus (normal to the reflection plane) of the spectrum will be on a straight line tangent to the Rowland circle at the normal to the grating (as seen in Fig. 3.6).

The ERG, or Extended Range Grasshopper, uses a constant-deviation Rowland-circle geometry at extreme grazing incidence [26]. Its extended range comes from having two interchangeable gratings, with two and five meter radii of curvature. The basic geometry of the ERG is shown in Fig. 3.7. It is designed to move so that the exit slit is always on the Rowland circle, allowing one to change the wavelength while retaining a focused beam and constant direction. The figure shows two positions of the monochromator, one at zero order, and the other giving a wavelength of  $\lambda$ . The grazing angles are exaggerated for clarity.  $\psi$  is the exit angle (a constant, as is  $\alpha$ ),  $r$  is the radius of the Rowland circle,  $M_0$  and  $M_1$  are cylindrical mirrors,  $S_1$  and  $S_2$  are the entrance and exit slits, respectively, and  $G$  is the location of the gratings when being used.

The first mirror,  $M_0$  collects and focuses the beam onto the exit slit in the horizontal plane. The mirror  $M_1$  focuses the beam onto the entrance slit with a demagnification of 7 to 9. This allows greater flux to pass through the slit, as well as a

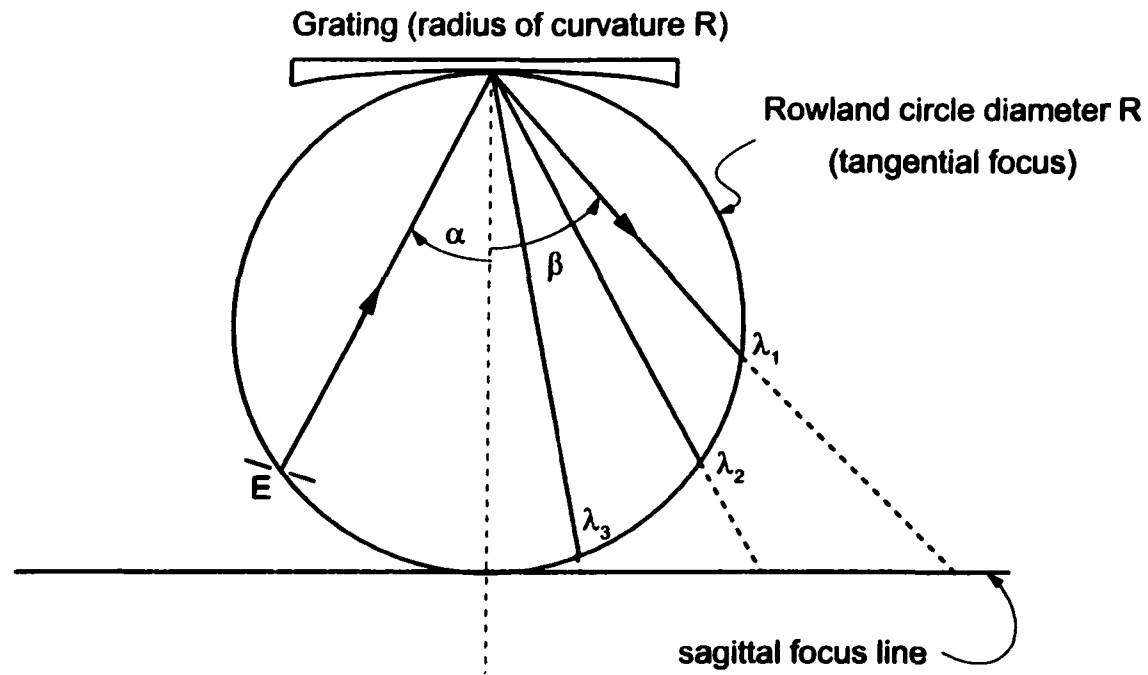


FIG. 3.6 The Rowland circle. Radiation from the point E is dispersed and focused by the grating at  $\lambda_1$ ,  $\lambda_2$ , etc.  $\alpha$  and  $\beta$  are the angles of incidence and diffraction, respectively. Diffracted radiation is focused tangentially on the Rowland circle, and sagittally on the line tangent to the circle at the normal to the grating.

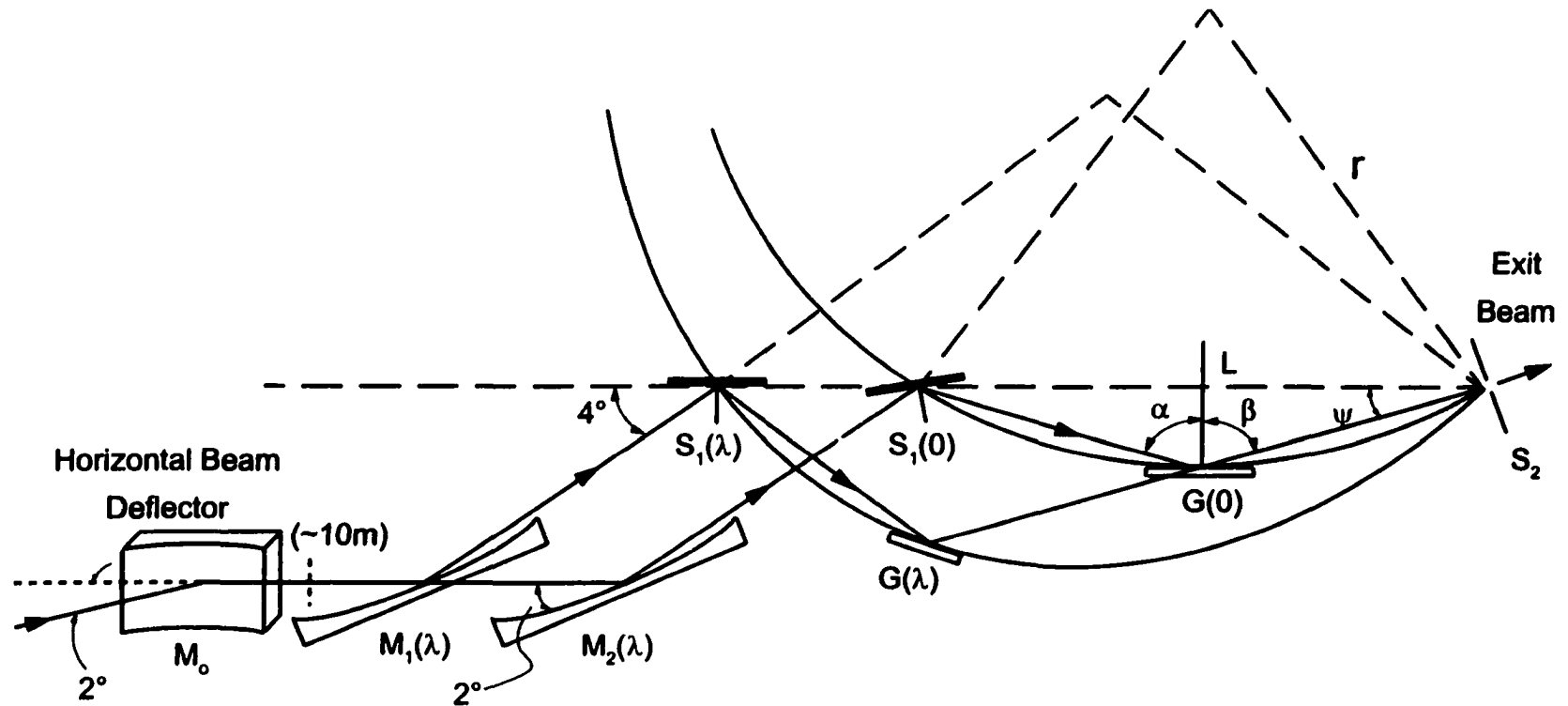


FIG. 3.7 Basic geometry of the ERG shown for zero order and some wavelength  $\lambda$ .  $G$  is one of two possible gratings (a 2 meter and 5 meter).

better resolution due to having more rulings illuminated. In scanning the monochromator, the Rowland circle rotates about  $S_2$  to give a constant exit beam direction. The grating is mounted on an arm  $\overline{SG}$  which pivots about  $S_1$  and together with  $M_1$ , translates horizontally along  $L$ .  $S_1$  pivots through half the angle that  $G$  rotates in order to keep  $\alpha$ , and thus  $\psi$ , constant. The grating refocuses the beam from  $M_1$  in the vertical plane onto the exit slit. We thus end up with a stigmatic image at  $S_2$ .

The Seya's scanning mechanism is much simpler than the ERG's. It consists of rotating the grating about an axis through the plane of the grating (normal to the plane of reflection). Normally, this would give an unfocused spot as one scanned wavelengths with fixed entrance and exit slits. However, in 1952, Seya [27] analyzed the focusing conditions for a simple rotation of the grating and found that a good focus could be obtained over a large spectral range if the slits subtended an angle of about  $70^\circ$  at the grating. The basic geometry of the Ames/Montana Seya is shown in Fig. 3.8 at zero order. To obtain a stigmatic image at the exit slit,  $S_2$ , the beam is allowed to expand continually in the sagittal direction from the source to the grating  $G$ . It is then focused by  $G$  onto  $S_2$ . The cylindrical mirror  $M$  focuses the beam onto the entrance slit  $S_1$  in the tangential direction. The Ames/Montana Seya contains a grating-changing mechanism which hold four gratings that differ in ruling density. Changing the ruling density changes the wavelength associated with scan angle, so the Seya can maintain high resolution at the shorter wavelengths.

After being focused into a stigmatic image on the exit slits, beam from both the Seya and the ERG impinge upon the refocusing mirror (Fig. 3.5). When the Seya is

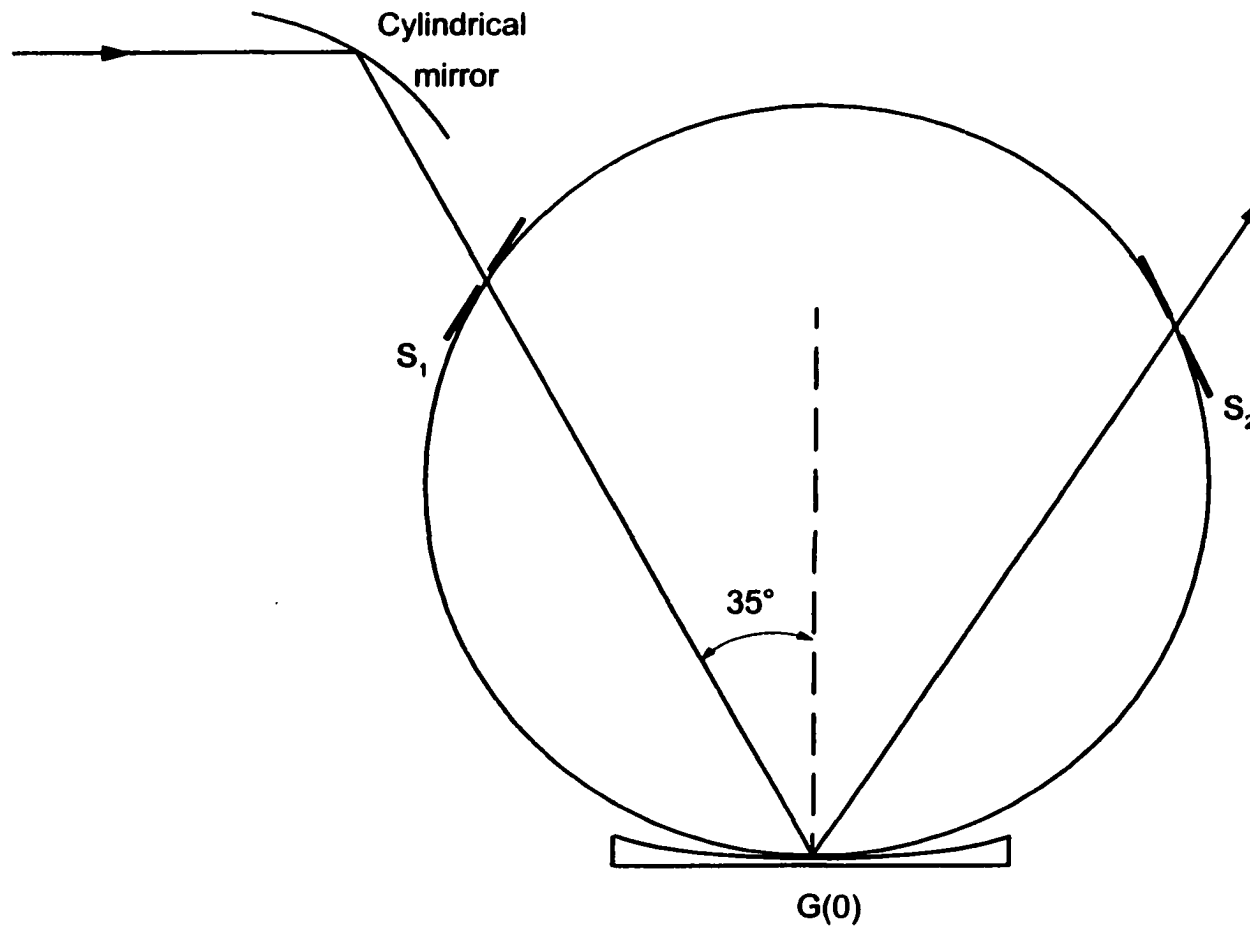


FIG. 3.8 The basic geometry of the Ames/Montana Seya for zero order.

illuminated, an intercept mirror is put in place to image the Seya's exit slit onto that of the ERG's. The refocusing mirror then focuses the exit slit onto the sample.

The photon energy range covered by the two gratings of the ERG is 38 eV to about 1000 eV and overlaps with the range of the Seya which is from 5 eV to 40 eV. Figure 3.9 shows the range and dispersion of all the possible beamline gratings. The resolutions indicated correspond to 10 micron slits for the ERG, and 200 micron slits for the Seya. The tick marks indicate the optimum range for each grating. The flux from the Seya gratings is given in Fig. 3.10.

### **Electron Energy Analyzer**

After ejection, the photoelectrons are detected by an electron energy analyzer. In our experiments, a VSW (Vacuum Science Workshop) Model HA50 hemispherical electron energy analyzer [28] was used. This analyzer is mounted on a goniometer which allows rotation in both the horizontal and vertical planes.

The analyzer itself consists of retarding lenses at the entrance aperture, two concentric hemisphere deflectors of mean radius  $R_0$  to disperse the electrons, and a single-channel electron multiplier at the exit of the deflectors (see Fig. 3.11). An incoming photoelectron will first be retarded to the given pass energy  $E_0$  by the retarding lenses. It then enters the deflectors. A potential is applied between the surfaces so that the outer surface is negative and the inner is positive with respect to the median equipotential surface between the hemispheres. A photoelectron will then be selected if

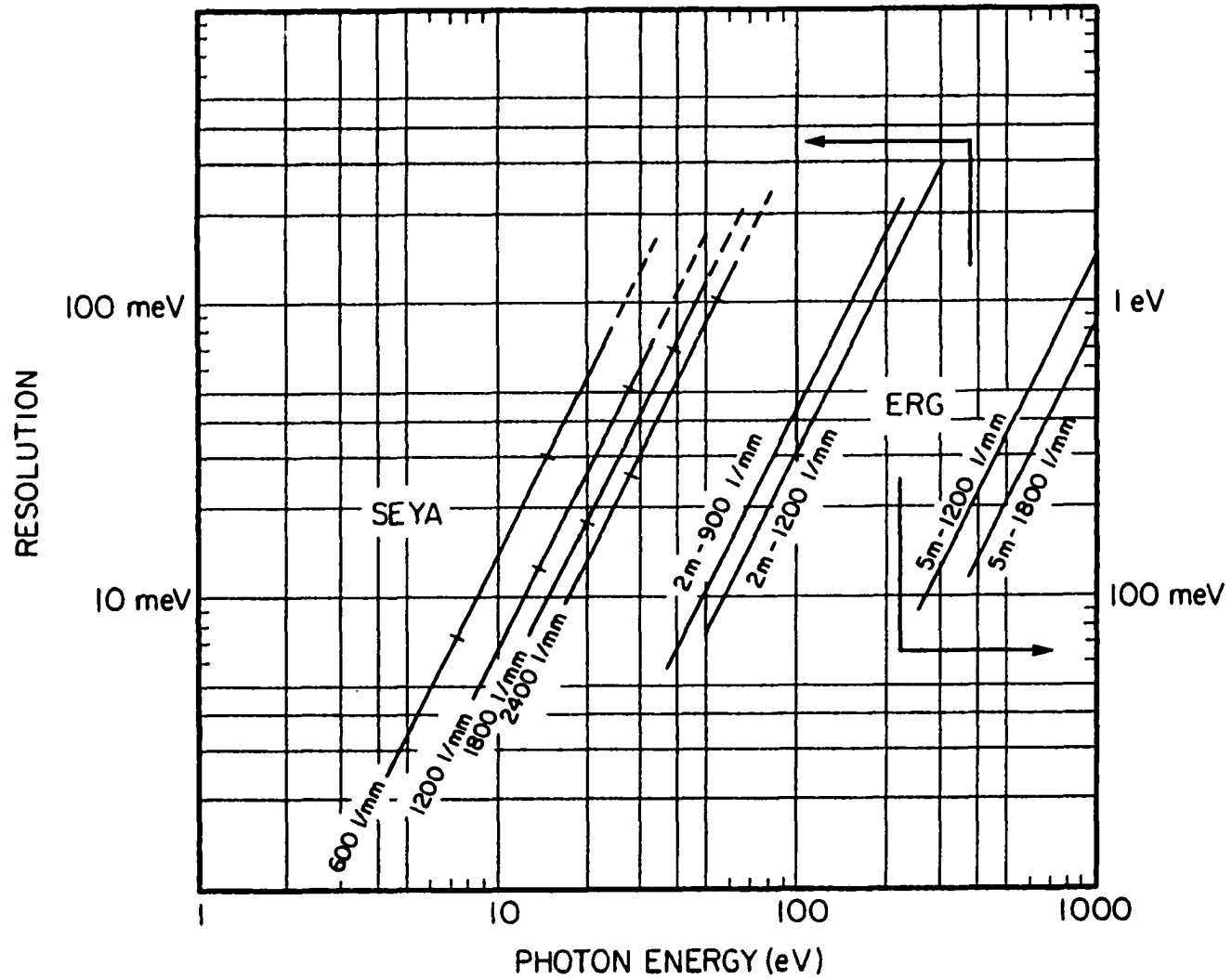


FIG. 3.9 Spectral range of the possible beamline gratings. The indicated resolutions correspond to 10  $\mu\text{m}$  slits for the ERG, and 100  $\mu\text{m}$  slits for the Seya [24].

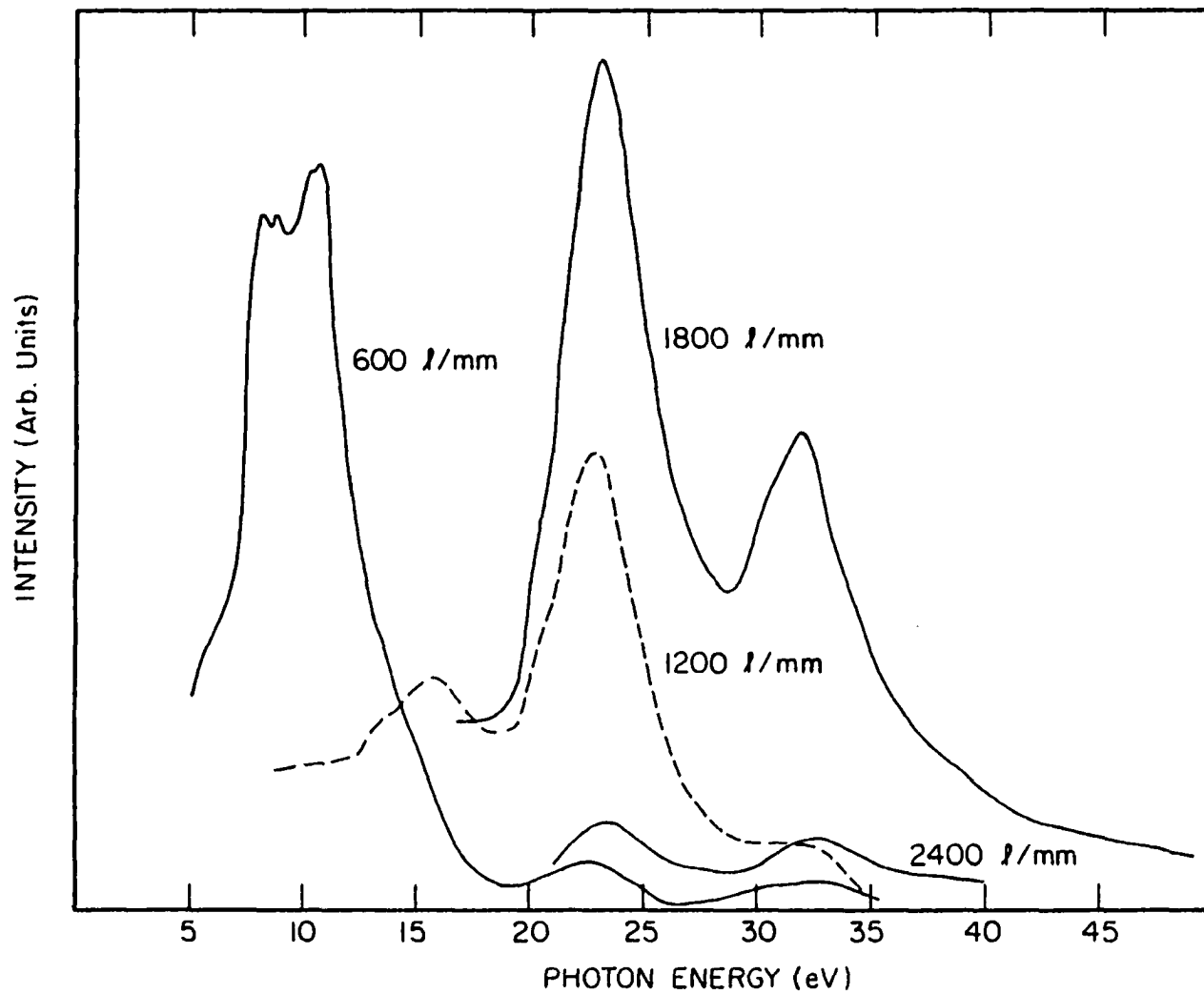
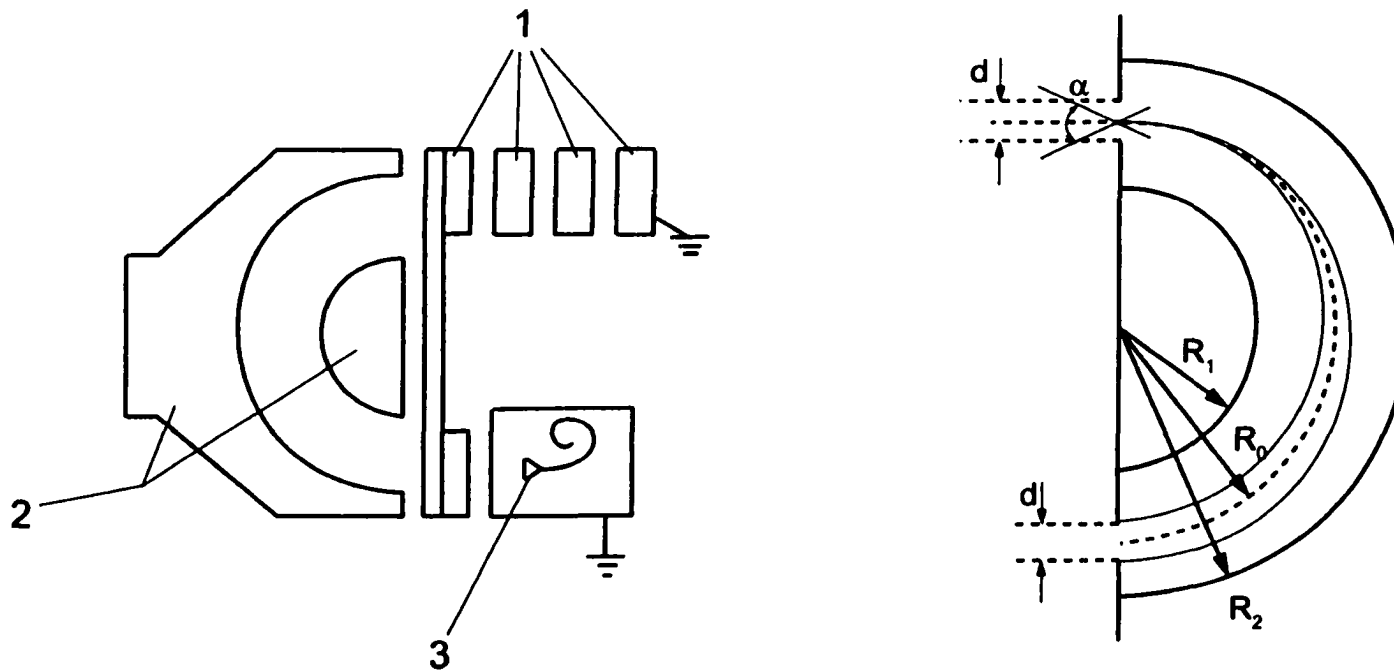


FIG. 3.10 Spectral output of the Seya. The intensities of the three higher gratings have been normalized to the bandpass of the 600 l/mm grating [24].



**FIG. 3.11 Schematic Diagram of the Concentric Hemispherical Analyzer. In the left figure, 1) denotes the entrance lenses, 2) denotes the hemisphere deflectors, and 3) denotes the channeltron. The right figure is a more detailed view of the hemisphere deflectors.**

the following relation is true:

$$E_o = \frac{eV}{\left( \frac{R_2}{R_1} - \frac{R_1}{R_2} \right)}$$

where  $e$  is the charge of an electron,  $V$  is the potential difference between the outer and inner hemispheres (the band pass),  $R_1$  is the radius of the inner sphere, and  $R_2$  is the radius of the outer sphere.

The energy resolution of the analyzer is given approximately by

$$\Delta E = E_o \left( \frac{d}{2R_o} + \frac{\alpha^2}{4} \right)$$

where  $d$  is the slit width,  $R_o$  is the mean radius of the hemispheres, and  $\alpha$  is the full angle of electrons entering the analyzer (at the entrance slit).  $\alpha$  is the angular resolution of the experiment, and in our case is equal to  $2^\circ$ .

## **CHAPTER 4: RESULTS AND DISCUSSION**

### **Photoemission Study of MnBi**

Originally, this experiment intended to utilize angle resolved photoelectron spectroscopy (ARPES) to determine the band structure of single-crystal MnBi samples and compare the experimental results to the theoretical results of the publications listed in the introductory chapter. Complications arose when cleaving the samples to obtain a clean surface. Cleaves were anticipated to be smooth cleaves of the (0001) surface. Instead, while cleaves were still oriented parallel to the (0001) plane, they were glassy and resulted in mountainous surfaces.

Although the surfaces were not ideal, we believe that the photoemission spectra taken are representative of bulk MnBi. This is after the work of L.C. Davis [29] who showed that for copper, the effect of stepped surfaces on the bulk band structure measured by photoemission was negligible. As our sample was not a smooth, prepared stepped surface, but rather, can be looked upon as a conglomeration of a great many stepped surfaces of no regularity, we expected there to be inelastic scattering at the surface.

We do report seeing a large inelastic scattering intensity in the valence band

spectra (detailed later). This background intensity made it very difficult to see the dispersion of the photoelectron intensities. We were, consequently, unable to find any symmetry in the  $k_{\parallel}$  directions (making it impossible to compare complete bandstructures). Symmetry was found in the normal direction, however. Thus, we were able to utilize ARPES in the normal direction. For the other measurements, we continued the experiment as AIPES, which gives a more complete sampling of momentum space.

In the following, we shall examine the valence band of MnBi with AIPES and ARPES using synchrotron radiation. We can determine the shape and features of the DOS and compare them to calculations. Resonant photoemission will be used to distinguish the general character of the valence band. Normal-emission scans with varying photon energies will be analyzed. Lastly we will examine the shallow core levels with AIPES.

MnBi crystallizes in the hexagonal NiAs structure and is shown in Fig. 4.1. The experimental lattice parameters are  $a = 4.170\text{\AA}$  and  $c = 6.126\text{\AA}$  [4]. Single crystals of MnBi were provided by Ian Fisher and Paul Canfield of the Ames Laboratory (DOE). The crystals were grown out of a binary melt with 10 atomic percent Mn and 90 atomic percent Bi. The binary melt was slow cooled from 410 to 272° C, with the excess liquid being decanted at the lower temperature (see Fig. 4.2 for the binary phase diagram). Note in the binary phase diagram that there is no width of formation for  $\alpha\text{MnBi}$ , this, and the fact that we found no stoichiometry issues in the literature, lead us to believe that the composition of the crystals does not deviate significantly from the expected 1:1 ratio.

Before mounting the crystals in the vacuum chamber, Laue diffraction patterns were taken to determine the crystals' orientation. Figure 4.3 shows the Laue diffraction

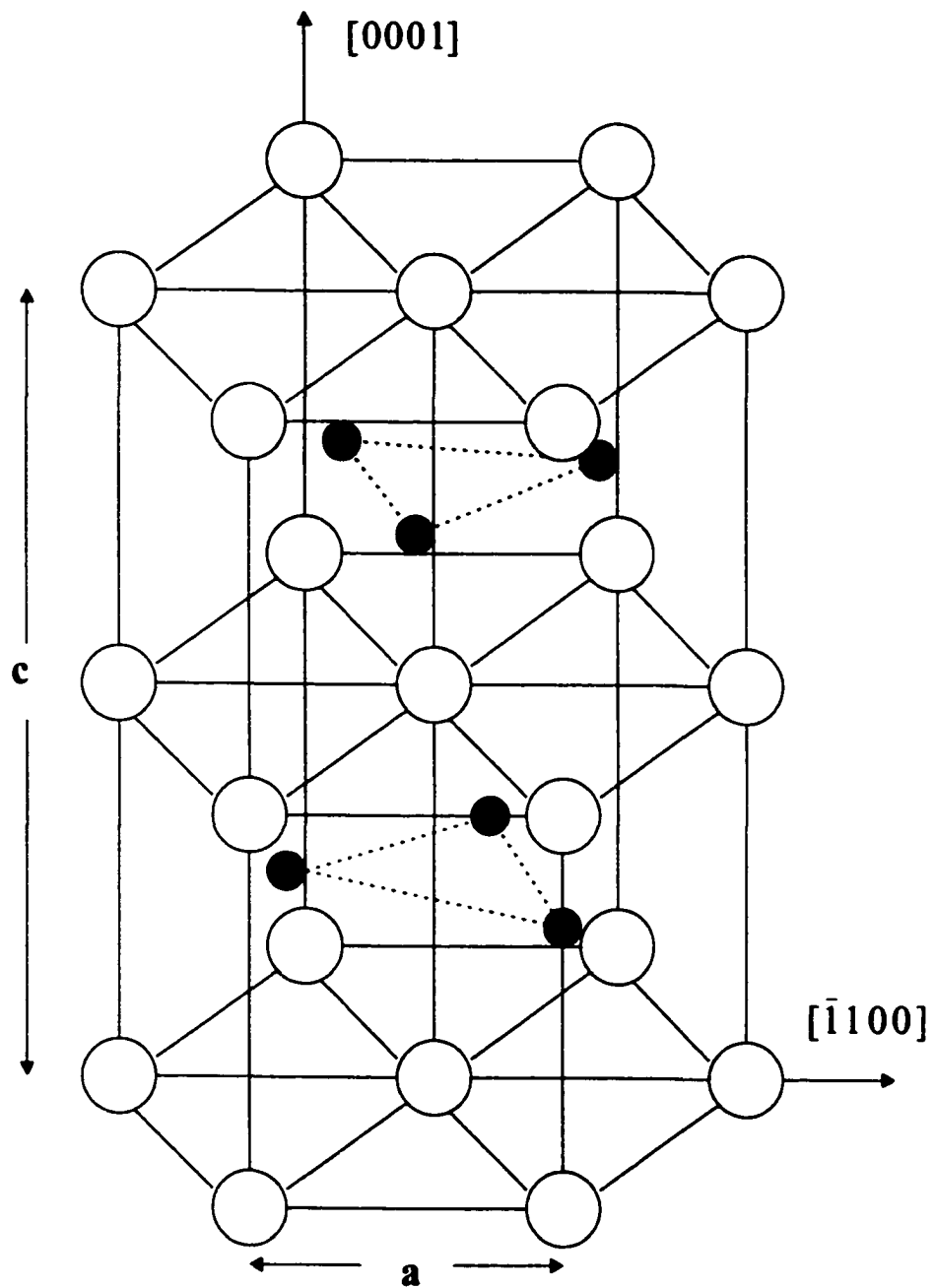


FIG. 4.1 Crystal structure of MnBi. The white balls represent the Mn atoms and the black balls represent the Bi atoms.

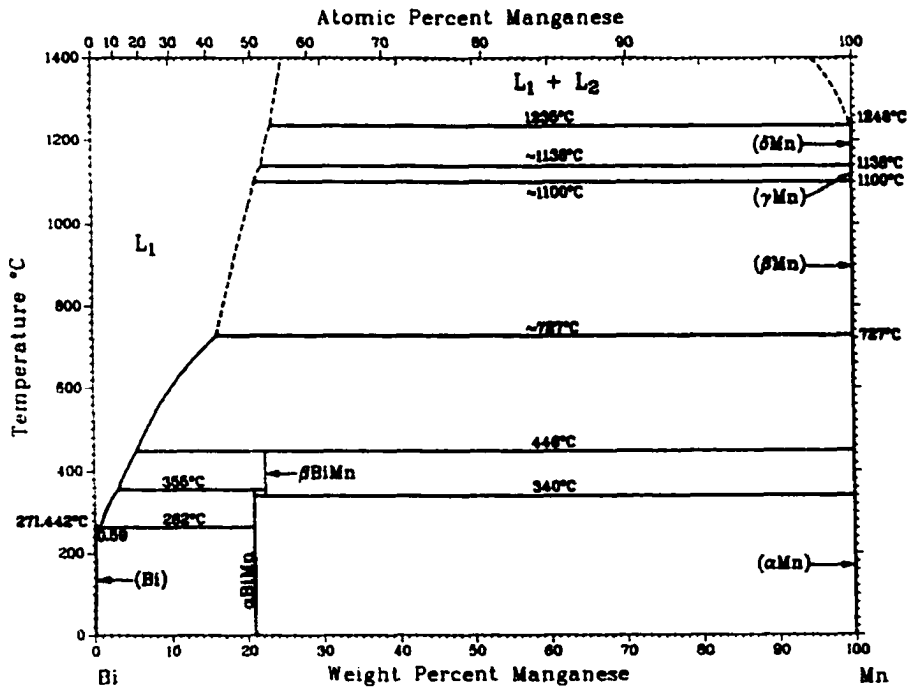
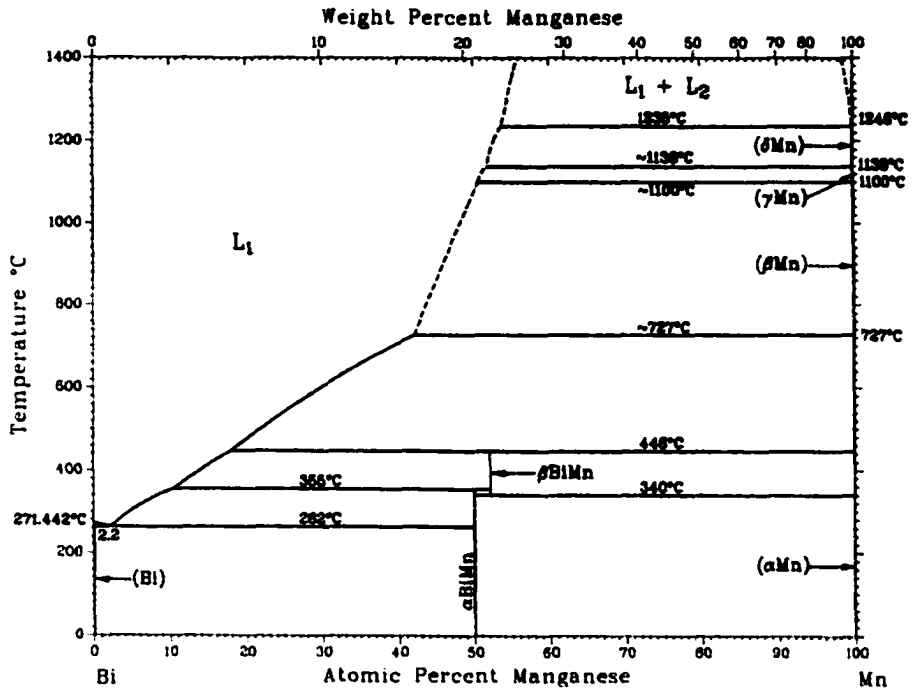


FIG. 4.2 Bi-Mn binary phase diagram [30].

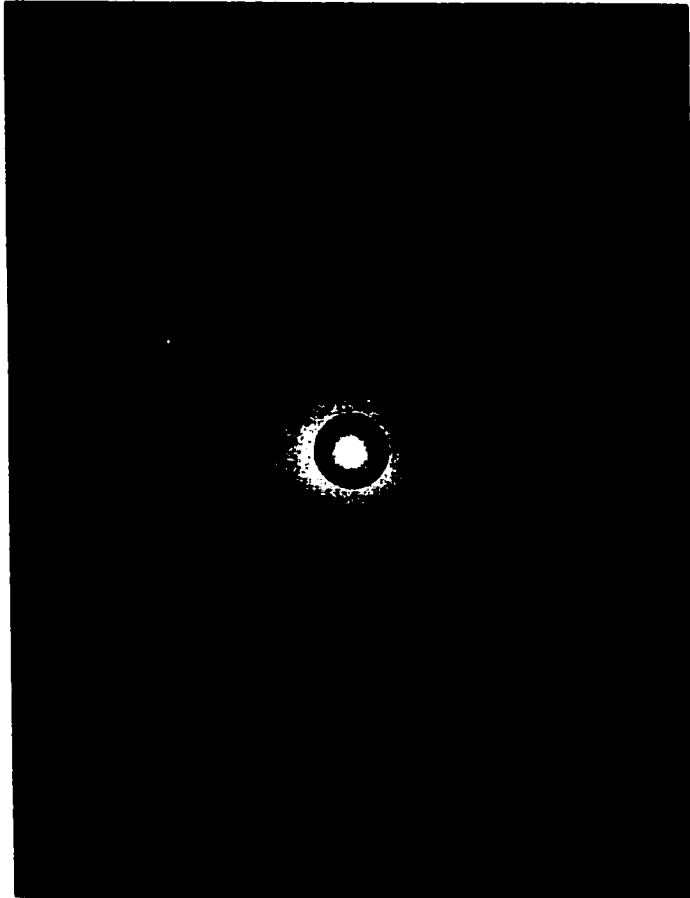


FIG. 4.3 Laue diffraction pattern of MnBi along the [0001] direction.

pattern of MnBi, revealing that the [0001] direction (c-axis) is the surface normal. The 6-fold symmetry is clearly visible. During the experiment, crystalline Bi inclusions were found to exist inside the MnBi samples. After their discovery, however, they were easily detectable and avoided. Details on this will be given later.

The MnBi samples were mounted on aluminum posts with Torr-Seal epoxy. These posts were then attached to the end of the copper cold finger of a closed-cycle helium refrigerator. Electrical contact was made by applying a thin layer of Aqua-Dag over the Torr-Seal epoxy. Clean surfaces were produced by cleaving the samples in the sample chamber under a pressure of lower than  $4 \times 10^{-11}$  Torr, and at a temperature of less than 20 K. The experiments were also conducted with a pressure of lower than  $4 \times 10^{-11}$  Torr. The temperature of the samples was measured with a Chromel-CuFe thermocouple. During the experiment, the temperature was kept under 20 K. At this temperature the sample is ferromagnetic.

Figure 4.4a shows a 15 eV wide scan of the valence band with the background subtracted out, taken with a photon energy of  $h\nu = 85$  eV (with a resolution of 0.36 eV). Calculations show the majority of the intensity is due to the Mn-3d states, especially in the largest peak [5] (see Fig. 4.5). MnBi is clearly metallic by noting the large intensity at the Fermi edge. The width of the valence band is approximately 12 eV. At these high energies, the scans varied little with photon energy. Thus, we can assume that final state effects are minimal, and that Fig. 4.4a has the general shape of the total density of states (DOS). Figure 4.4b shows the calculated spin-projected density of states for MnBi [5] (the total DOS is the sum of the spin-up and spin-down densities of states). Our

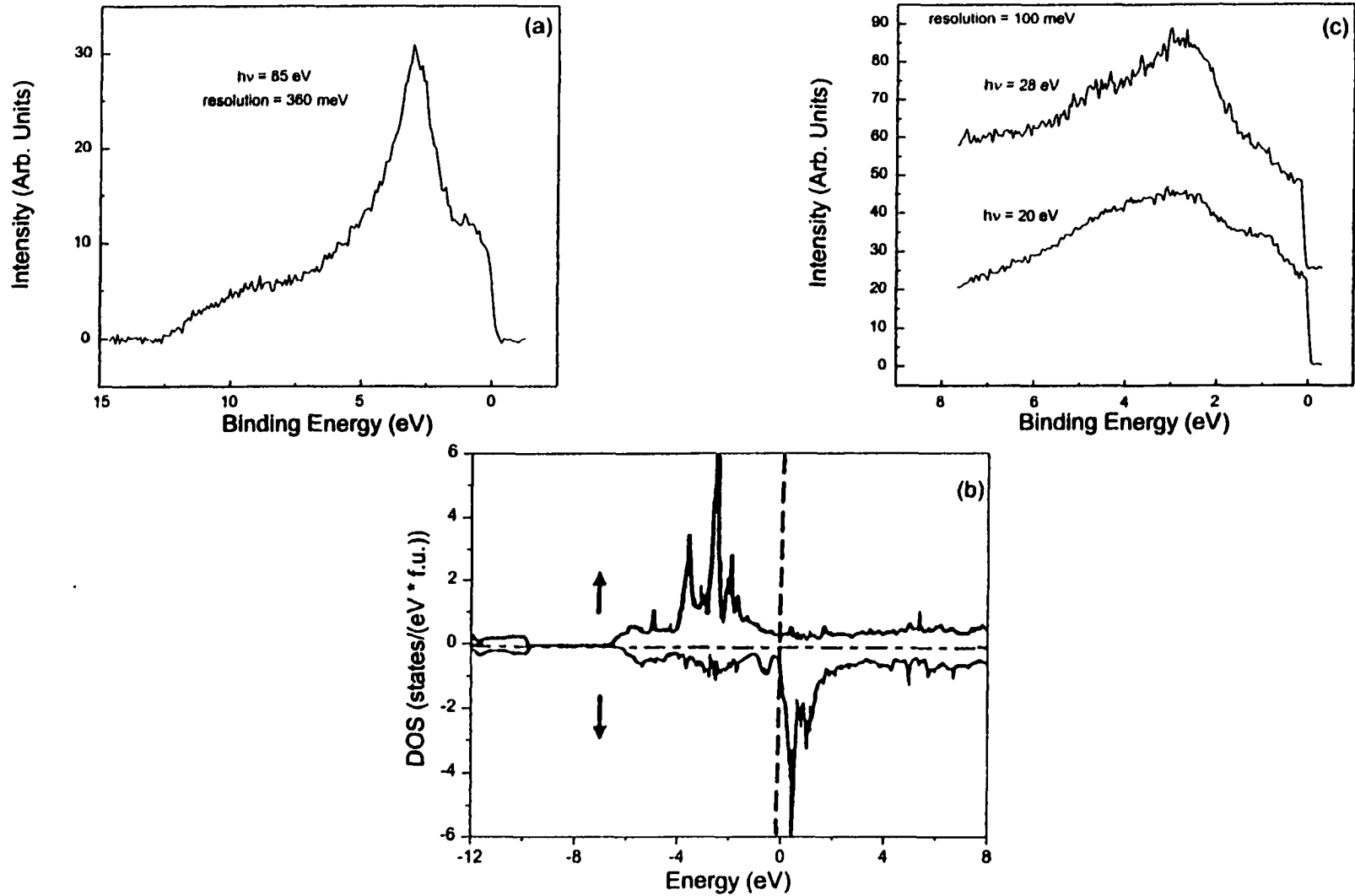


FIG. 4.4 Comparison of photoemission spectra of the MnBi valence band (a), and the spin-projected total density of states (b) [5]. Part (c) shows spectra with better resolution than (a), but are not good representations of the density of states.

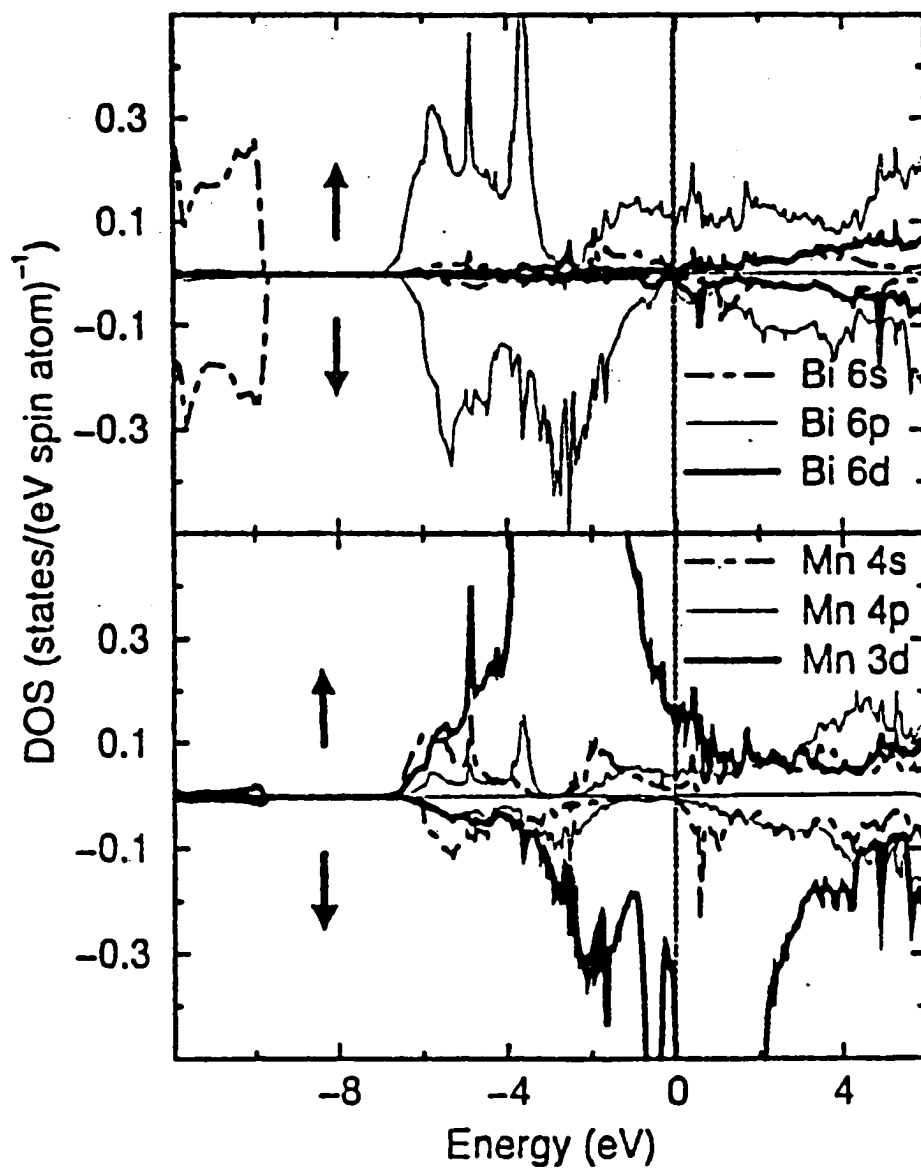


FIG. 4.5 The spin-projected angular momentum and site decomposed density of states of MnBi obtained from the s-o included FLMT0 method. [5]

measurement compares very well with the calculation, especially in the location of the largest peak at 2.5 eV binding energy (BE). The experimental scan shows a much greater intensity at the Fermi edge, however. Also, while the DOS in Fig. 4.4b approaches zero at about 6.5 eV, there is no absence of intensity in Fig. 4.4a. We expect that some of this intensity is due to inelastic scattering of the photoelectrons from the rough surface (as mentioned earlier). The resolution of the scan in Fig. 4.4a is 360 meV. To compare to higher-resolution scans, figure 4.4c contains two 8 eV wide scans of the valence band with resolutions of 100 meV. Note that a direct comparison of intensities is not possible, as the 4.4c scans do not represent the DOS since they only sample a small part of the Brillouin zone.

We now take a look at the orbital character of the valence band. To look for Mn-3d character, we utilize resonant photoelectron spectroscopy (RPES). We expect to see resonant behavior as we vary the photon energy through the Mn 3p→3d core-absorption threshold ( $h\nu \cong 47$  eV). Figure 4.6 shows four scans, one at an energy below threshold ( $h\nu = 45$  eV), and three above ( $h\nu = 51, 53,$  and  $55$  eV). We do, indeed, see a large resonance, and the fact that the scans above threshold are so greatly enhanced shows that there is a great deal of Mn-3d character throughout the valence band. In the top three scans, the vertical lines show the MVV Auger peak (due to ejection of a valence electron into the vacuum and simultaneous de-excitation of a valence electron to the M atomic shell) as it moves through the valence band spectra with changing photon energy.

Figure 4.7 shows four CIS scans taken at different states through the valence band with the photon energy passing through the Mn 3p→3d threshold ( $h\nu \cong 47$  eV). All of

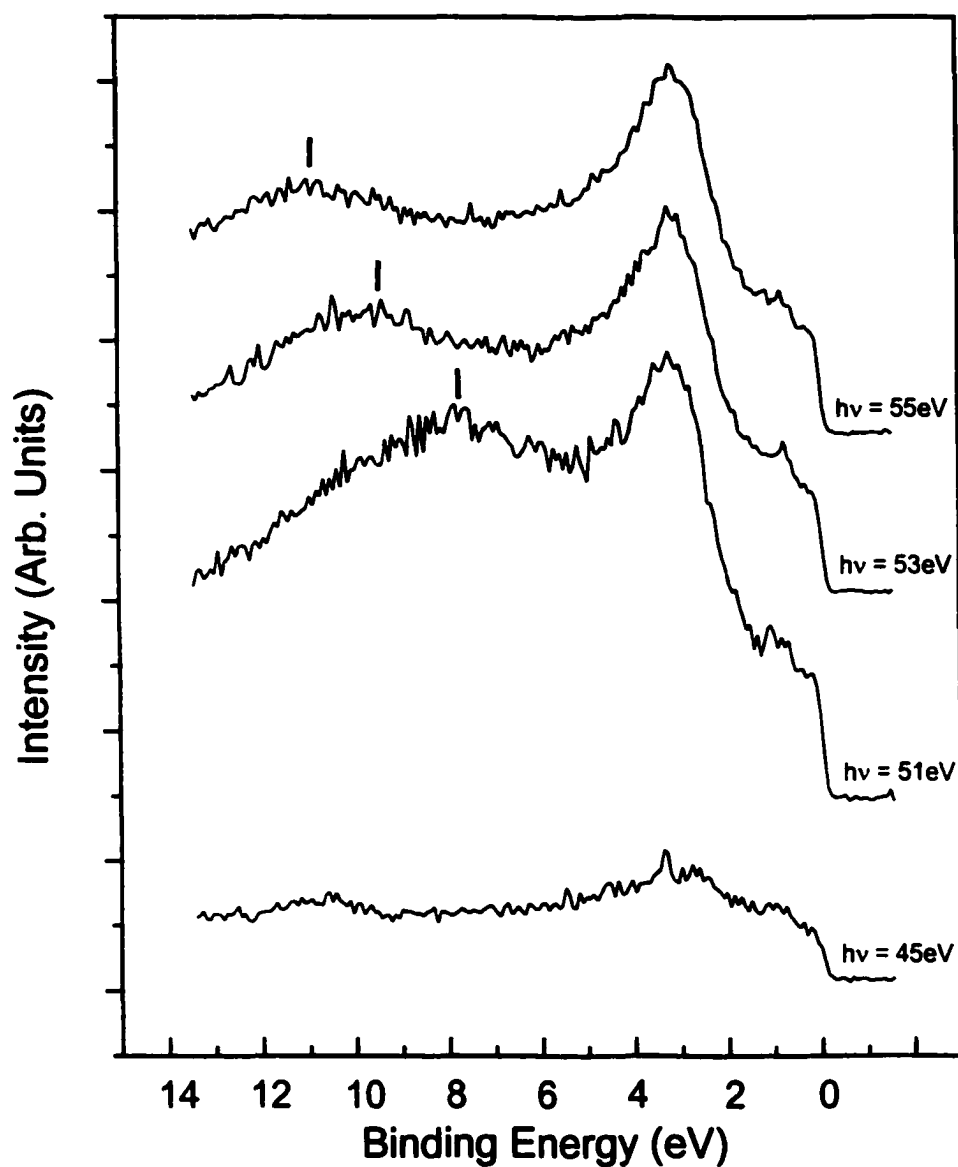


FIG. 4.6 Using resonant photoemission to identify Mn-3d character within the valence band. The bottom scan is taken at a photon energy below the Mn 3p - 3d core absorption threshold, while the top three scans are taken at energies above threshold. The vertical lines indicate the position of the MVV Auger peak as it moves through the valence band.

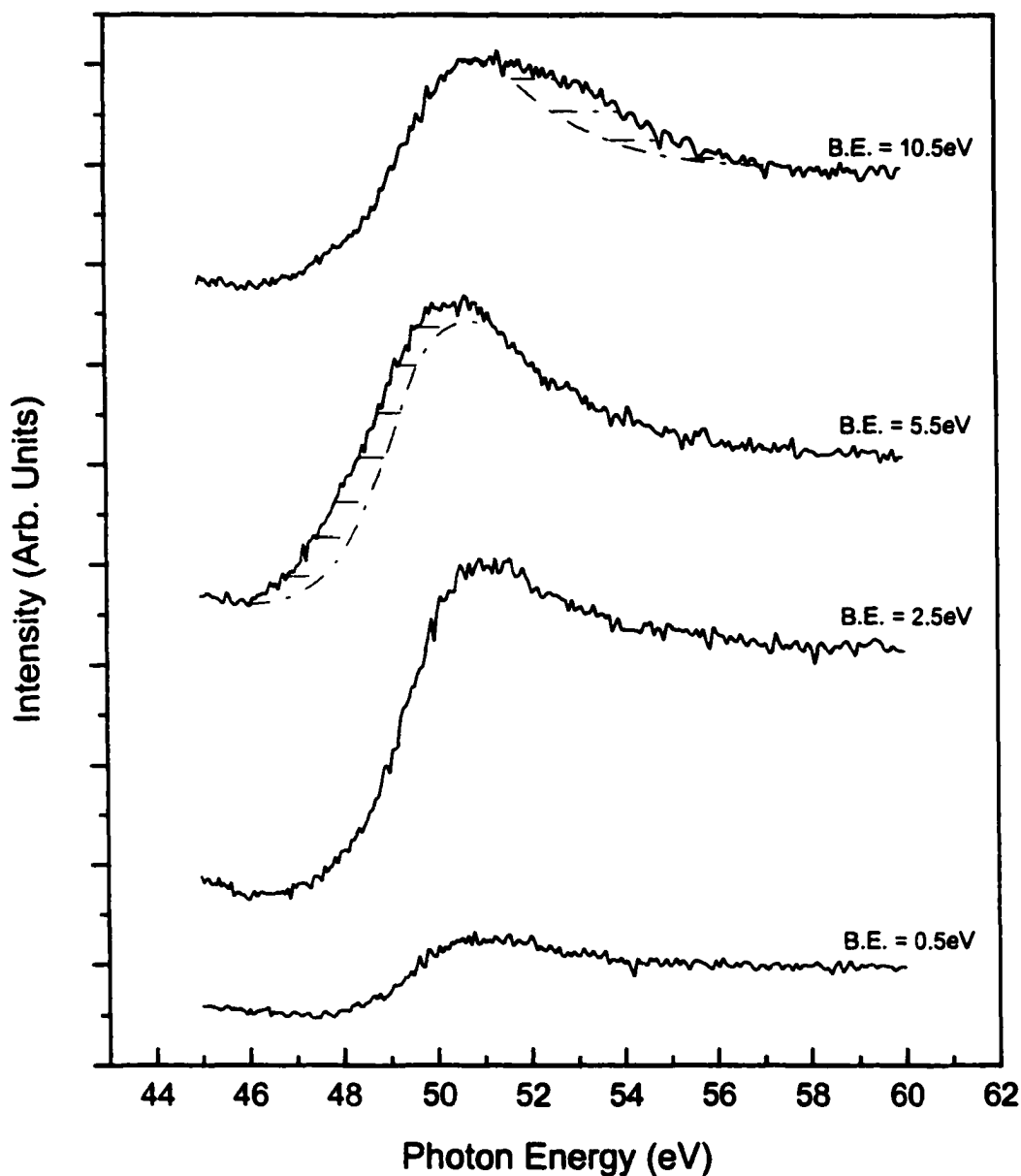


FIG. 4.7 Constant initial-energy (CIS) scans taken at different locations throughout the valence band. The Fano lineshapes [31] in the scans indicate resonance due to Mn 3p - 3d transitions, thus showing Mn-3d character is present in the valence band. Extra intensity indicated in a few of the peaks is caused by the Auger electrons.

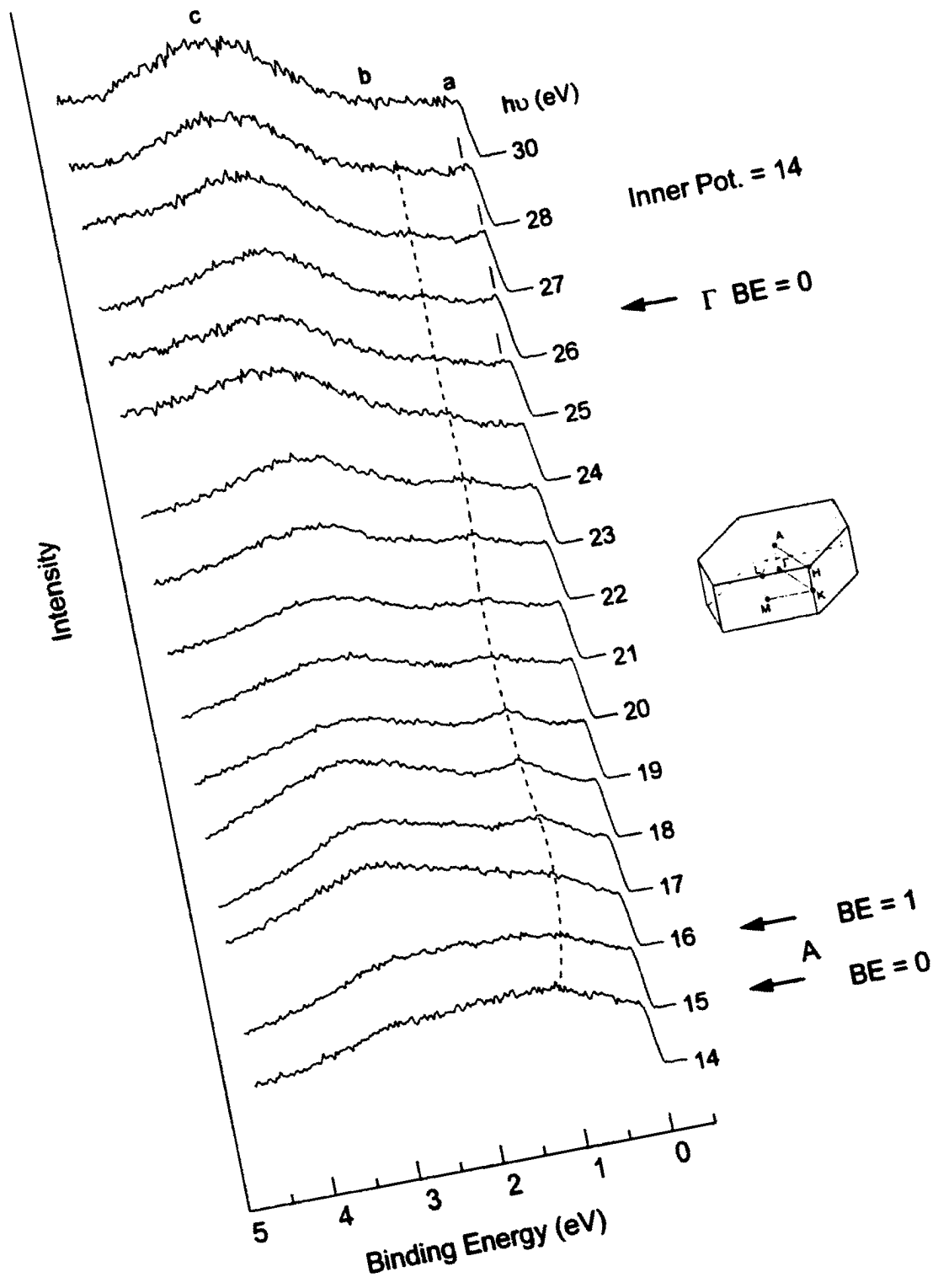
the scans show the Fano line shape [31] signifying the existence of the Mn 3d resonance. The relative size of the enhancement at 0.5 eV BE suggests that there is much less 3d character here than elsewhere in the valence band. As one would expect, the largest strength is at a BE of 2.5 eV (the location of the largest 3d derived peak in the DOS). As we move to higher binding energies, the intensity slowly increases, though even as far out as 10.5 eV there is still much more intensity than at 0.5 eV. Again, although this is contrary to what was expected from calculations, which show the PDOS of Mn 3-d to be much less at 10.5 eV than at 0.5 eV (see Fig. 4.5), much of this intensity at higher binding energy could be due to scattered photoelectrons.

The shaded intensity in the 5.5- and 10.5-eV scans is due to the Mn MVV Auger peak. This additional intensity can be confusing, as it appears that the Fano line shape shifts as the initial states are changed, which will not occur.

Figure 4.8 shows 16 scans of the valence band using increasing photon energies (the scans have been normalized to the Fermi edge to show relative changes in structure and intensity). Each has three features that stand out: A broad feature around 2.75 eV (peak **c**), another feature around 0.9 eV (peak **b**), and a feature at the Fermi edge (peak **a**).

Before looking at the individual peaks, note that with the increase in photon energy there is an almost constant change in intensity between the states below and above about 2 eV binding energy. At BEs greater than 2 eV, the intensity continually increases with respect to the intensity at BEs less than 2 eV (keep in mind that the overall intensity is decreasing due to less photon flux). A consistent change like this over a broad range of photon energies is not characteristic of final-state effects. Much more, it is due to the

**FIG. 4.8** A set of scans at normal emission with changing photon energy  $h\nu$  ( $\Gamma \rightarrow A$  symmetry line). Three features stand out, labeled **a**, **b**, and **c**. Symmetry seen in peaks **a** and **b** indicate the location of the symmetry points  $\Gamma$  and **A** shown to the right of the figure. **A** is shown using BE's of both 0 and 1 eV.



photoionization cross sections. From the cross sections for Mn-3d and Bi-6p subshells listed in Yeh and Lindau [32], the Mn-3d cross section monotonically increases from 10 eV to 40 eV, while the Bi-6p cross section monotonically decreases over the same range. This would explain the change in intensities over such a broad range. It also supports the CIS findings that there is much less Mn-3d character near the Fermi edge, as well as establishes Bi-6p character close to the Fermi edge.

Looking at the 2.75 eV feature (peak c), we can see that it does not disperse, yet it changes shape quite often. The changes in shape can be due to electric-dipole matrix element effects, especially since we are changing the photon energy (the energies are much lower than earlier, so final states are much less free-electron like), as well as the dispersion of individual bands within the feature. The fact that the feature stays localized around 2.75 eV shows that any dispersion is small. This is expected from d-character bands, which dominate this region of the valence band. Looking at the band structure calculations shown in Fig. 4.9, we can see that there are a large number of bands in this area, and, as expected, most of them are relatively flat.

Peak b is narrower and we are able to see that it definitely disperses at low photon energies. The dashed line in the figure traces out the general movement of the peak. The width of the band is about 300 meV. There seems to be some symmetry as it curves towards and away from the Fermi edge at lower energies. Taking the symmetry to indicate the crossing of a Brillouin zone boundary, we calculate the inner potential  $V_0$  (defined on page 20) to be approximately 14 eV. This puts the A symmetry point at about 16 eV photon energy with a binding energy of 1 eV (shown to the right in Fig. 4.8).

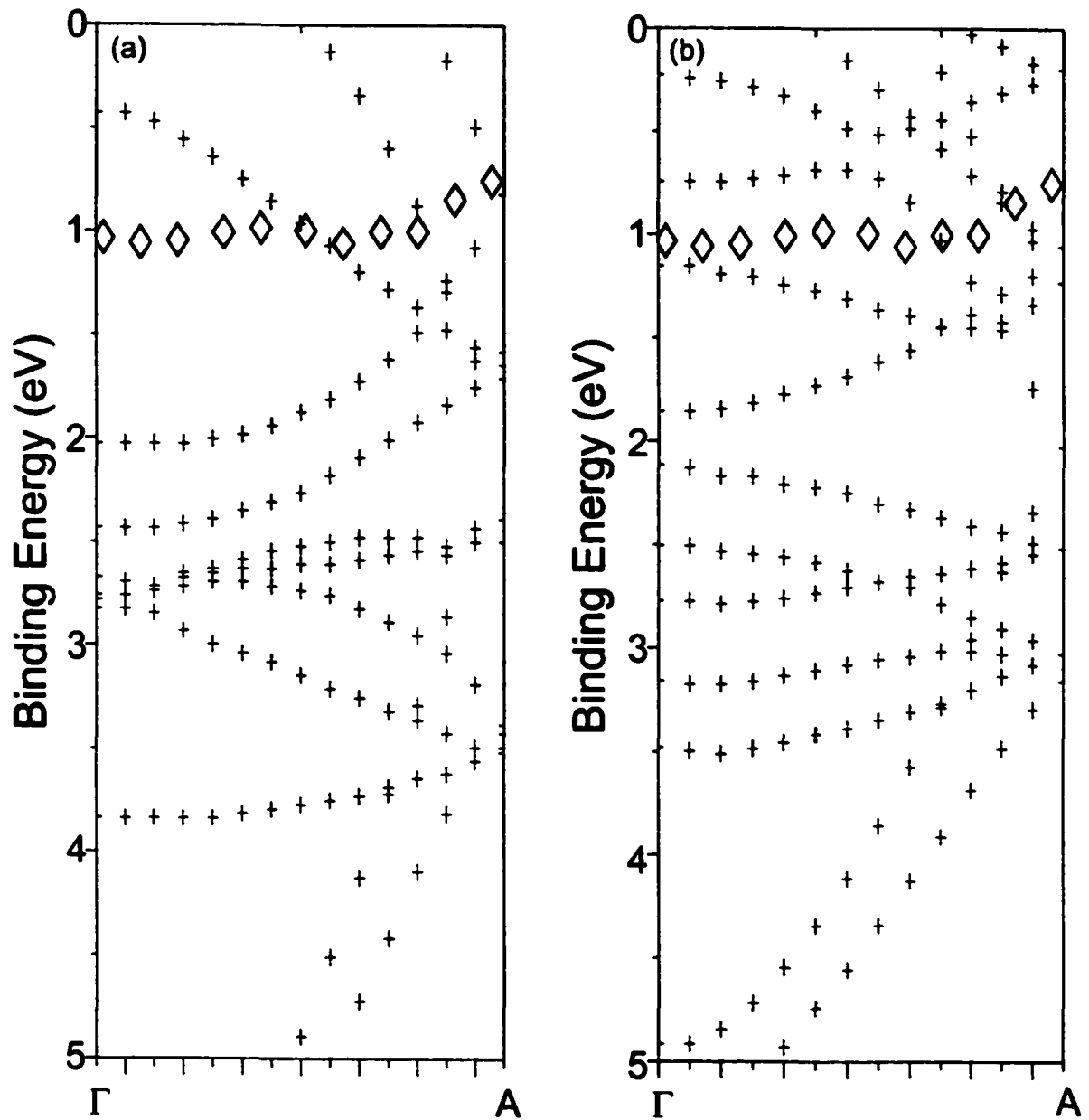
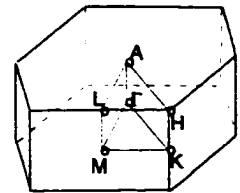


FIG. 4.9 Results of theoretical band structure calculations performed by (a) Ravindran [5] and (b) Köhler [4]. The hollow diamonds indicate the experimental points of peak **b** in figure 4.7.



Peak **b** is most likely due to the Bi-6p bands instead of Mn-3d. For one, as seen in the CIS scans, there is less 3-d character in this range than at greater binding energies. Second, the peak itself continuously loses intensity from low to high photon energy, furthering the case that it indeed has Bi-6p character (due to the cross sections described above). We compare the dispersion of peak **b** with the calculated band structures in Fig. 4.9. The increase in bonding energy appears to be consistent with the calculations of both Ravindran [5] and Köhler [4], while the main intensity around 1 eV is more consistent with Köhler.

Finally, the scans in Fig. 4.8 show a peak very near the Fermi edge. Its intensity and shape change often, possibly signifying Fermi-surface crossings. It is interesting to note that with the inner potential of 14 eV, the symmetry point  $\Gamma$ , for the Fermi energy  $E_F$ , lands approximately between the 26- and 27-eV scans. Here, peak **a** shows symmetry with a possible Fermi-surface crossing shown by the tick marks in the figure. At 26 and 27 eV, feature **a** is peaked right at the Fermi edge, signifying a band starting to cross. At 25 and 28 eV, the feature has moved in from the Fermi edge slightly, and by 24 and 30 eV, the feature has disappeared, losing intensity due to final-state effects or changing its character. Because peak **b** continuously decreases in intensity with respect to peak **a**, we expect peak **a** could be of Mn-3d character. From the calculations [4, 5, 6], the peak appears to be due to the Mn-3d minority states, most of which lie above the Fermi energy.

We now look at the Bi-5d core levels in Fig. 4.10. The  ${}^2D_{5/2}$  and  ${}^2D_{3/2}$  peaks are located at binding energies of 23.60 eV and 26.65 eV respectively. The  ${}^2D_{5/2}$  peak is

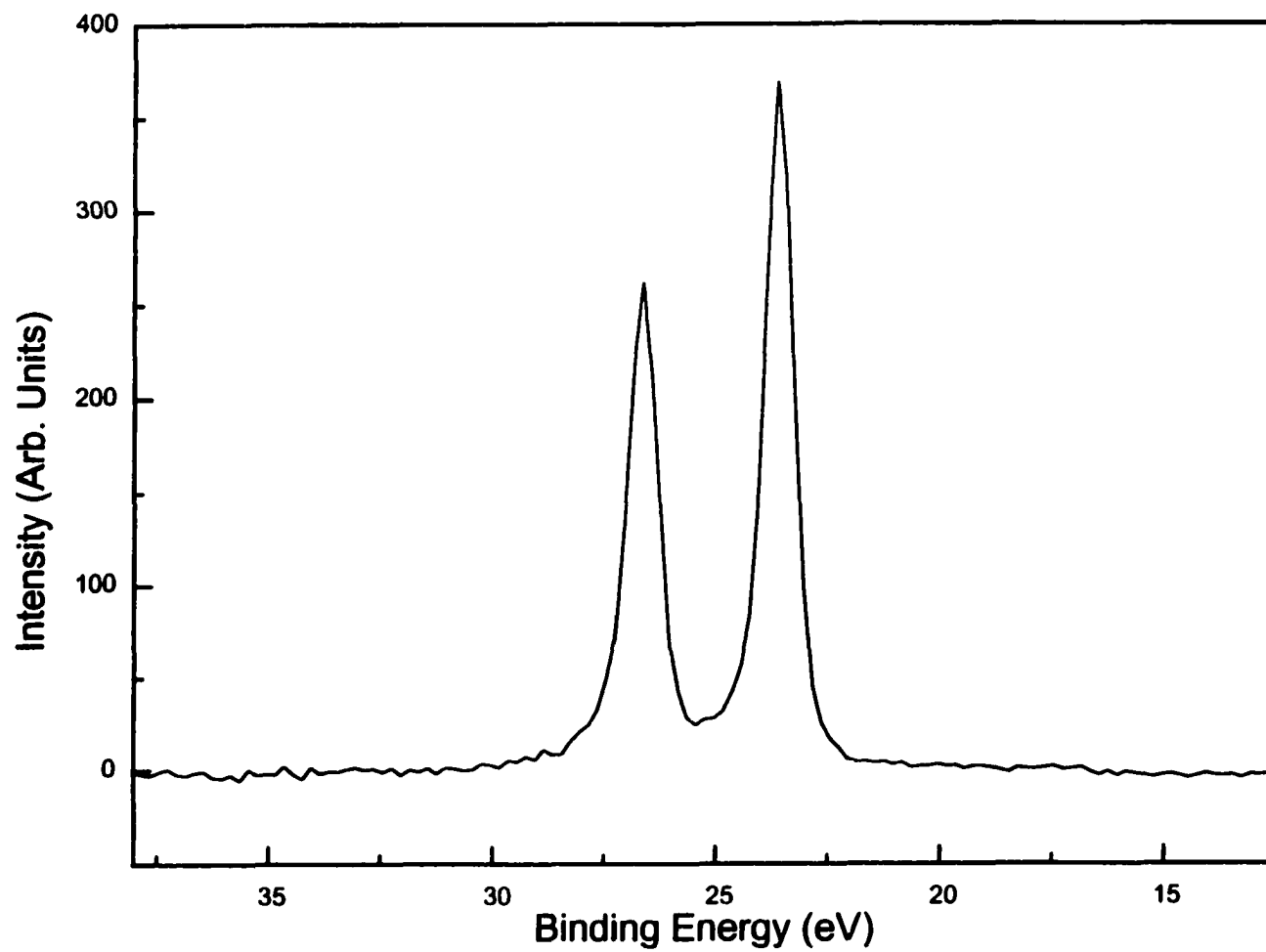
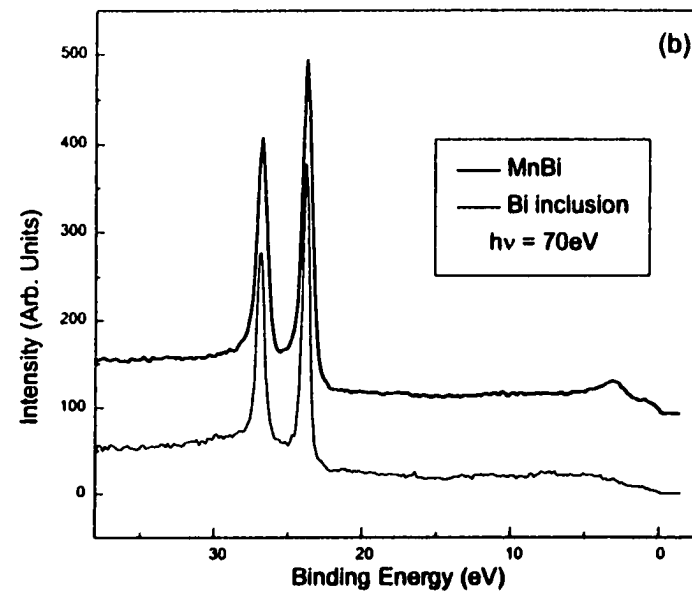
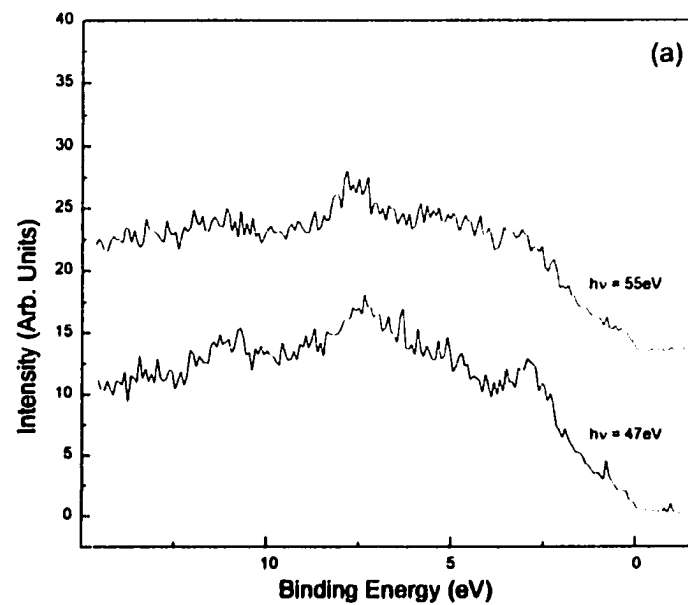


FIG. 4.10 Photoemission scan of the Bi-5d core levels using a photon energy of  $h\nu = 70\text{eV}$

approximately  $3/2$  times larger than the  ${}^2D_{3/2}$  peak, in agreement with the degeneracies of the emitting orbitals  $(2J_1 + 1)/(2J_2 + 1) = 3/2$ . The peaks were fitted with Lorentzian curves using the least-squares method. The FWHM of the peaks were 0.665 eV for the  ${}^2D_{5/2}$  peak and 0.726 eV for the  ${}^2D_{3/2}$  peak. The resolution of the measurement, measured from Fermi edge, was 0.383 eV. Even using the bare eye, one can see the symmetric shapes of the peaks. The symmetric peaks, and the fact that we don't see any satellites, indicate weakly correlated electrons [33]. We expect, then, that the one-electron approximation can be used here. The symmetric peaks also indicate a lack of Bi character at the Fermi level, reinforcing the view that the feature there is due to Mn-3d states.

We now address the crystalline Bi inclusions that occurred within the MnBi crystals. Several of the samples, instead of cleaving in the bulk MnBi crystals, cleaved along sites of single-crystal Bi. Initially, this caused confusion. Once discovered, however, the inclusions were easily detected. Upon cleaving, the samples that cleaved along an inclusion would show a dull surface instead of a shiny surface. Spectra from these surfaces showed a great deal of dispersion with angle as well as photon energy, showing that they were indeed from a single crystal. The inclusion spectra resembled, very well, angular resolved photoemission spectra of single crystal Bi [34]. When using resonant photoemission, Mn character was completely undetectable, while the Bi core levels remained strong. Figure 4.11a shows valence-band scans taken of a Bi impurity at photon energies below and above the Mn  $3p \rightarrow 3d$  threshold. Note the total lack of enhancement of the 55-eV peak, signifying lack of Mn. Were the surface of MnBi, we



**FIG. 4.11 (a) Resonant photoemission showing a lack of Mn signal in a Bi inclusion. With the MnBi sample, a large enhancement would be seen as the photon energy passed the Mn 3p-3d threshold ( $h\nu \sim 47\text{eV}$ ).**

**(b) Photoemission of a good MnBi cleave and a cleave with a Bi inclusion. Both scans were taken above the Mn 3p-3d threshold.**

would have seen a large increase in intensity as in Fig. 4.6. Figure 4.11b shows two scans taken at a photon energy of 70 eV. One scan is of a good cleave of MnBi and the other is of a cleave along a Bi inclusion. We can see in both situations the Bi cores are strong, yet in the Bi inclusion scan, the valence band intensity has diminished greatly.

It appears, then, that since the crystals were grown in a Bi flux, small single crystals of Bi were occasionally included in the MnBi single crystals. Data were only taken on a crystal if the whole surface showed no Bi inclusion character. We are confident that all the above data are from single crystal MnBi surfaces. Laue diffraction patterns were taken of the samples after finishing the measurements to affirm that the crystal orientation had not changed. As a note, future ARPES experiments may be successful on a polished sample, if, when subsequently sputtered and annealed in UHV, it produces a clean surface of correct stoichiometry.

### **Photoemission Study of $\text{GdNi}_2\text{Ge}_2$**

In this experiment, we examine the valence band of  $\text{GdNi}_2\text{Ge}_2$  with ARPES, using synchrotron radiation. We also examine the shallow core levels with AIPES using synchrotron radiation as the radiation source. We attempt to identify the Gd-4f electrons and justify their treatment in the calculations as core levels. Lastly, we take high-resolution scans of the Fermi edge to find evidence of the SDW and Fermi-surface nesting that was reported.

The crystal structure of  $\text{GdNi}_2\text{Ge}_2$  is the body-centered tetragonal (BCT)  $\text{ThCr}_2\text{Si}_2$

structure (see Fig. 4.12). For  $\text{GdNi}_2\text{Ge}_2$ , the room temperature lattice constants are:  $c = 9.783 \text{ \AA}$ , and  $a = 4.063 \text{ \AA}$  [35]. High-quality single crystals were provided by Dr. Paul Canfield of the Ames Laboratory (DOE). These crystals were grown using a high-temperature-solution-growth technique detailed by Canfield and Fisk [36].

Before mounting the crystals in the vacuum chamber, Laue diffraction patterns were taken to determine their orientation. Figure 4.13 shows the Laue diffraction pattern of  $\text{GdNi}_2\text{Ge}_2$ , revealing that the  $[001]$  direction (c-axis) is the surface normal. The  $\langle 100 \rangle$  directions can be distinguished from the  $\langle 110 \rangle$  directions by the former's greater number of spots. Figure 4.14 shows the first Brillouin zone for the BCT structure with labeled symmetry points.

The experiment was prepared and performed in the same manner as with the MnBi samples. Temperature was adjusted via a small resistor imbedded in the cold finger. Unless otherwise noted, the temperature at which the following scans were taken was kept at 37 K. At this temperature, the sample is paramagnetic and above the SDW transition.

Figures 4.15 and 4.16 show angle-resolved photoemission scans of the valence band at different photon energies along the  $[110]$  and  $[100]$  directions (in the  $\Gamma\text{XUZ}$  and  $\Gamma\Sigma\text{NZ}$  planes), respectively. The figures show at which angle the scans cross the BZ boundary for  $BE = 0 \text{ eV}$ . Figure 4.17 shows ARPES scans in the  $[001]$  direction ( $\Gamma$  to Z), normal to the surface. Many peaks can be seen to come and go in the scans. This is a result of the myriad of bands that exist, as evidenced by the calculated band structure (see Fig. 4.18), making it next to impossible to identify individual bands. However there are a

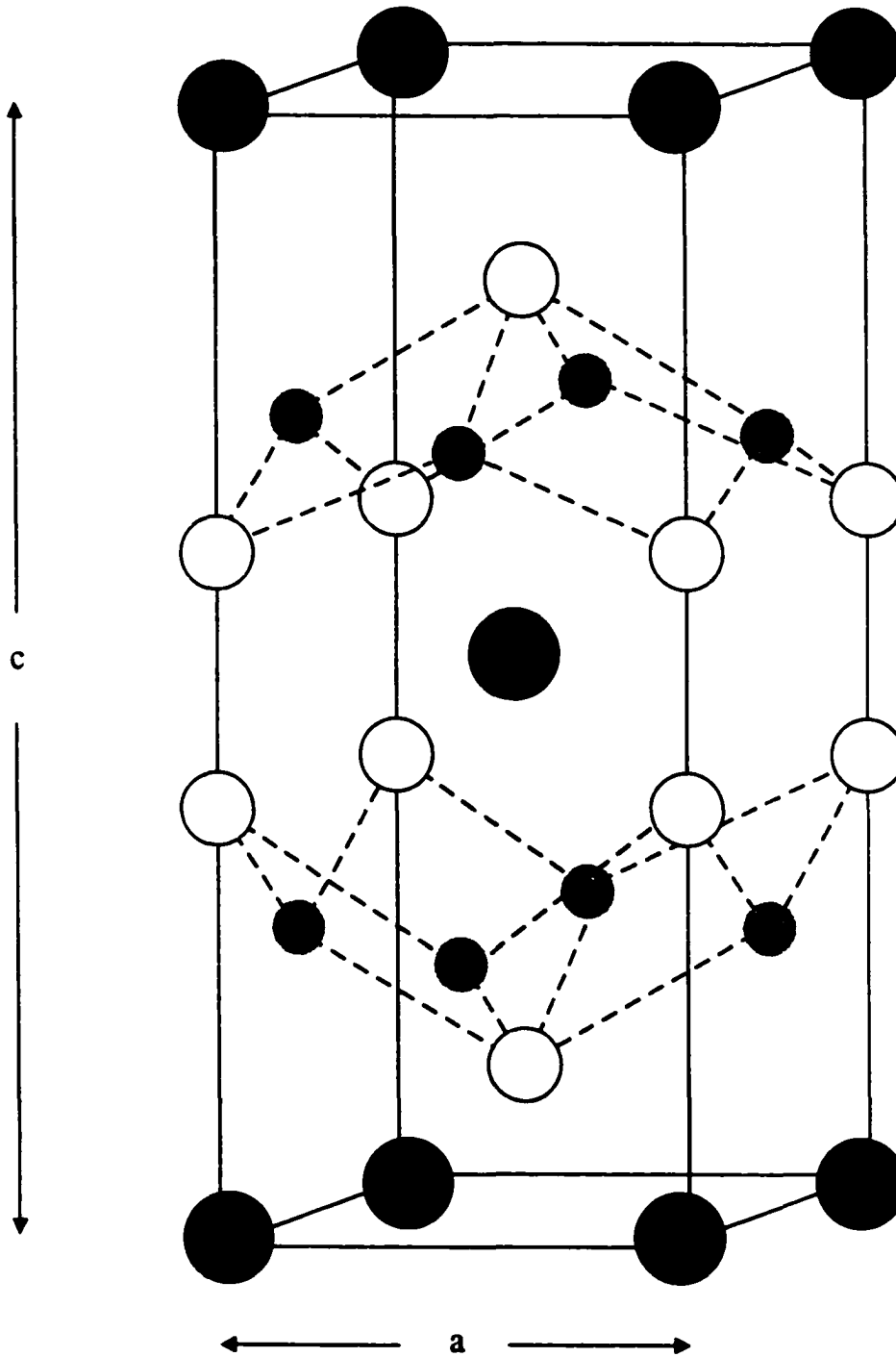


FIG. 4.12 A conventional unit cell of a  $\text{GdNi}_2\text{Ge}_2$  crystal. The large black circles denote Gd atoms, the small shaded circles represent Ni atoms, and the white circles represent Ge atoms.

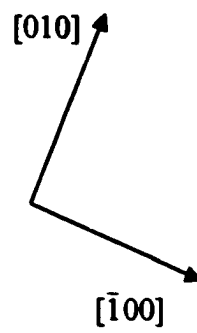
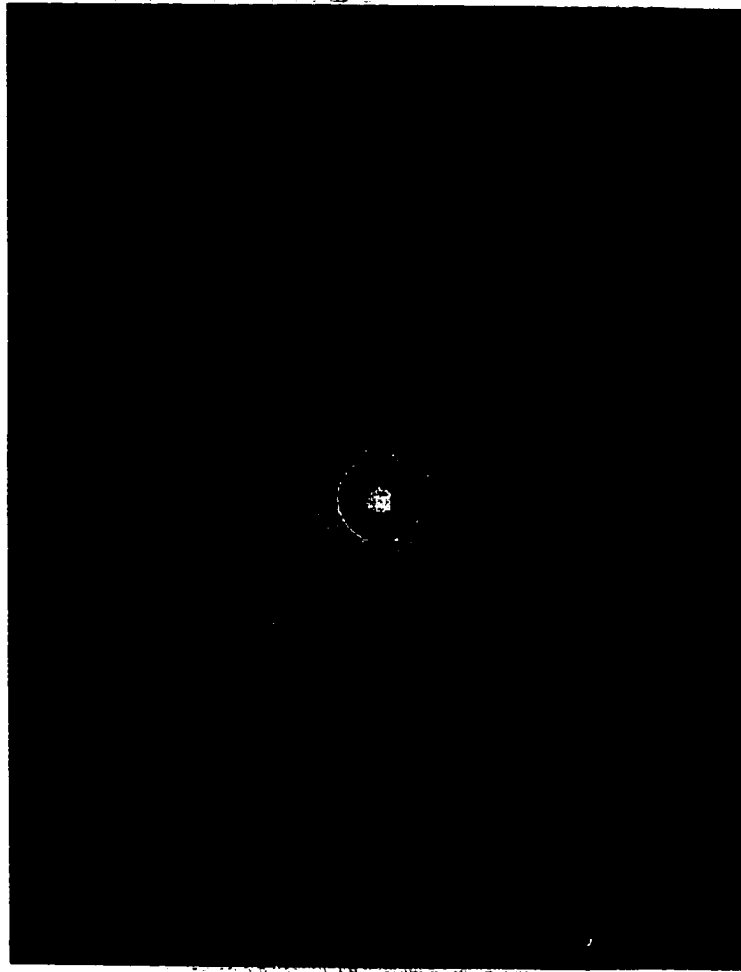


FIG. 4.13 Laue diffraction pattern of  $\text{GdNi}_2\text{Ge}_2$  along the  $[001]$  direction.

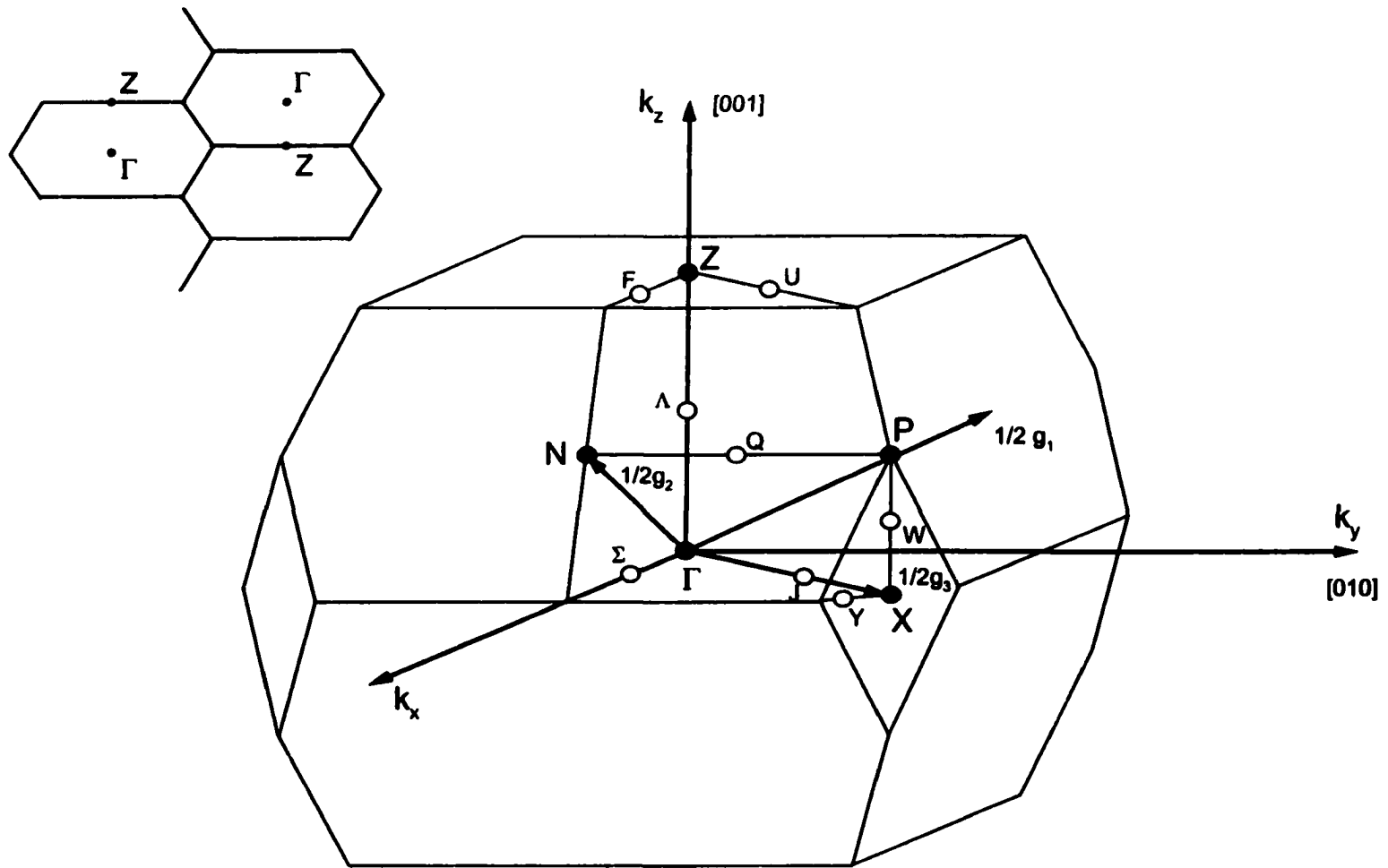


FIG. 4.14 Brillouin zone for a body-centered tetragonal (BCT) lattice with labeled symmetry points. The upper left figure illustrates how the unit cells stack in the  $(k_z, k_y)$  plane.

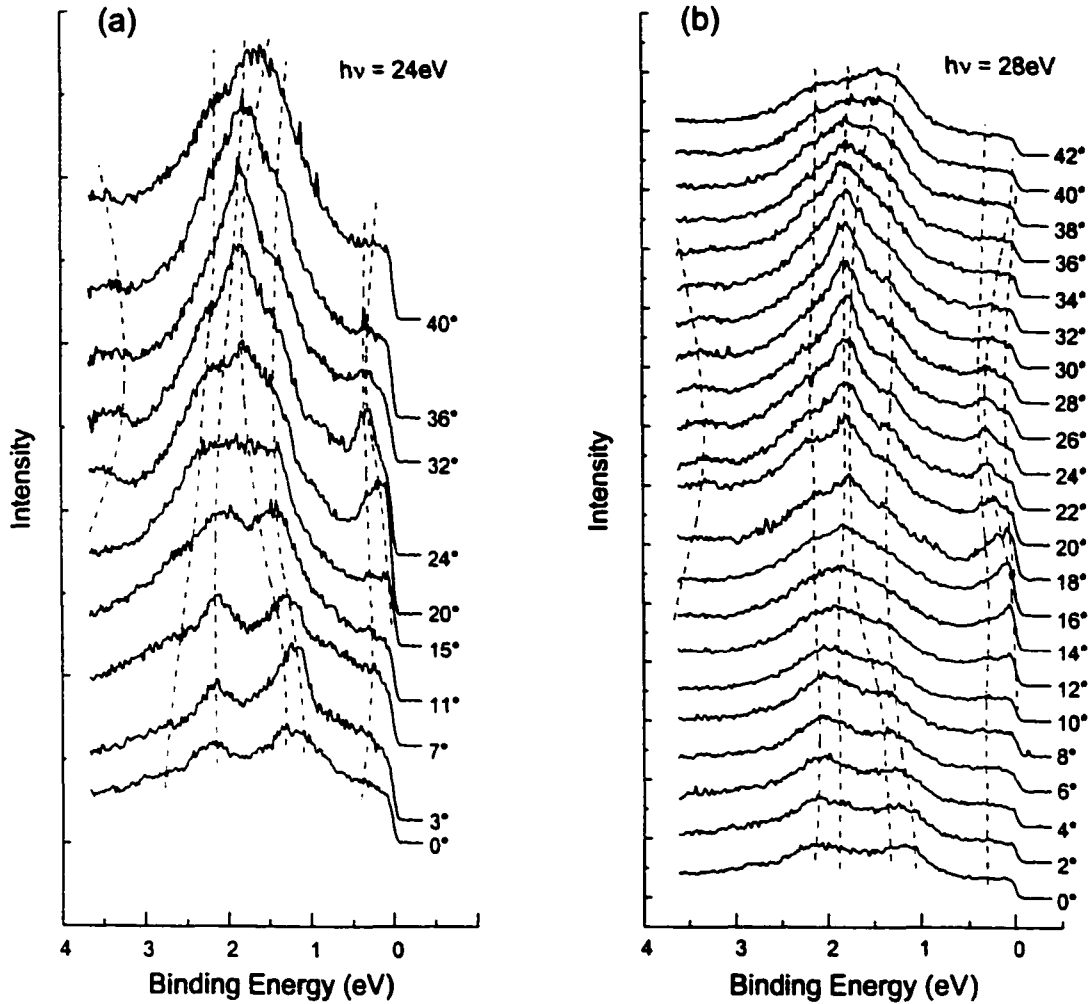


FIG. 4.15 EDCs taken with photon energies of a) 24 eV, and b) 28 eV from a (001) surface while changing angle in the [110] direction (in the  $\Gamma$ XUZ plane). Zero degrees is normal to the surface. The dashed lines qualitatively follow the major features of the scans. The angles of the Brillouin zone boundary are approximately  $29^\circ$  for  $h\nu = 24\text{eV}$  and  $26^\circ$  for  $h\nu = 28\text{eV}$ .

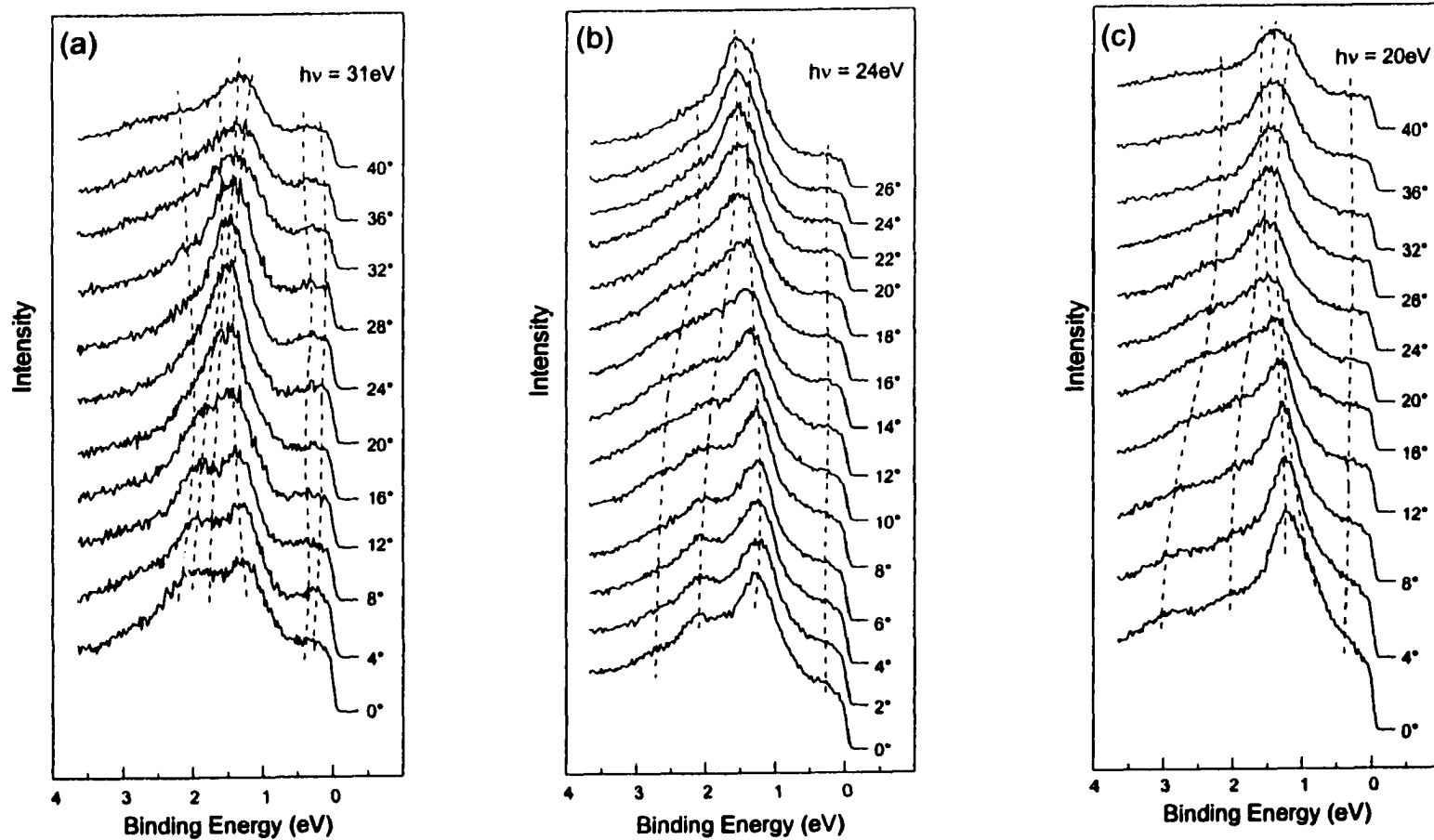


FIG. 4.16 EDCs taken with photon energies of a) 31 eV, b) 24 eV, and c) 20 eV from a (001) surface while changing angle in the [010] direction (in the  $\Gamma\Sigma\text{NZ}$  plane). Zero degrees is normal to the surface. The dashed lines qualitatively follow the major features of the scans. The angles of the Brillouin zone boundary are  $20^\circ$  for  $h\nu = 31\text{ eV}$ ,  $24^\circ$  for  $h\nu = 24\text{ eV}$  and  $26^\circ$  for  $h\nu = 20\text{ eV}$ .

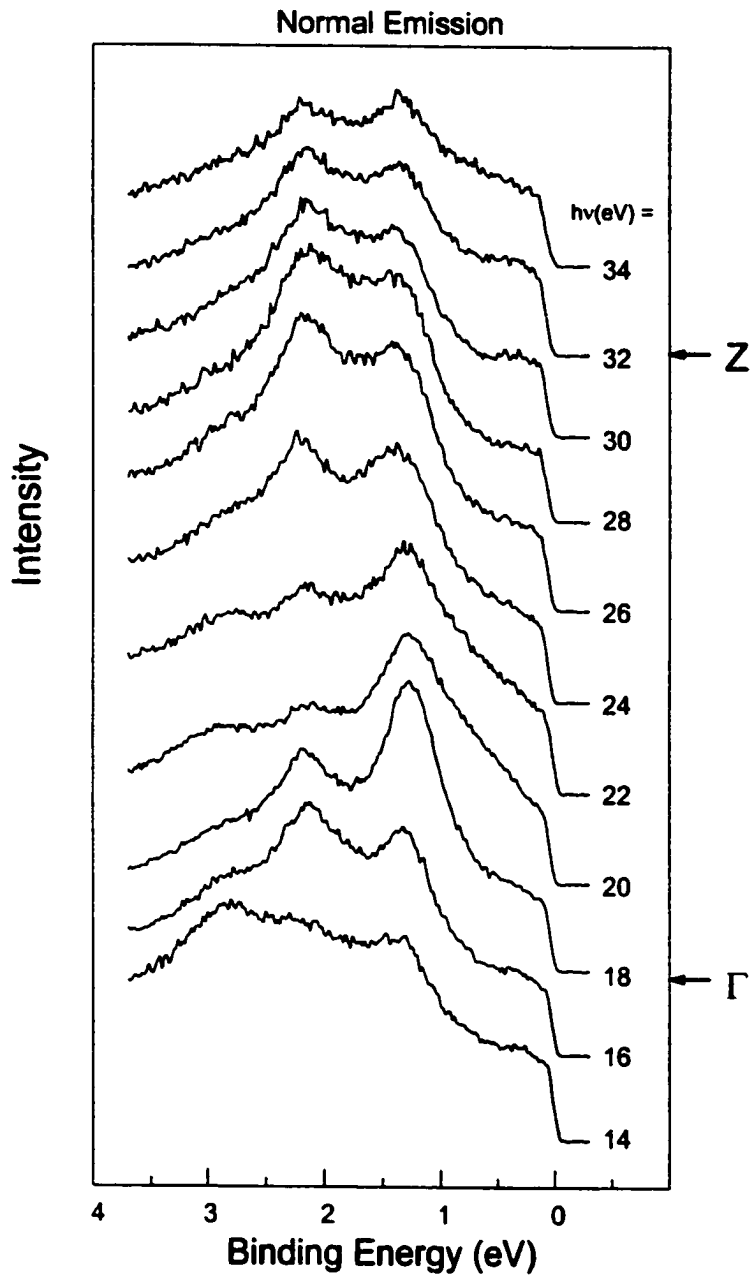
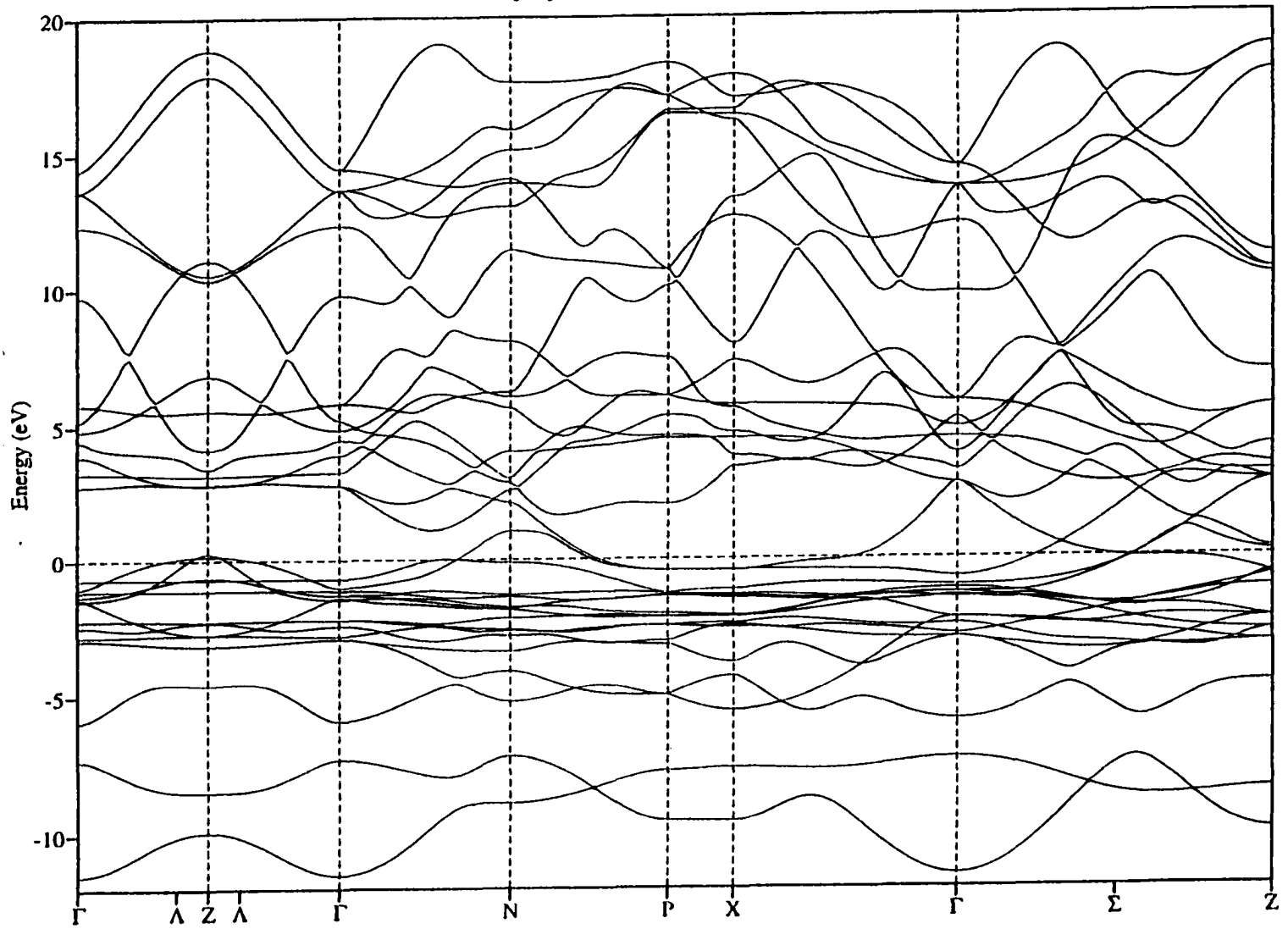


FIG. 4.17 EDCs at normal emission from the (001) surface ( $\Gamma$  -  $Z$  direction) taken with increasing photon energy. Although several features are present, we see no dispersion. This is most likely due to weak binding in the [001] direction.

**FIG. 4.18** Band structure of  $\text{GdNi}_2\text{Ge}_2$  shown along selected high symmetry lines (see Fig. 4.14 for details). The band structure is the result of a tight-binding linear-muffin-tin-orbital calculation using the atomic-sphere approximation [37].

GdNi<sub>2</sub>Ge<sub>2</sub> LDA-TB-LMTO-ASA Bands 01-01-99



few strong features that stand out amidst the background intensity that allow us to follow the general structure of the bands. Dashed lines following the path of the features are included to help guide the eye, and are not meant to specify peak positions quantitatively.

Examining Figs. 4.15, 16 and 17, one can see that the region of greatest intensity occurs between  $\sim 0.7$ - $0.8$  eV and  $\sim 2.5$  eV below the Fermi level. This is consistent with Fig. 4.18, where the greatest density of bands occurs in this same region. Note also the consistency in the width of the bands. Both calculation and experiment (Figs. 4.15 and 16 only) show typical dispersions to range from  $\sim 0.15$  eV to  $\sim 0.9$  eV. This is to be expected as well, as d-bands typically do not disperse much. We do note, however, the almost complete lack of dispersion in the direction normal to the surface (Fig. 4.17). And, though there is no dispersion, there is a great deal of intensity change. This could be attributed to a one-dimensional density-of-states (1DDOS) effect, where the very small escape depth of the electrons causes a lack of the  $k_{\perp}$  selection rule. This then smears out the final states giving us contributions from the whole Brillouin zone in the  $k_{\perp}$  direction at a certain  $k_{\parallel}$ . It may, however, just be a result of weaker bonding in the normal direction, which would be consistent with the cleavage plane being along the c axis. Later results suggest the latter to be the case.

The region with BE larger than  $\sim 2.5$  eV is relatively featureless. Due to this, scans shown are limited to a width of 4 eV. The scans in Fig. 4.15, however, do show a feature that comes in to 3.2 eV at  $16^{\circ}$  and is gone by  $36^{\circ}$  in both frames. Figure 4.18 shows several bands in the region where the BE is greater than 2.5 eV, though they are much more diffuse than those above. This causes a difficulty in resolving any features at

all, and for this reason, as well as time constraints, most of our valence band scans were no more than 4 eV wide.

The final region ( $\sim 0.8$  eV to 0 eV) shows a nearly constant intensity in Figs. 4.16 and 17, though Fig. 4.15 shows quite a prominent Fermi-surface crossing. This crossing is also accompanied by one of lesser intensity (as shown by the dotted lines). At first glance, it seems to form an electron pocket. Looking at the band calculation in Fig. 4.18, there are indeed several Fermi-edge crossings, one of which is in the  $[110]$  direction ( $\Gamma$  to X). It is surprising, however, that only crossings in this area of the Brillouin zone were detected. In Fig. 4.18, one can see several Fermi-edge crossings in different directions, including the  $[100]$  ( $\Gamma - \Sigma - Z$ ) and  $[001]$  ( $\Gamma - \Lambda - Z$ ). As seen in Figs. 4.16 and 17, however, no obvious crossings can be detected in these directions experimentally, although in Fig. 4.16(a), which is the closest approximation to the  $\Gamma - \Sigma - Z$  line, we see slightly more intensity changes around the Fermi-level region than in either (b), (c) or Fig. 4.17.

The Fermi-edge crossing in Fig. 4.15 is strong enough that we were able to map it through k-space and use its symmetry to locate the Brillouin zone boundaries in the  $[001]$  direction (c-direction). Thus, we were able to find the inner potential to be  $V_0 \approx 13.5$  eV and locate the  $\Gamma$  and Z symmetry points as shown in Fig. 4.17. Figure 4.19 shows the location of the Fermi-edge crossing at different points mapped onto the  $\Gamma$ XPZ plane using the periodic zone scheme. One can see how it effectively maps the Fermi surface in this plane. The curved line through the data points was created via a least squares fit using an empirical  $(\sin^2 + \sin^6)$  expression. We see then, that the Fermi surface forms an

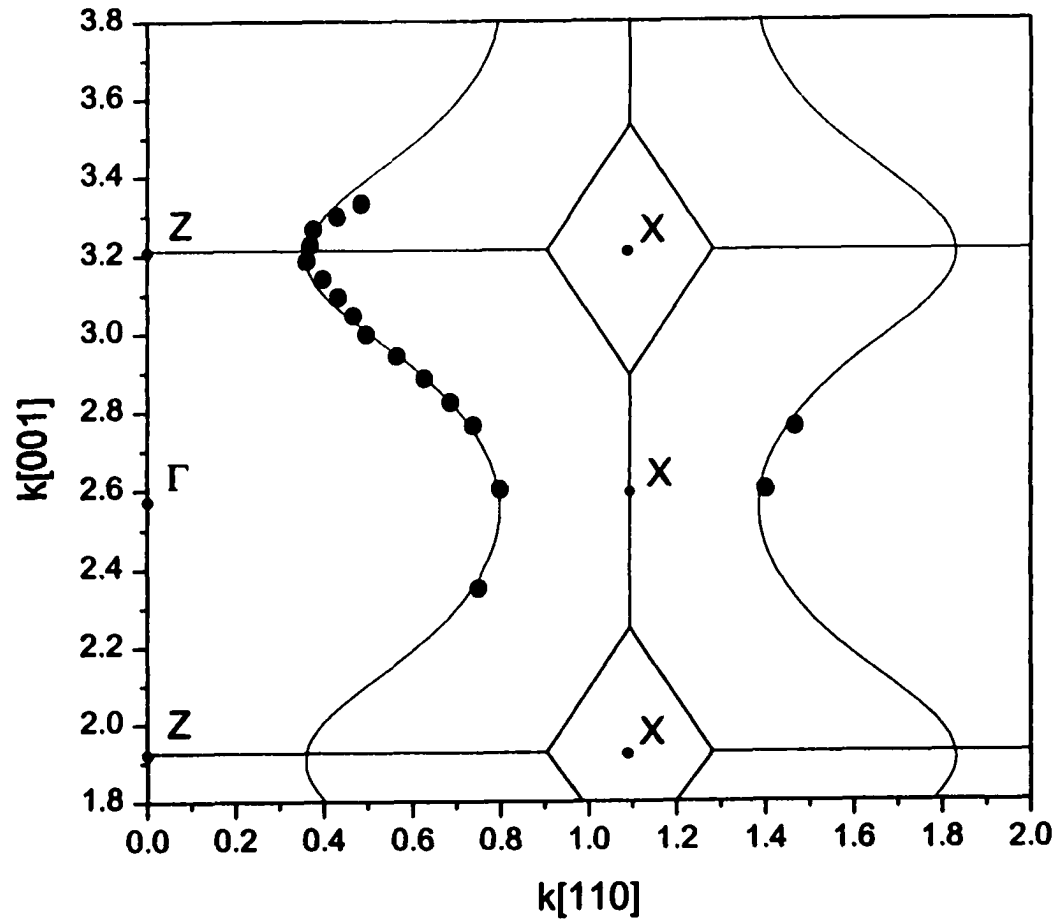


FIG. 4.19 Fermi Surface mapped in the  $\Gamma$ XPZ plane using a periodic zone scheme. Black dots indicate the experimental data, while the curve is a least-squares fit using a  $(\sin^2 + \sin^6)$  expression.

electron pocket in the (001) plane (a-b plane), but an open orbit along the c axis. The fact that we can see a very large curvature in the Fermi-surface in the [001] direction using photoemission reinforces the position that the lack of dispersion of peaks in this direction is not due to 1DDOS effects, and that we should not use the 1DDOS to analyze these data.

If we compare this experimental section of the Fermi surface with the theoretical Fermi surface, we see a striking difference (see Fig. 4.20). While both surfaces have similar oscillating patterns through the BZ (a broad peak at the maximum  $k[110]$  value and a narrow peak at the minimum  $k[110]$  value), the patterns are offset by half a BZ. The theoretical Fermi surface has its minimum  $k[110]$  value ( $0.48 \text{ \AA}^{-1}$ ) at  $k[001] = \Gamma$  and its maximum  $k[110]$  value ( $0.79 \text{ \AA}^{-1}$ ) at  $k[001] = Z$ . The experimental  $k[110]$ 's are just the opposite, with the minimum at  $k[001] = Z$  and maximum at  $k[001] = \Gamma$  (min. and max. experimental values are  $0.38 \text{ \AA}^{-1}$  and  $0.80 \text{ \AA}^{-1}$  respectively). One should also note the close correspondence of the theoretical and experimental  $k$  values.

Due to the general shape of the Fermi surfaces being so similar (except for the half-BZ shift), we considered human error being a possible cause of this discrepancy. In order to discount human error, our data points and their locations in the BZ were checked several times. Our calculations of the reciprocal lattice for the BCT lattice were also checked.

It would be possible to match the experimental and theoretical curves by using an inner potential other than 13.5 eV. However, the closest inner potentials possible would be 2.5 eV and 28 eV, both of which would be absurd, as inner potentials typically range

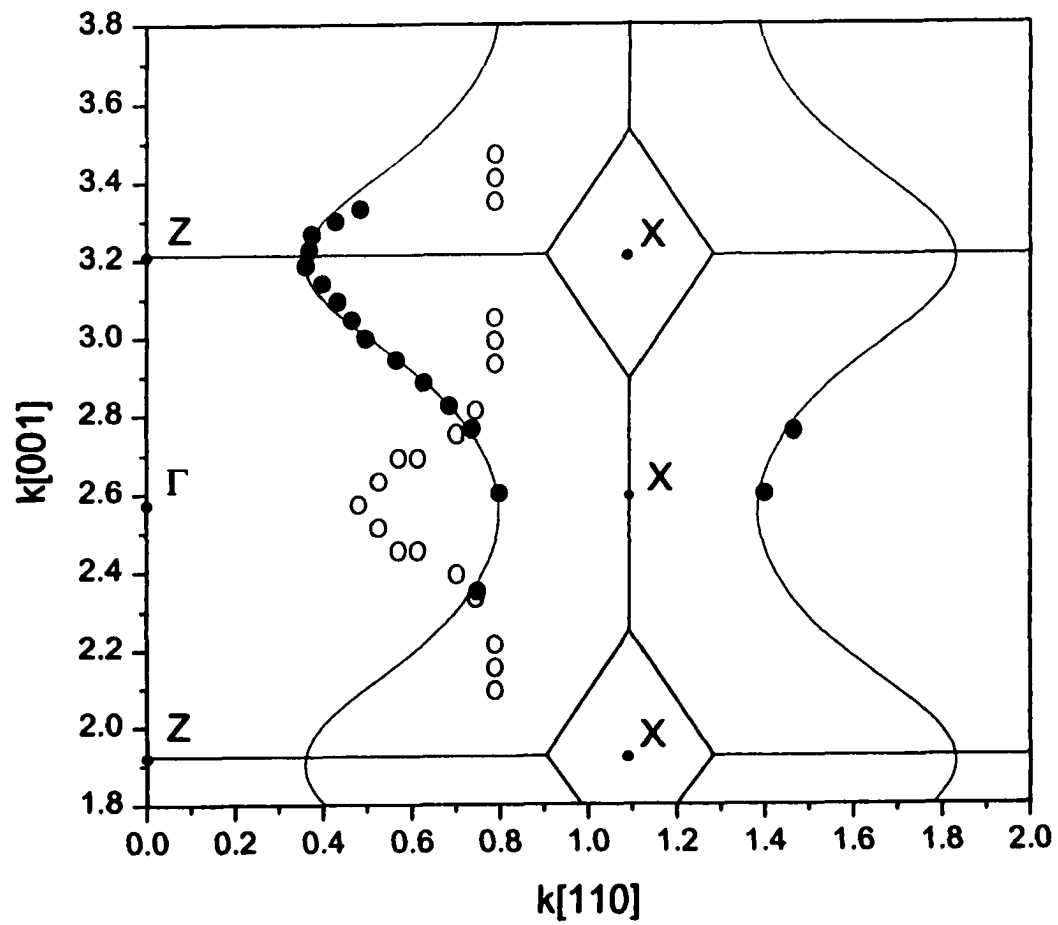


Fig. 4.20 Fermi Surface mapped in the  $\Gamma$ XPZ plane using a periodic zone scheme. Black circles indicate the experimental data. Hollow circles indicate the theoretical Fermi surface.

between 10 and 14 eV. Other explanations, such as a change of the lattice constant due to residual magnetization, would only change the scale of the Fermi surface and not actually shift it. This, of course, rules out looking for typical factor-of-2 errors that commonly occur. In discussions with the person who performed the theoretical calculations, Z. Islam [37], we were unable to find any reason for the discrepancy. As it stands, this issue is unresolved, though we believe the experimental data to be correct.

It is interesting to look again at how, in the normal emission spectra, even though there is no visible dispersion, there is a great deal of intensity change, especially in the two peaks at BE = 1.25 and 2.20 eV. If we continue to change the photon energy, a pattern emerges. The intensities of the peaks alternate between the peak at BE = 1.25 eV being dominant in intensity, and the two peaks having approximately the same intensity (see Fig. 4.21). Using the Brillouin zone lattice constant  $k_c = 1.285 \text{ \AA}^{-1}$  and the inner potential of  $V_o = 13.5 \text{ eV}$ , the photon energies needed to obtain spectra of the alternating  $\Gamma$  and Z points can be calculated using this equation similar to (2.9):

$$E_{kin} = \left( \frac{\hbar^2}{2m} \right) (\mathbf{k}_r + \mathbf{G})^2 - V_o, \quad (4.1)$$

where, after equation (2.2),

$$E_{kin} = \hbar\omega - \Phi - |E_B| \quad (4.2)$$

(Here,  $\Phi = \text{work function} \approx 4.3 \text{ eV}$  and  $E_B = \text{BE} \approx 1.5 \text{ eV}$ ). The results have the  $\Gamma$  points located at  $h\nu = 17.5, 49.0, 93.0, \text{ and } 149.7 \text{ eV}$ , and the Z points at  $h\nu = 32.7, 69.5, \text{ and } 119.8 \text{ eV}$ . These energies have been marked on figure 4.20 and one can see how well they match the change in intensities, with the  $\Gamma$  point associated with the dominant

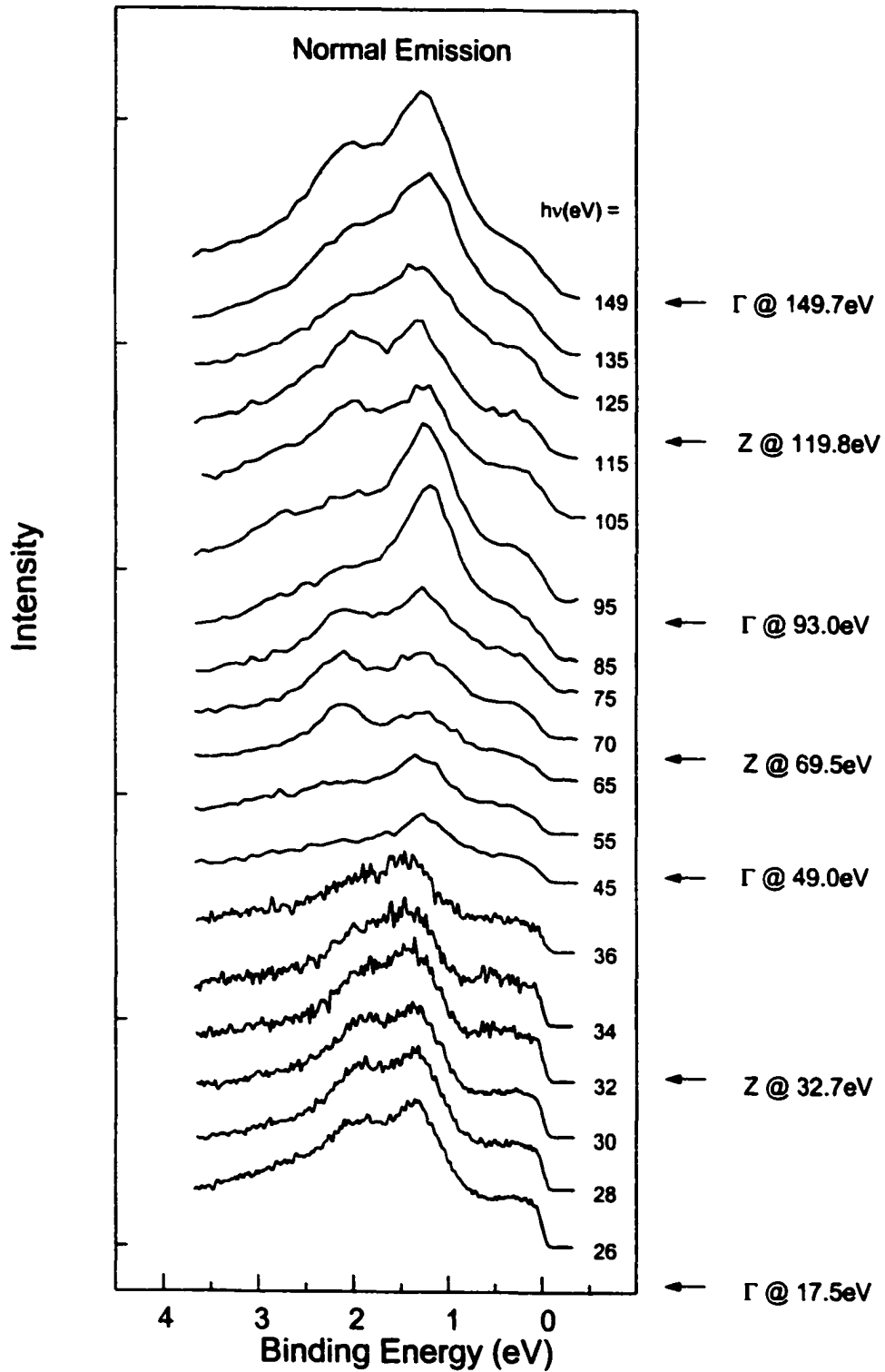


FIG. 4.21 EDCs taken at normal emission over a large range of photon energies. The high-symmetry points  $\Gamma$  and Z are indicated to the right of the figure.

1.25 eV BE peak, and the Z point associated with both peaks having comparative intensities. This change in intensity is most likely due to dispersing bands that are not resolved. With the extended range of photon energies, we are even able to see that the features themselves do disperse slightly. If we refer to the  $\Gamma$ - $\Lambda$ -Z direction in the band structure (Fig. 4.18), we see that there is a group of bands at approximately 1.25 and another at approximately 2.2 eV BE. At the  $\Gamma$  point there are more bands in the 1.25 eV group, which can be assumed to result in the larger intensity peak. But as we scan to the Z point individual bands disperse out of this group, one even dispersing to the 2.2 eV group, making the intensity of the two peaks comparable. Note that this agreement between the theoretical and experimental  $\Gamma$  and Z points is contrary to the disagreement shown in the Fermi surface comparison. Presently, we cannot explain this.

According to the calculation, the valence band is mostly of Ni 3d character. We expect, then, to be able to see resonant behavior between the nickel 3p levels and the valence band. Figure 4.22 shows 10-eV wide scans of the valence band with the photon energies varying through the Ni 3p $\rightarrow$ 3d core-absorption threshold ( $h\nu \sim 66$  eV). The scans show the full valence band as well as the Gd-4f levels at  $\sim 8$  eV BE. We expect to see a resonant enhancement of the Ni-d satellite which is located about 6 eV below the Ni-d bands [38]. Figure 4.22 shows no such resonance. We can see a slight enhancement around 5 eV BE due to the MVV Auger peak in the  $h\nu = 67$  eV scan. The vertical lines show the expected location of the Auger peak.

To be more thorough, CIS scans were taken at various energies throughout the valence band and the expected Ni-satellite location (Fig. 4.23). The results are

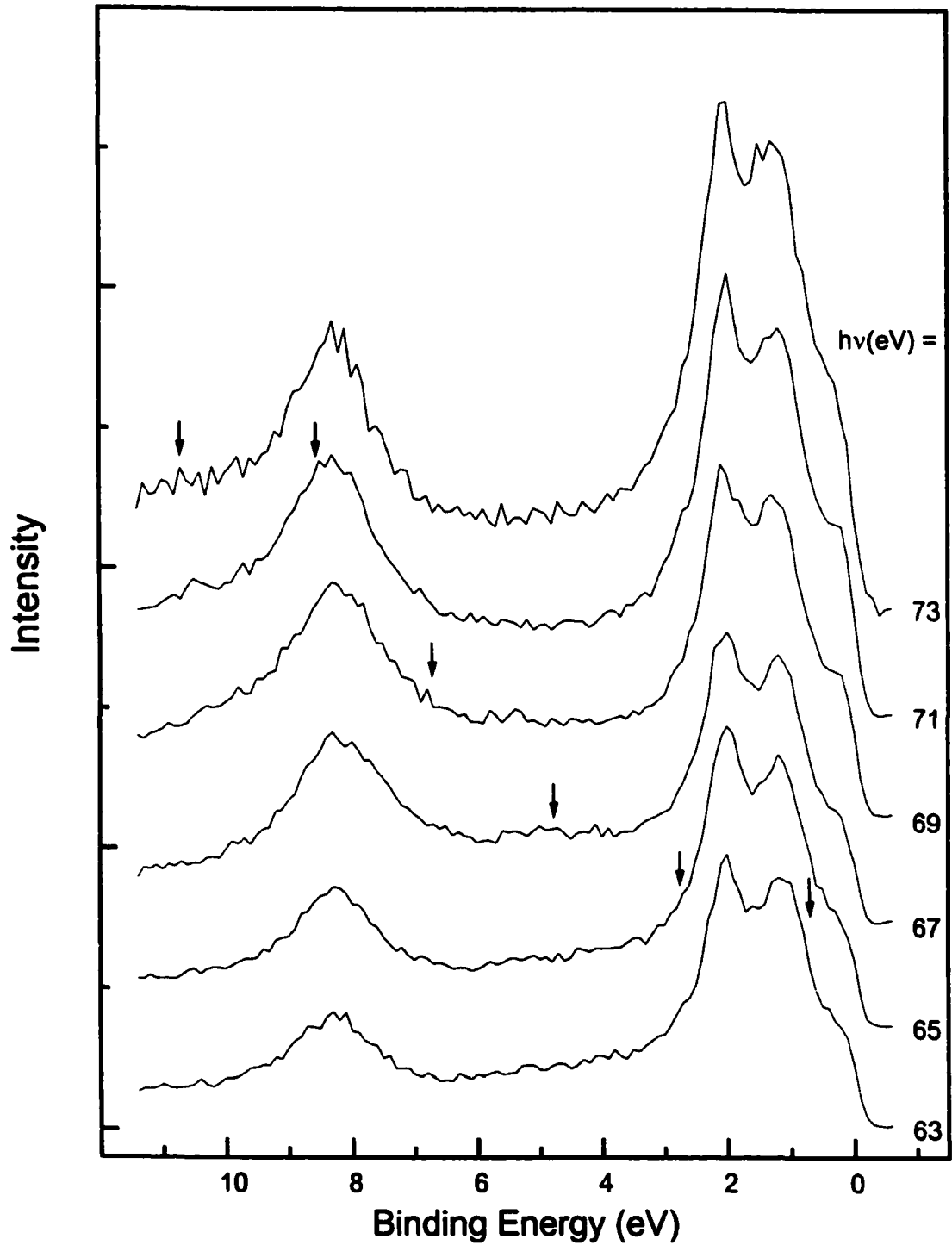


FIG. 4.22 EDCs taken at varying photon energies in an attempt to observe resonance of the Ni-3d satellite. The Ni 3p-3d core-absorption threshold is  $\sim 66\text{eV}$ . Arrows indicate the expected location of the MVV Auger peak.

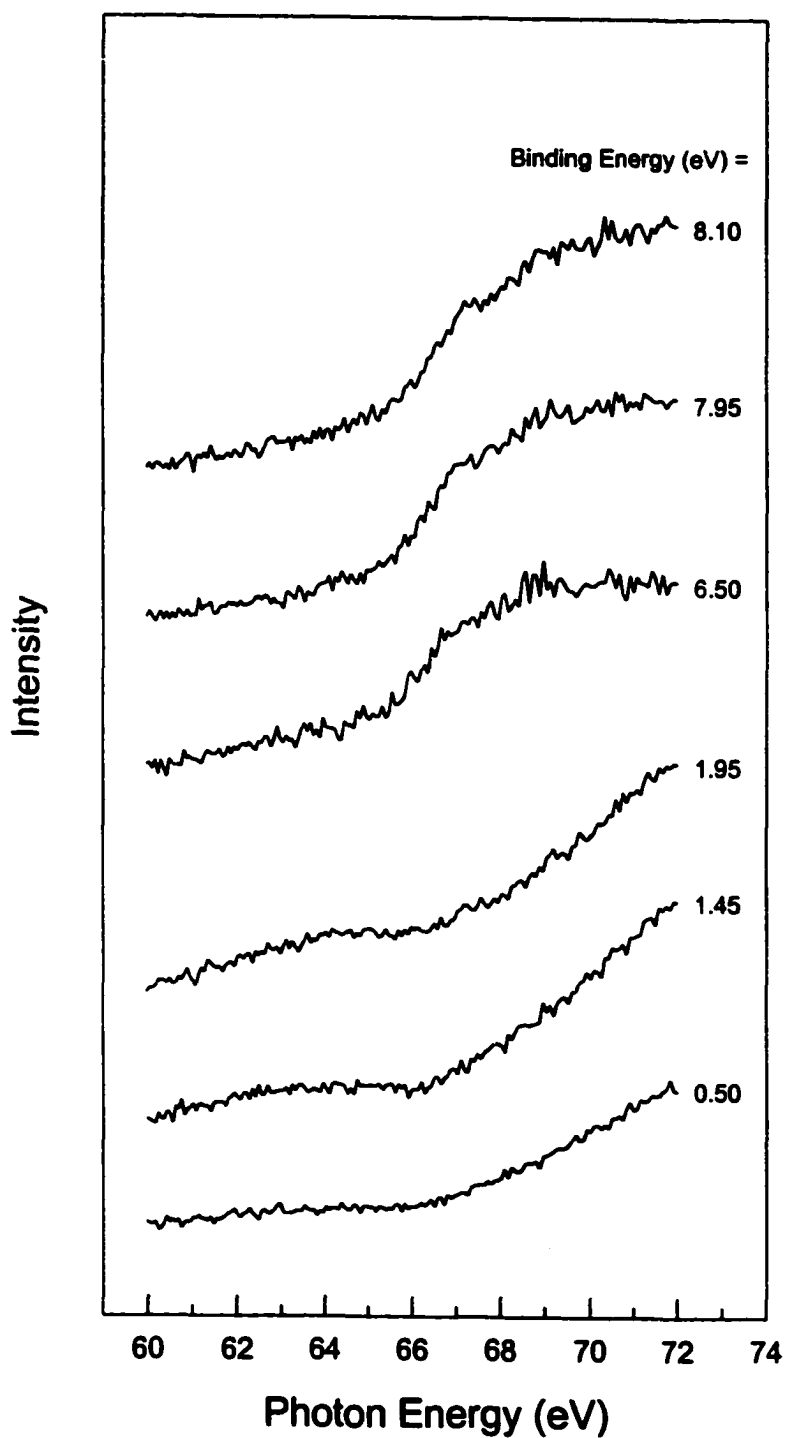


FIG. 4.23 Constant initial energy (CIS) scans taken at different binding energies throughout the valence band and the expected location of the 6eV Ni-d satellite.

characteristic of strong Ni character. The scans at 0.50, 1.45, and 1.95 eV show the expected line shape of the anti-resonance (specifically, the change in slope) that should occur in the Ni-character bands (due to the reduction of the number of photons available for direct photoemission [39] ), while the scans at 6.50, 7.95, and 8.10 eV show the expected line shape of the resonance of the Ni-3d satellite (The Fano line shape may be obtained by subtracting a background from each scan) [40]. We thus conclude that although an enhancement of the EDCs is not large, there is apparent strong Ni-d character throughout the valence band.

We now switch our attention to the shallow core levels. Figure 4.24 shows a 40-eV wide energy scan both off (12a) and on (12b) resonance for the Gd-4f levels. The scans were taken with photon energies of a) 135 eV, and b) 149 eV, with the Gd 4d→4f core-absorption threshold at  $h\nu \sim 142.6$  eV. We can immediately notice the strong enhancement of the Gd 4f peak at a binding energy of 8.25 eV. The peak is a Lorentzian with a FWHM of 1.42 eV. One can see that the peak is isolated from the valence band, and the valence band itself is unaffected by the resonance. To further investigate whether there is any Gd 4f character in the valence band we took CIS scans of both the Gd-4f peak and the valence band (see Fig. 4.25). The very large resonance seen at 8.2 eV BE and the absence of resonance at 1.7 and 0.3 eV BE show, very well, the lack of Gd-4f character in the valence band. We can thus conclude that the treatment of the Gd 4f states as core states in calculations is justified. The weak resonances in the 8.2 eV scan of Fig. 4.25, result from the transitions  $4d^{10}4f^N \rightarrow 4d^94f^{N+1}$  and are characteristic of Gd. The strong overlap of the Gd-4d and Gd-4f orbitals results in an exchange interaction that

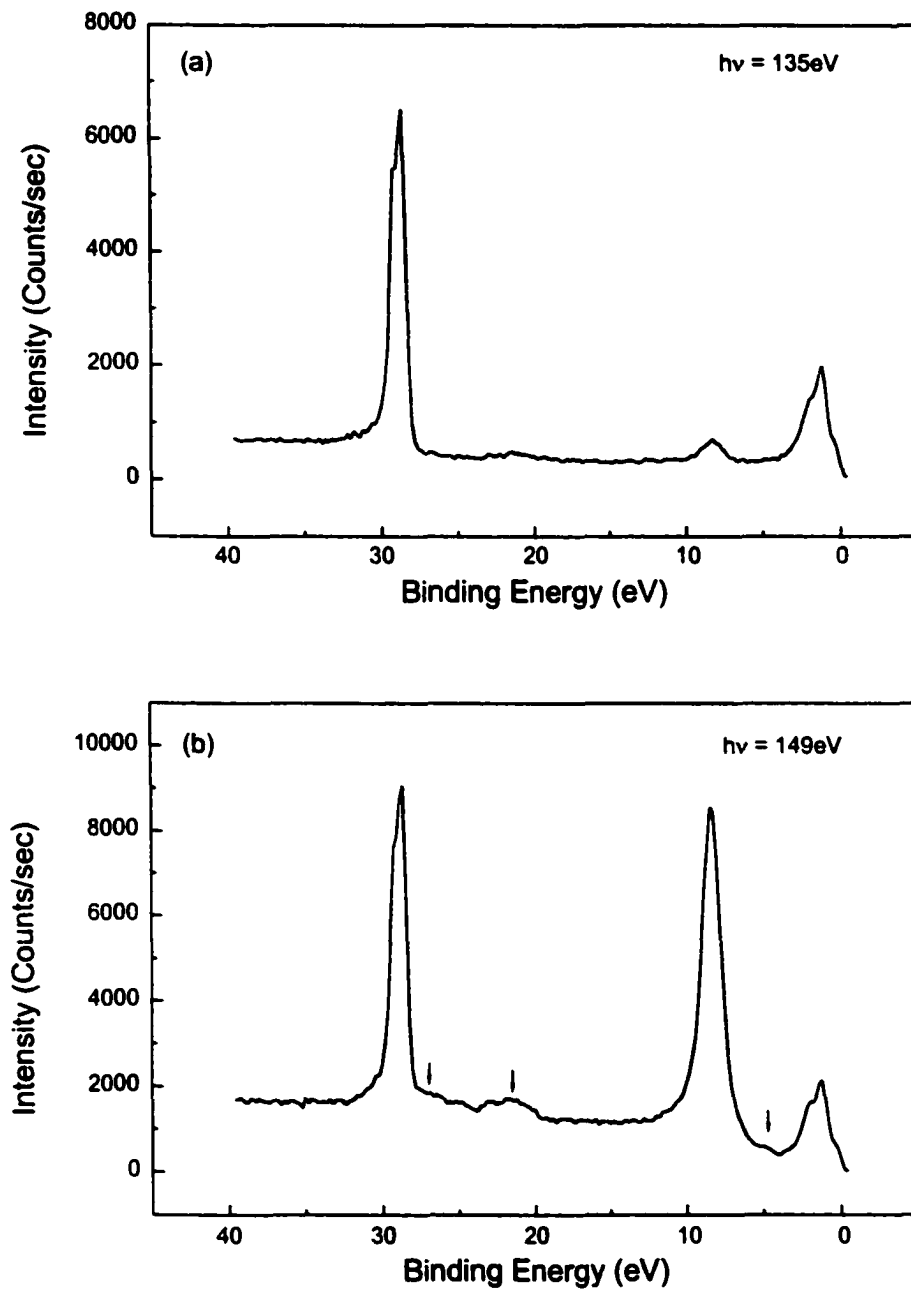
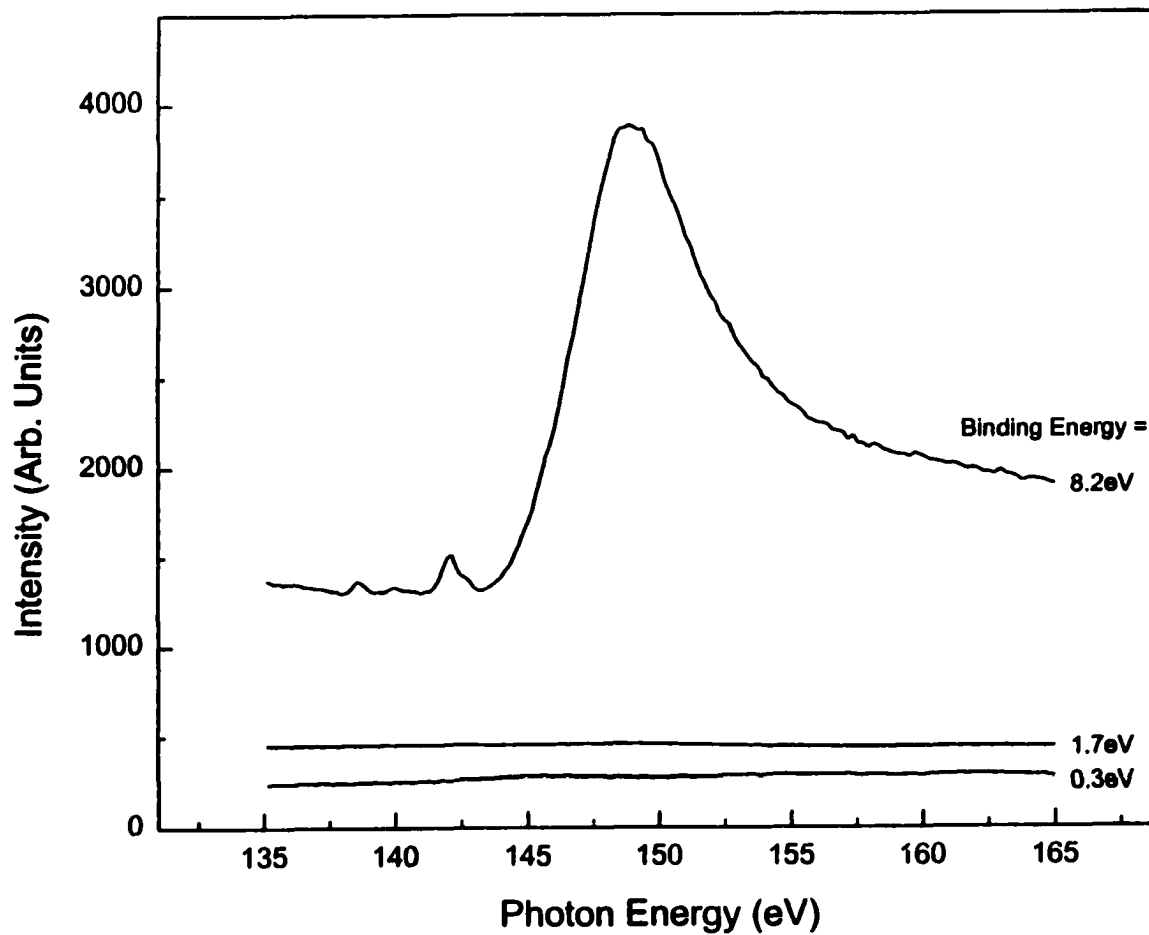


FIG. 4.24 EDCs taken off (a) and on (b) resonance for the Gd-4f peak. The core-absorption threshold for the Gd 4d-4f transition is  $\sim 142.6\text{eV}$ . The arrows in (b) indicate the enhancement of the Gd-5p and -6s orbitals as well.



**FIG. 4.25** CIS scans taken at the Gd-4f peak (BE = 8.2eV) and the valence band (BE = 1.7 and 0.3eV). The lack of signal in the valence band indicates lack of Gd-4f character. The fine structure in the 8.2 eV scan is characteristic of Gd.

splits the  $4d^9 4f^{N+1}$  configuration over a very broad range of energy. In doing so, some of the energy levels are forced below threshold [41].

The resonant effect shown in Fig. 4.24 is strong enough that we can see other enhancements as well (marked by arrows). The broad Gd-5p orbitals can be seen at BE = 21.6 and 27.2 eV. One can nearly make out the fine structure of the broad peaks. Also enhanced is the Gd-6s band at  $\sim 4.9$  eV. Calculations corroborate this observation as the bands near this energy were calculated to be of Gd-6s character (see Fig. 4.18) [37]. Lastly noted in Fig. 4.24 are the split Ge-3d core levels (also fit with Lorentzians). They are located at BE = 28.4 and 29.0 eV.

We now describe the attempt to find evidence of the SDW. We expect evidence to present itself in the form of a decrease of intensity at the Fermi edge when the crystal temperature passes below  $T_N = 27.1$  K and transitions from paramagnetic to antiferromagnetic. This would be the effect of the band splitting described in the appendix.

Our experimental procedure is as follows. A total of 27 high-resolution scans were taken of the Fermi-edge in both the paramagnetic (T held at 50 K) and anti-ferromagnetic (T held at 20 K) phases. Resolution at these temperatures was determined to be 53 meV and 48 meV at 50 K and 20 K respectively. These scans were taken around the expected location of the nested Fermi surfaces. These lie at  $q_z = 0.19$  and  $0.28$  in units of  $2\pi/a$ . At each of these  $q_z$  values, the area between  $q_x, q_y = 0.13$  and  $q_x, q_y = 0.17$  (units of  $2\pi/a$ ) is the area of nesting (see Fig. 4.26).

Analyzing the resulting scans, there was no observed change between the two

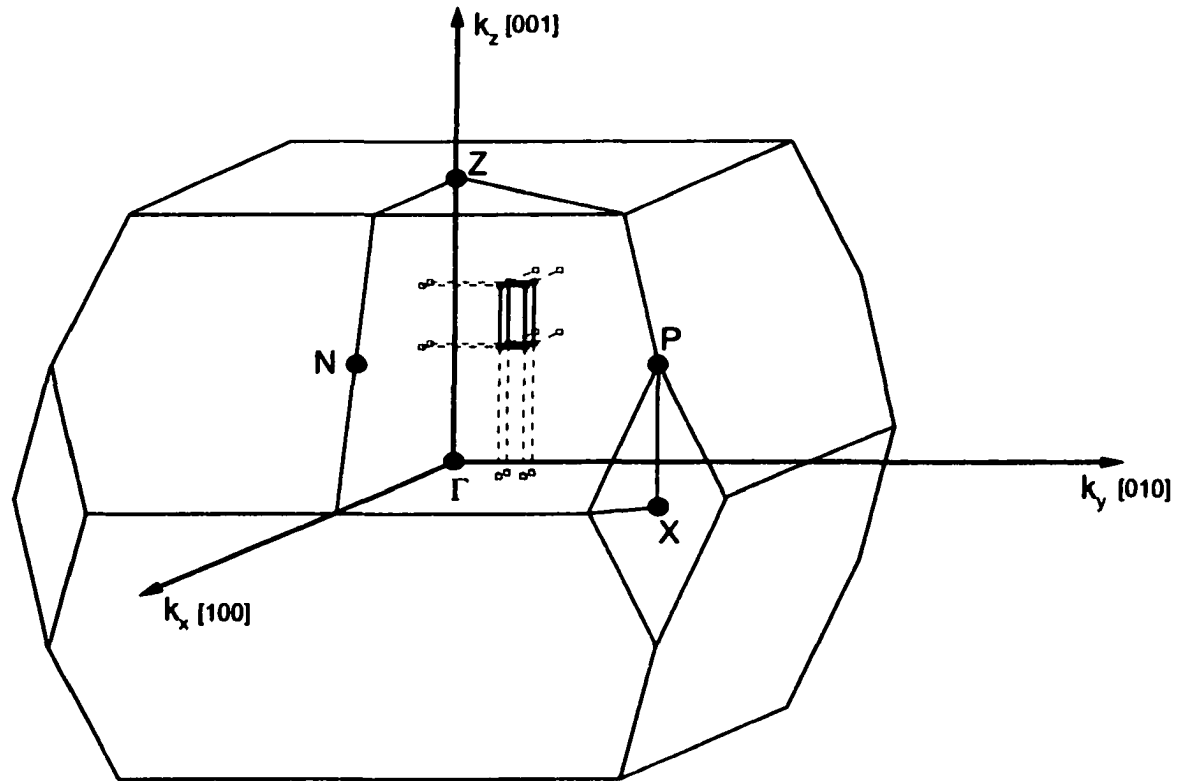


FIG. 4.26 Expected location of the fermi-surface nesting outlined by solid lines within the BCT Brillouin zone. Dotted lines extend back to the (001), (010), and (100) planes to give perspective. Note that this region is shown in only one quadrant, but, by symmetry, exists in all quadrants.

magnetic phases (except for the temperature-broadened Fermi edge). Thus, we were unable to find any experimental evidence of a SDW. One reason for this could be that the change is too subtle to pick up with our present resolution (angular resolution of  $2^\circ$ ). Note that broadening of the Fermi-edge due to temperature is most likely low enough to not have adverse effects. Future experiments on higher resolution beamlines may be enlightening. Other future experiments may involve a more thorough mapping of the band structure in both magnetic phases.

## CHAPTER 5: SUMMARY

We have performed ARPES and AIPES on crystalline samples of MnBi and GdNi<sub>2</sub>Ge<sub>2</sub>. The purpose was to investigate the valence band and the shallow core levels of both samples.

In MnBi, the valence band was found to be approximately 12 eV wide. The majority of the photoemission intensity was due to the Mn-3d states. Evidence of Bi-6p states within approximately 1 eV of the Fermi edge was also found. The peak at the Fermi edge is believed to be of Mn-3d character. The location of the most intense peak at BE  $\cong$  2.5 eV agreed very well with calculations, though a large number of counts with BE > 6.5 eV may be due to inelastic scattering from the roughly cleaved surfaces. Dispersion of two photoemission features was found along the normal (0001) direction. The symmetry seen in the dispersion lead to a determination of the inner potential  $V_0$  to be 14 eV. Bi-5d core levels showed no signs of satellites or inelastic tails, indicating lack of Bi character at the Fermi edge.

In GdNi<sub>2</sub>Ge<sub>2</sub>, dispersion of photoemission peaks in the valence band was found in the  $\Gamma$ XUZ and  $\Gamma$  $\Sigma$ NZ planes of the Brillouin zone. Feature locations and dispersion matched that of the calculation well. The valence band was determined to consist of mostly Ni-3d character. An inner potential of 13.5 eV was found by mapping the Fermi

surface in the normal direction. A large discrepancy between experiment and calculation was noted in what looked to be a half-BZ shift between the two. However, there is no shift seen when comparing the normal scans ( $\Gamma \rightarrow Z$  direction) to the calculated band structure. This discrepancy is still unresolved. The lack of dispersion along the normal indicated weak bonding in this direction, though intensity changes were still seen to coincide with the extended Brillouin zone.

Resonance of the Gd-4f states showed them to be localized at 8.25 eV BE. When crossing the Gd 4d $\rightarrow$ 4f core-absorption threshold, resonance of the Gd-5p and Gd-6s states was also seen. No evidence of a SDW was found, though this just indicates a need for better resolution.

## APPENDIX A: THE KERR EFFECT

A plane-polarized beam of light, when incident on a ferromagnetic body magnetized in a direction parallel to the light propagation, splits into transmitted and reflected beams. These beams become elliptically polarized with their major axes rotated with respect to the plane of polarization of the incident beam. This phenomenon, when it refers to the transmitted beam, is known as the Faraday effect; when it refers to the reflected beam, it is known as the polar Kerr effect (see Fig. A.1a). Other Kerr effects, known as transverse and longitudinal, refer to situations where the magnetization is not parallel to the beam. These, and the Faraday effect, are not discussed here.

One can picture how the Kerr effect works by viewing plane- (or linearly-) polarized light as the combination of left-handed and right-handed circularly polarized light (LCP and RCP) (see Fig. A.1b). When propagating along the z-axis, LCP and RCP are described by the electric-field vector

$$\mathbf{E}_{\pm} = \text{Re}\{E_0 \exp\{i(\omega t - 2\pi n_{\pm} z / \lambda_0)\}(\mathbf{e}_x \pm i\mathbf{e}_y)\} \quad (\text{A.1})$$

where (+) and (-) refer to right- and left- handed circular polarization,  $\lambda_0$  is the wavelength in vacuum,  $n_{\pm}$  is the complex index of refraction for the two states of polarization, and  $\mathbf{e}_x$  and  $\mathbf{e}_y$  are unit vectors in the x- and y-directions respectively. Here, the sign convention has the  $\mathbf{E}$  vector of RCP rotating in a clockwise sense at a given point

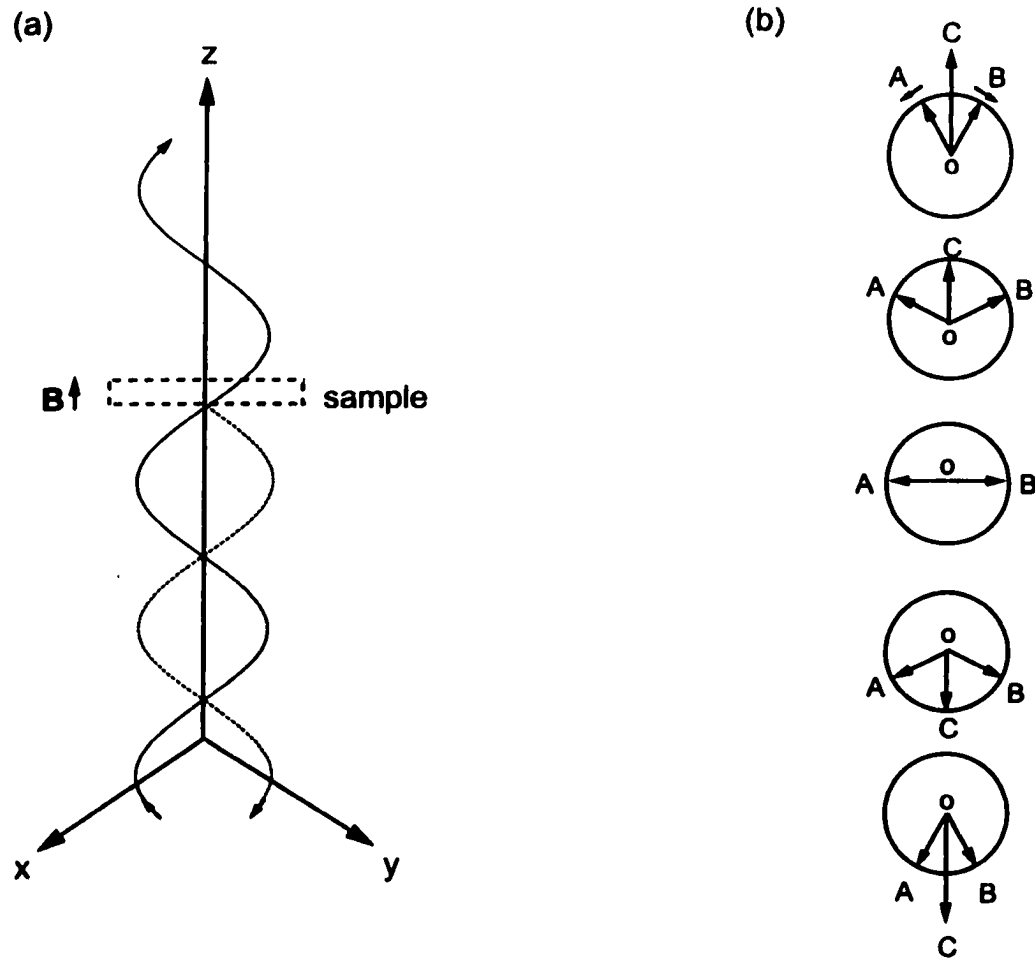


FIG. A.1 a) Scheme to illustrate the transmission and reflection of the Faraday and Kerr effects, respectively. The curved line represents the motion of the electric field vector for right-handed circularly polarized light (rcp) as it propagates along the z axis. b) Shows how a beam of linearly polarized (lp) light can be resolved into two beams of circular light. The E field of the (lp) light (C), is the addition of the rcp light (B) and the left-handed circularly polarized light (lcp) (A).

in space when viewed in the direction of propagation (see Fig. A.1). Upon reflection, and depending on the direction of the magnetization, one of these components (RCP or LCP) is absorbed more than the other. This dichroic effect then results in elliptical polarization with a rotation of the major axis.

With the magnetization in the [0001] direction (for a hexagonal crystal), the form of the optical conductivity tensor is (from [42])

$$\sigma = \begin{pmatrix} \sigma_{xx} & \sigma_{xy} & 0 \\ -\sigma_{xy} & \sigma_{xx} & 0 \\ 0 & 0 & \sigma_{zz} \end{pmatrix}. \quad (\text{A.2})$$

The difference in the absorption rate of LCP and RCP is proportional to the absorptive part of the off-diagonal optical conductivity tensor,  $\text{Im}(\sigma_{xy})$ . This is given for spin up electrons by (from [42])

$$\text{Im}(\sigma_{xy\uparrow}) = \frac{\pi e^2}{4\hbar\omega m^2 V} \sum_{\alpha\beta} \left\{ \left| \langle \beta \uparrow | \bar{\pi}^- | \uparrow \alpha \rangle \right|^2 - \left| \langle \beta \uparrow | \bar{\pi}^+ | \uparrow \alpha \rangle \right|^2 \right\} \delta(\omega_{\alpha\beta\uparrow} - \omega). \quad (\text{A.3})$$

Note that  $|\beta \uparrow\rangle$  and  $|\uparrow \alpha\rangle$  in the above expression are the spin-up crystal wave functions for the unoccupied and occupied states, respectively. They are normalized in the sample volume  $V$ . Also in the above expression,  $\bar{\pi}^\pm = \bar{\pi}_x \pm \bar{\pi}_y$  are linear combinations of the kinetic-momentum operator defined by

$$\bar{\pi} = \mathbf{p} + (\hbar / 4mc^2) \vec{\sigma} \times \vec{\nabla} V(r),$$

$\mathbf{p}$  being the momentum operator and the  $\vec{\sigma} \times \vec{\nabla} V(r)$  term represents a spin-orbit contribution.  $\delta(\omega_{\alpha\beta\uparrow} - \omega)$  is the condition for total energy conservation. The expression

for spin-down states is formally identical to (A.3) with spin-down states substituted for spin-up ones.

The Kerr rotation angle ( $\theta_K$ ) and ellipticity ( $\eta_K$ ) depend on the conductivity in the following way (note: here, a positive Kerr rotation is a clockwise rotation of the polarization ellipse as viewed when looking in the direction of propagation of the light):

$$\frac{1 + \tan(\eta_K)}{1 - \tan(\eta_K)} e^{2i\theta_K} = \frac{(1 + n_+)(1 - n_-)}{(1 - n_+)(1 + n_-)} \quad (\text{A.4})$$

where  $n_{\pm}$  are the complex indices of refraction for RCP(+) and LCP(-), given by:

$$n_{\pm}^2 = 1 + \frac{i4\pi}{\omega} (\sigma_{xx} \pm i\sigma_{xy}). \quad (\text{A.5})$$

For small Kerr angles, the above can be simplified [44] to

$$\theta_K + i\eta_K = \frac{-\sigma_{xy}}{\sigma_{xx} \sqrt{1 + (4\pi i / \omega) \sigma_{xx}}}. \quad (\text{A.6})$$

Note how the Kerr angle can be enhanced by a larger off-diagonal conductivity and a smaller diagonal part.

## APPENDIX B: SPIN DENSITY WAVES

Fermi surface nesting is the existence of nearly parallel planes of Fermi surface which can be strongly perturbed by a periodic lattice distortion. A periodic lattice distortion can come about in several ways. One such way is known as a charge density wave (CDW). A one dimensional example is shown in Fig. B.1. Suppose the periodic chain of atoms of periodicity  $a$  (Fig. B.1a), has the dispersion relation shown in the left frame of Fig. B.1b, with the Fermi surface crossing through it to form a metal. A simple view of Peierls' theorem is that to lower the system's energy, the lattice will distort, forming a new 'superlattice' with periodicity  $a'$  (shown in the lower portion of Fig. B.1a). The periodicity  $a'$ , will be of such a length as to form a band gap where the Fermi surface crossed the original band ( $\pi / a$ ), thus lowering the energy of the electrons.  $a'$  may or may not be commensurate with the underlying lattice constant  $a$  (in Fig. B.1,  $a'$  is equal to  $3a$ ). The charge density wave, results from electrons accumulating in the areas of extra bonding character around the larger atomic core density [45].

Spin density waves (SDW) can come about in a way similar to CDWs. In this case, the periodicity is changed by having an alternating excess of spin-up and spin-down electron density. If this alternation coincides with the atom positions (which does not have to be the case), a simple antiferromagnet is formed. A crude view of the SDW is

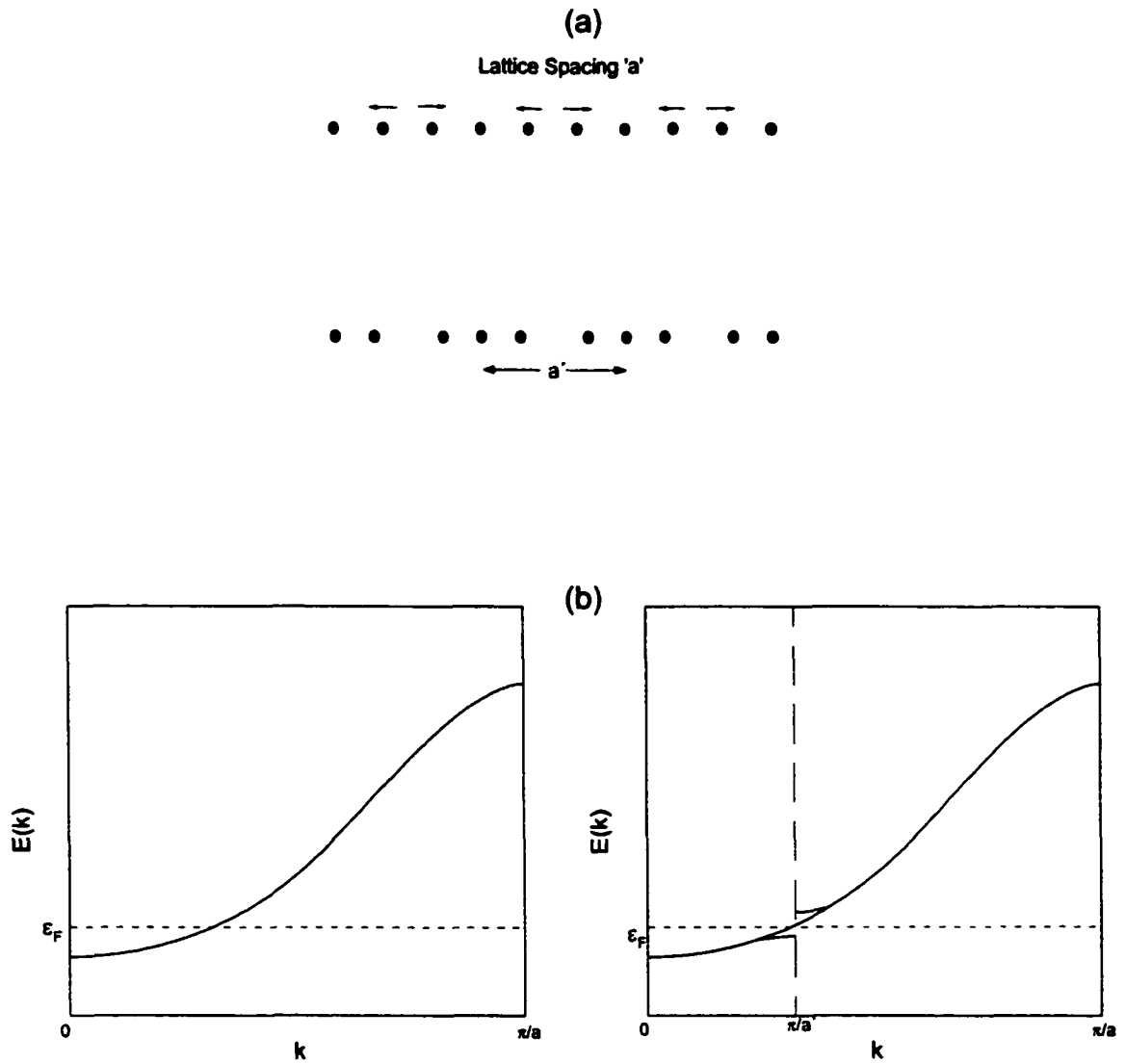


FIG. B.1 Example of a periodic distortion of a chain of atoms (a), along with its effect on the band structure (b). New band gaps will occur at  $k = \pi/a'$  where  $a'$  is the periodicity of the distortion (and also at multiples of this value of  $k$ , which are not shown here) [45].

having two CDWs, one for the 'spin-up' and one for the 'spin-down' sub-bands [46]. This is shown in Fig. B.2a. Here, the wavelength of the SDW is  $\pi/k_F$ , where  $k_F$  is the Fermi wavevector, and  $\rho$  indicates the spin-up and -down electron densities. Figure B.2b shows the energy gap opening up at  $\pm k_F$ , the location of the Fermi energy. The gap at the Fermi level will open up in both spin subbands.

Of course, the above works very nicely for a one-dimensional metal, whose Fermi surface is just 2 parallel planes - perfectly nested (see Fig. B.3a). Then, the new zone boundaries, created by a change in the periodicity of the lattice, affects the maximum number of states, making it energetically favorable for the transition to take place. However, for two- and three-dimensional Fermi surfaces, strong Fermi surface nesting is not so common. In the two-dimensional example in Figs. B.3b) and c), a Fermi surface with poor nesting and one with good nesting are shown. The dashed lines represent the new zone boundaries originating from the change in periodicity. One can see how, in the poorly nested Fermi surface, only a few states are affected by the change, so we would not expect a CDW here. In the Fermi surface with good nesting, however, many states are affected, and the result may end up being energetically favorable [45].

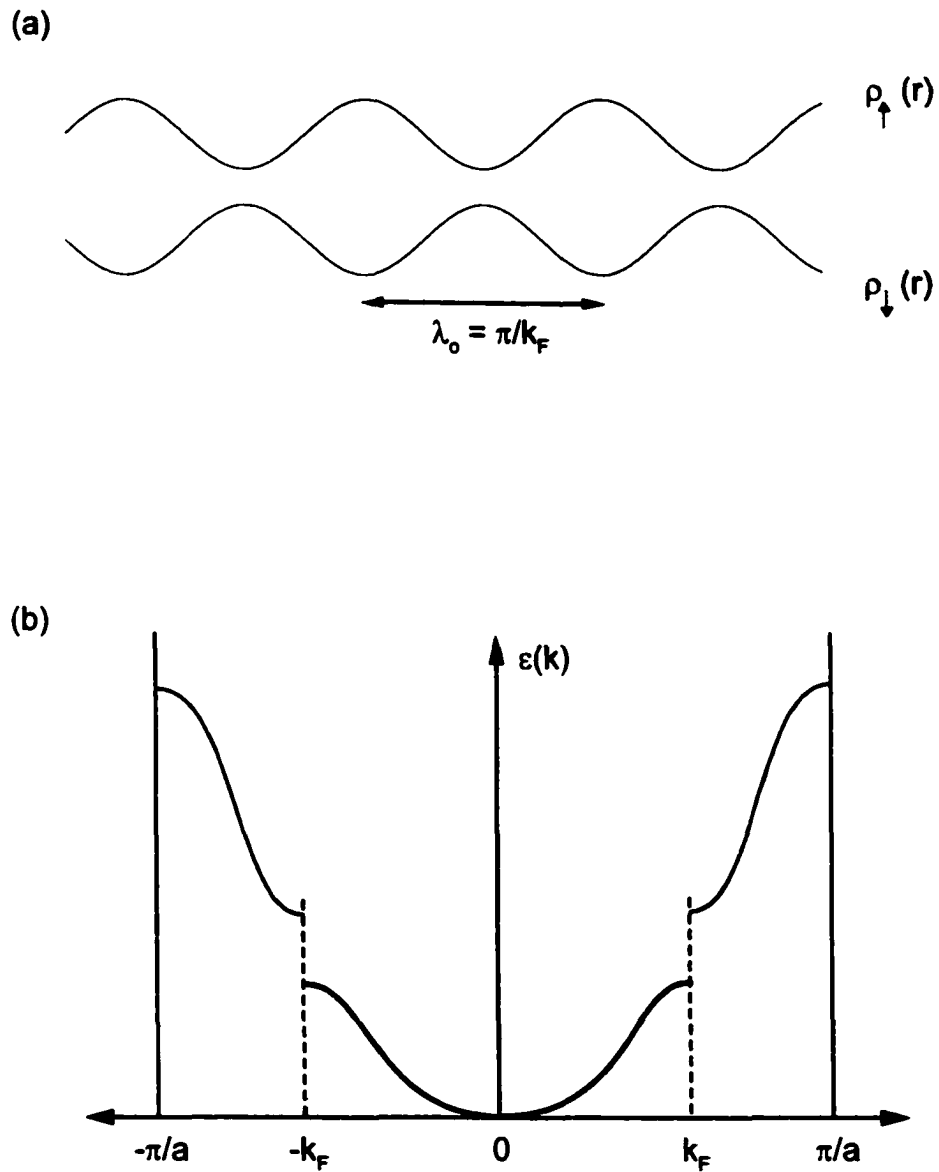
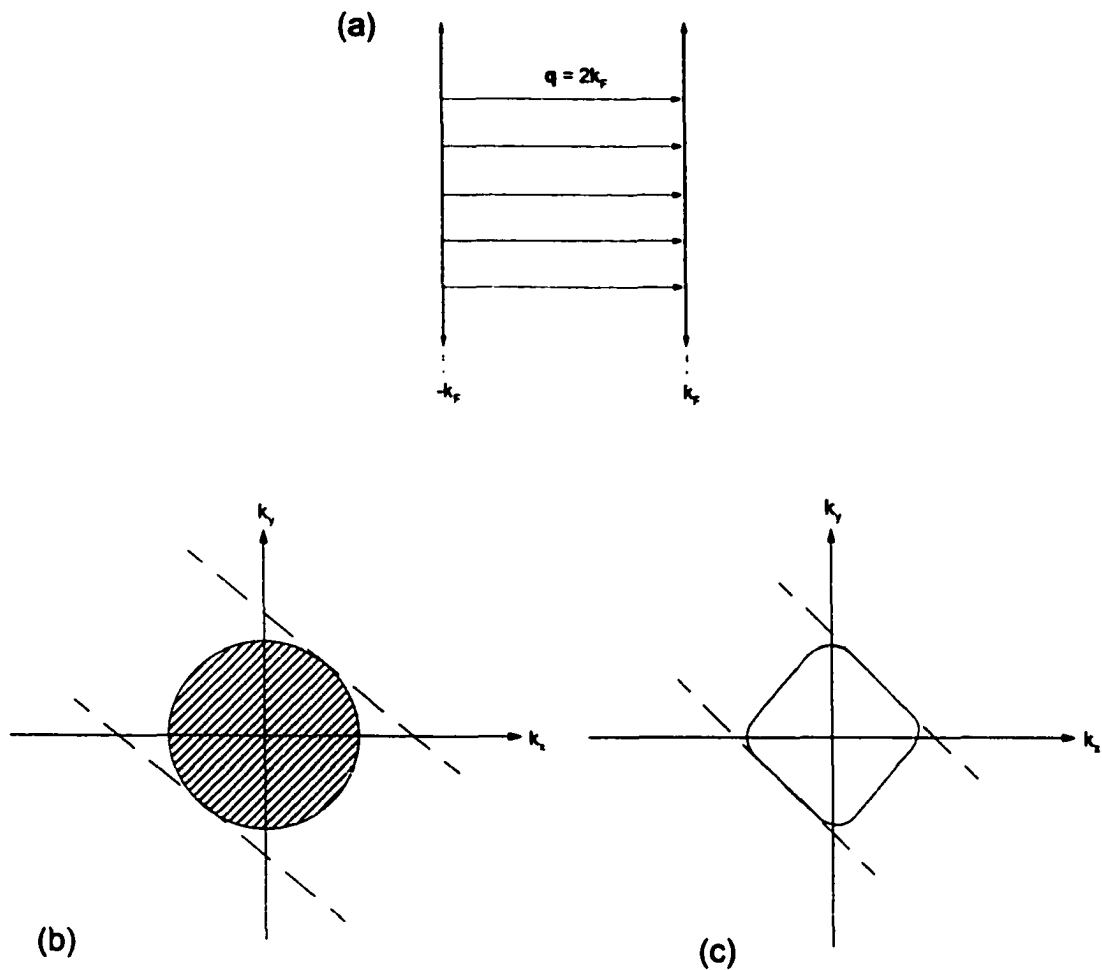


FIG. B.2 The dispersion relation and charge and spin density wave modulation for the two spin subbands in the spin density wave ground state [46].



**FIG. B.3** a) Fermi surface for a 1D free electron gas. The arrows indicate pairs of states that differ by the wavevector  $q = 2k_F$ , where  $k_F$  is the Fermi wavevector. b) & c) Fermi-surface nesting in two dimensions shown for two different topographies. The dashed lines represent new zone boundaries that might be introduced by a periodic lattice distortion. In (b), only a few states close to the Fermi surface are strongly perturbed, while in surface (c), which shows strong nesting, many states are perturbed, and the distortion may be energetically favorable [45].

**REFERENCES**

- [1] D. Chen, J. F. Ready, and E. Bernal G.: *J. Appl. Phys.* **39**, 3916 (1968).
- [2] K. -U. Harder, D. Menzel, T. Widmer, and J. Schoenes: *J. Appl. Phys.* **84**, 3625 (1998).
- [3] Prabhakar R. Bandaru, Timothy D. Sands, and Yukiko Kubota: *Appl. Phys. Lett.* **72**, 2337 (1998).
- [4] J. Köhler and J. Kübler: *J. Phys.: Condens. Matter* **8**, 8681 (1996).
- [5] P. Ravindran, A. Delin, P. James, and B. Johansson: *Phys. Rev. B* **59**, 15\_680 (1999).
- [6] R. F. Sabiryanov and S. S. Jaswal: *Phys. Rev. B* **53**, 313 (1996).
- [7] A. Szytula and J. Leciejewicz: *Handbook of Crystal Structures and Magnetic Properties of Rare Earth Intermetallics* (CRC Press, Boca Raton, 1994), pp. 114-192.
- [8] Z. Islam *et al.*: *Phys.Rev. B* **83**, 2817 (1999).
- [9] Stefan Hüfner: *Photoelectron Spectroscopy* (Springer, New York, 1996) page 1.
- [10] H. Hertz: Über einen Einfluss des ultravioletten Lichtes auf die elektrische Entladung (On the influence of ultraviolet light on the electric discharge). *Ann. Physik* **31**, 983 (1887).

- [11] A. Einstein: *Ann. Physik* **17**, 132 (1905).
- [12] Stefan Hüfner: *Photoelectron Spectroscopy* (Springer, New York, 1996)  
Chapt. 1.
- [13] Stefan Hüfner: *Photoelectron Spectroscopy* (Springer, New York, 1996)  
Chapt. 6.
- [14] M.P. Seah and W.A. Dench: *Surf. Interface Anal.* **1**, 2 (1979).
- [15] C.N. Berglund and W.E. Spicer: *Phys. Rev. A* **136**, 1030 and 1044 (1964).
- [16] David W. Lynch and Clifford G. Olson: *Photoemission Studies of High-Temperature Superconductors* (Cambridge University Press, New York, 1999)  
Chapt. 3.
- [17] Stefan Hüfner: *Photoelectron Spectroscopy* (Springer, New York, 1996)  
Chapt. 7.
- [18] S. Doniach and M. Sunjic: *J. Phys. C* **3**, 285 (1970).
- [19] Robert Z. Bachrach, ed.: *Synchrotron Radiation Research: Advances in Surface and Interface Science, Vol.1.: Techniques*: (Plenum Press, New York, 1992)  
Chapt. 6.
- [20] U. Fano: *Phys. Rev.* **124**, 1866 (1961).
- [21] E. M. Rowe: *Nucl. Instrum. Meth. B* **24/25**, 414 (1987).
- [22] J. D. Jackson: *Classical Electrodynamics* (John Wiley & Sons, New York, 1975)  
Chapt. 14.
- [23] Figure and additional information can be found at <http://www.src.wisc.edu/facilities/Aladdin/flux.html>

- [24] C. G. Olson: Nucl. Instrum. Methods Phys. Rev., Sect. A **266**, 205 (1988).
- [25] H. A. Rowland: Phil. Mag. **16**, 197 and 210 (1883).
- [26] F. C. Brown, R. F. Bachrach, and N. Lien: Nuc. Instrument Methods, **152**, 73 (1978).
- [27] M. Seya: Sci. Light **2**, 8 (1952).
- [28] VSW HA50 Hemispherical Analyzer Instruction Manual, VSW Scientific Instruments Ltd., Manchester, England (1989).
- [29] R. F. Davis *et al.*: Phys. Rev. B **31**, 1997 (1985).
- [30] T. B. Massalski, ed.: *Binary Alloy Phase Diagrams: 2nd Edition* (ASM International Publications, Materials Park, Ohio, 1990).
- [31] U. Fano: Phys. Rev. **124**, 1866 (1961).
- [32] J. J. Yeh and I. Lindau: *Atomic and Nuclear Data Tables*, Vol. 32, No.1, January 1985.
- [33] Stefan Hüfner: *Photoelectron Spectroscopy* (Springer, New York, 1996) page 18.
- [34] Akinori Tanaka, Masayuki Hatano, Kazutoshi Takahashi, Hiroyuki Sasaki, Shoji Suzuki, and Shigeru Sato: Phys. Rev. B **59**, 1786 (1999).
- [35] W. Rieger *et al.*: Monat. für Chemie **100**, 444 (1969).
- [36] P.C. Canfield and Z. Fisk: Philos. Mag. B **56**, 1117 (1992).
- [37] Z. Islam (private communication).
- [38] Stefan Hüfner: *Photoelectron Spectroscopy* (Springer, New York, 1996) page 88.
- [39] Stefan Hüfner: *Photoelectron Spectroscopy* (Springer, New York, 1996) page 91.
- [40] L.C. Davis and L.A. Feldkamp: Phys. Rev. B **23**, 6239 (1981).

- [41] Anthony F. Starace: *Phys. Rev. B* **5**, 1773 (1972).
- [42] Petros N. Argyres: *Phys. Rev.* **97**, 334 (1955).
- [43] J.L. Erskine and E.A. Stern: *Phys. Rev. B* **8**, 1239 (1973).
- [44] P. Ravindran, A. Delin, P. James, and B. Johansson: *Phys. Rev. B* **59**, 15\_680 (1999).
- [45] P.A. Cox: *Transition Metal Oxides* (Oxford University Press, Inc., New York, 1995) pp. 78-81.
- [46] George Grüner: *Density Waves in Solids* (Addison Wesley, New York, 1994), pp. 71-79.

## ACKNOWLEDGMENTS

I wish to thank my advisor, Professor David Lynch, for all his guidance and for his infinite patience. I also wish to thank Dr. Clifford Olson for all his help with the experimental and theoretical aspects of this work.

I thank Dr. P. Canfield for growing the  $\text{GdNi}_2\text{Ge}_2$  and MnBi crystals.

I would like to thank Dr. Z. Islam for helpful discussions on  $\text{GdNi}_2\text{Ge}_2$ .

I would like to thank Dr. I. Fisher for growing the MnBi crystals and for helpful discussions pertaining to them.

I would also like to thank my parents, Paul and Kathy, and my sister and brother, Kirsten and Nathan, for their unwavering support and love.

This work was performed at Ames laboratory under contract No. W-7405-eng-82 with the U.S. Department of Energy. The United States government has assigned the DOE Report number IS-T 2023 to this thesis.

This work is also based upon research conducted at the Synchrotron Radiation Center, University of Wisconsin-Madison, which is supported by the NSF under Award No. DMR-0084402.